論文 / 著書情報
Article / Book Information

題目(和文)	共振器内表面構造制御VCSELのモード制御と帯域幅向上に関する研究
Title(English)	Study on Mode Control and Bandwidth Enhancement of Intra-cavity Surface Engineered VCSELs
著者(和文)	GEChang
Author(English)	Chang Ge
出典(和文)	学位:博士(工学), 学位授与機関:東京工業大学, 報告番号:甲第12695号, 授与年月日:2024年3月26日, 学位の種別:課程博士, 審査員:植之原 裕行,小山 二三夫,中村 健太郎,西山 伸彦,宮本 智之,渡辺 正裕,粕川 秋彦
Citation(English)	Degree:Doctor (Engineering), Conferring organization: Tokyo Institute of Technology, Report number:甲第12695号, Conferred date:2024/3/26, Degree Type:Course doctor, Examiner:,,,,,,
学位種別(和文)	博士論文
Type(English)	Doctoral Thesis

博士論文

Study on Mode Control and Bandwidth Enhancement of Intra-cavity Surface Engineered VCSELs
(共振器内表面構造制御 VCSEL のモード制御と帯域幅向上に関する研究)

令和 5 年（2023 年）12 月版

提出者

東京工業大学 工学院 電気電子系 電気電子コース

Chang Ge

指導教員 小山二三夫特任教授
植之原裕行教授

内容

Chapter 1

Introduction

In this thesis, the intra-cavity surface engineered VCSEL with mode control and bandwidth enhancement is proposed and demonstrated. It also provides single-mode operation with hundred-micrometers long length. It may provide new opportunities for high-speed transmitters in the next-generation hyper-scale data centers and fronthaul-access 6G networks. In this chapter, the development of data center will be firstly discussed, and then the previous work of current high speed VCSEL.

1.1 Background

In recent years, the total network bandwidth in data centers has been steadily increasing over the years due to the growing demand for high-speed data transfer and the need to support data-intensive applications[1-6]. Especially from 2020, The global COVID-19 pandemic has had a significant impact on the data center industry, accelerating years of digital transformation into a matter of months. This has been driven by behavioral shifts in businesses and consumers, including a shift to remote and hybrid work, automation of business processes, and increased reliance on the digital economy. The pace and success of this digital transformation has garnered significant attention for the data center industry, as a broader audience began to understand the mission-critical nature and the value that data centers bring to their lives.

According to the Cisco annual Internet report from 2018 to 2023 white paper[7], quantitative projections are given on the growth of Internet users, devices and connections.

The total number of Internet users is rapidly growth from 3.9 billion in 2018 to 5.3 billion in 2023 with a 6% CAGR as shown in Fig. 1-1. By 2023, the devices and connections are growing faster than the Internet users with a 10% CAGR as shown in Fig. 1-2. Especially for the M2M connection which is machine-to-machine connection, it will be half of the total devices and connections with a 19% CAGR from 6.1 billion in 2018 to 14.7 billion by 2023 as shown in Fig. 1-3.

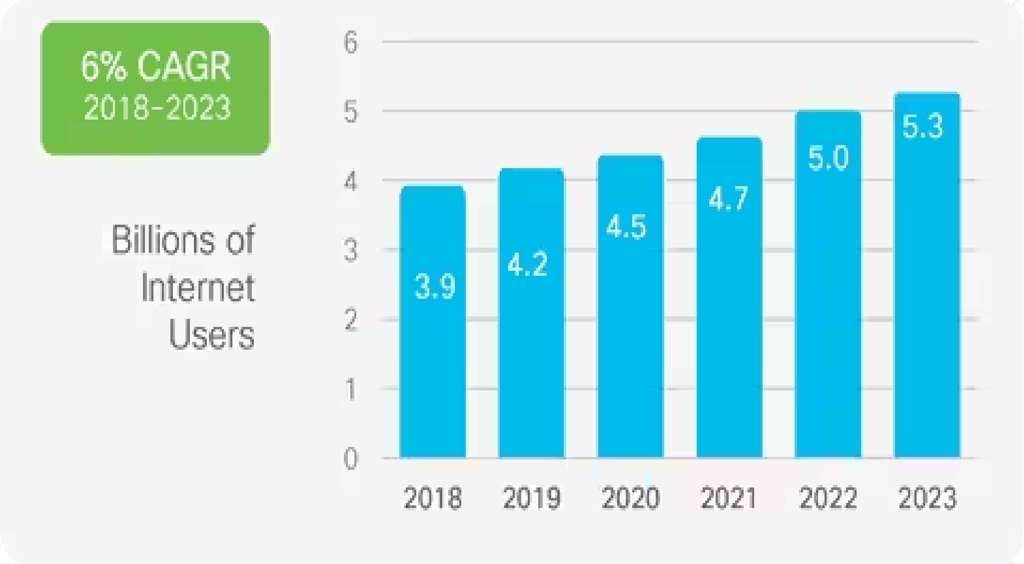

Fig. 1-1. Global Internet user growth[7]

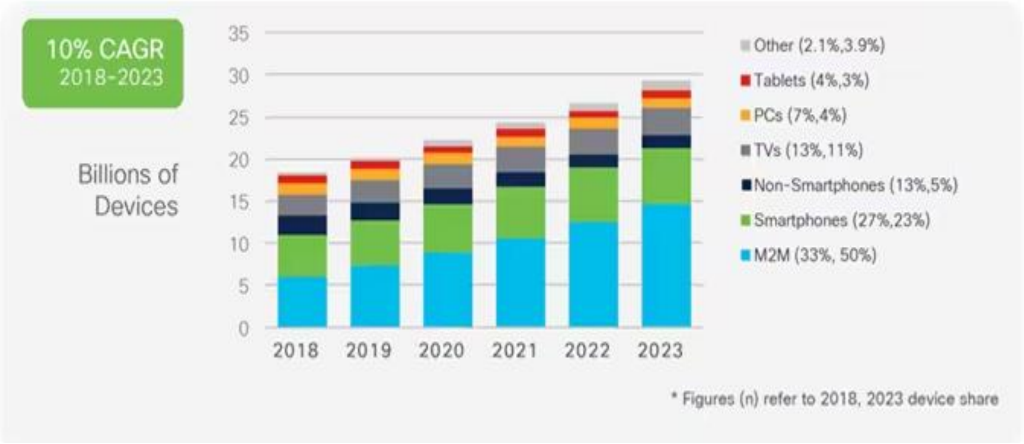

Fig. 1-2. Global device and connection growth[7]

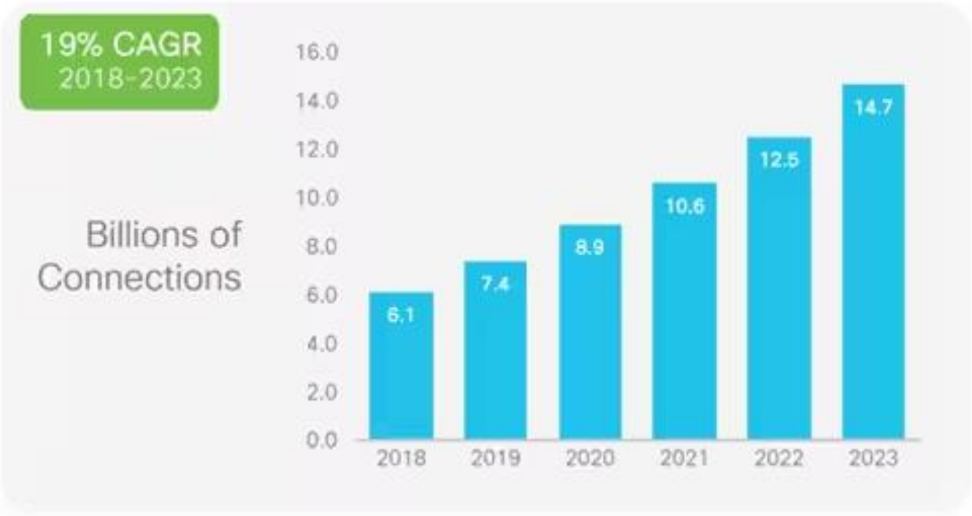

Fig. 1-3. Global M2M connection growth[7]

With the development of VR, cloud storage and gaming, UHD video, the significant bandwidth demands will be required as shown in Fig. 1-4. The bandwidth needs today is just a sliver of the future needs.

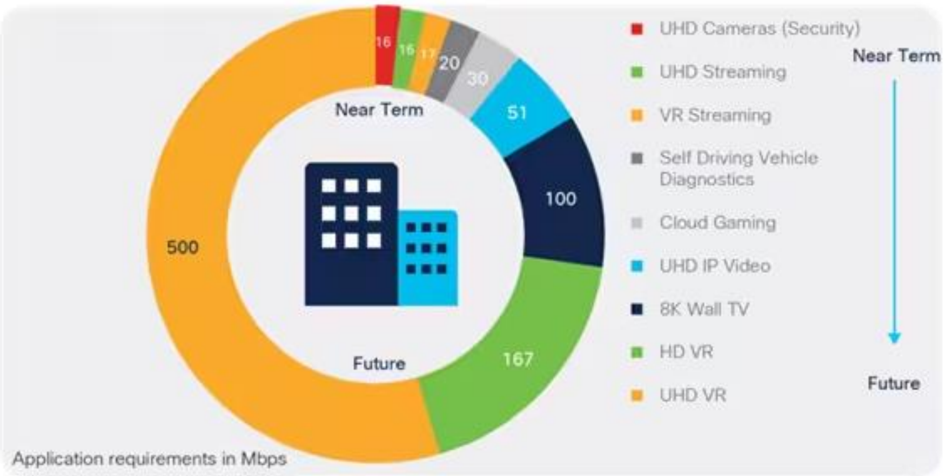

Fig. 1-4. Significant demand for bandwidth and video in the connected home of the future [7]

With the increasing number of data-intensive users and connections, managing data traffic has become a significant challenge in the development of the Internet. To address this issue, data centers have upgraded their network infrastructures to support multiterabit-per-second (Tbps) or even petabit-per-second (Pbps) bandwidth capabilities[8-10]. These upgrades involve the adoption of advanced technologies like high-speed optical networking[11-14], advanced Ethernet standards[15-16], and dense wavelength division multiplexing (DWDM)[17-20]. These technologies allow data centers to aggregate and transmit large volumes of data efficiently over high-capacity fiber optic networks. Furthermore, the trend towards hyperscale data centers, specifically designed to handle massive workloads and extensive data processing, has led to an increased demand for even higher network bandwidth.

According to the latest report from Dell'Oro Group[21], the 100G Ethernet market remains highly active, and shipments of 100G data center switches are expected to continue growing by more than 50 percent. While shipments of 100G port devices are currently experiencing significant momentum, analysts at Dell'Oro predict that shipments of 400G port equipment will also continue to increase in the coming years. As a result, hyperscale data centers have been deploying cutting-edge networking technologies such as 400 Gigabit Ethernet (GbE) and beyond to support their demanding requirements for high-performance computing and storage.

According to Dell'Oro's predictions[21], by 2024, ports of 400G and higher will make up more than 25% of total shipments, indicating significant growth in this segment. Additionally, the development of 800G ports is expected to gain momentum, resembling the emergence of a new technology era[21-22]. Sameh Boujelbene, Senior Director at Dell'Oro, emphasized the continued importance of optics in the data center switch market, highlighting that the availability of high-capacity and cost-effective optics is crucial for driving the adoption of higher speeds.

Moreover, the increasing presence of AI-driven workloads will continue to influence the development of data center networking infrastructure. As demand for faster processing and data transfer capabilities grows, the cost of high-speed port equipment is anticipated to gradually decline. This trend suggests that data center operators will be able to access more affordable and efficient networking solutions, enabling them to accommodate the evolving demands of AI and other data-intensive applications.

In order to fulfill the demand for accelerated expansion in data center bandwidth and cope with the substantial data traffic, there is a pressing necessity to augment both the bandwidth and transmission speed. As depicted in Figure 1-5, the data center encompasses multiple switches interconnected by means of optical links. According to Cisco's projections, the bandwidth of these switches is anticipated to surpass 100Tbps by 2026 as shown in Fig. 1-6[24]. However, it is noteworthy that the speed of fiber optic interconnects lags significantly behind that of the switches.

Overall, in the face of challenging data traffic and hyperscale data centers with transmission speeds of 400 Gigabit Ethernet or higher, as well as the substantial growth disparity between optical switches and fiber optics, there is a greater demand placed on the bandwidth and transmission speed of lasers, necessitating an urgent improvement in the laser's transmission speed to 100GBd within a kilometer.

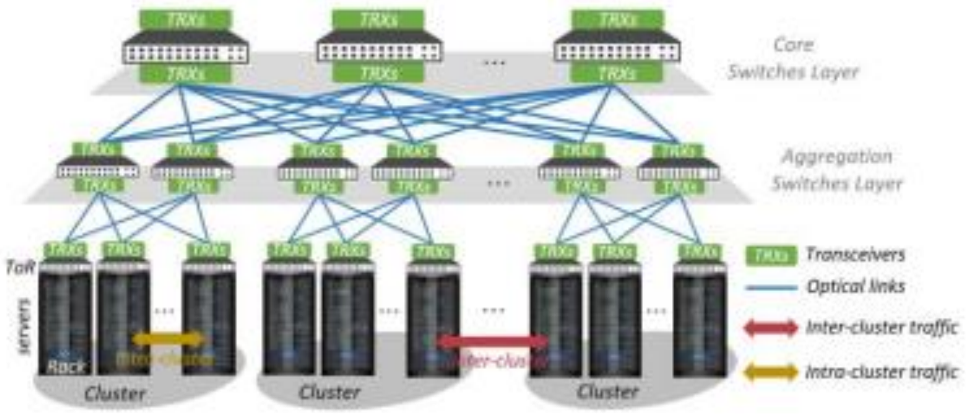

Fig. 1-5. Multi-tier tree-like data center network[23]

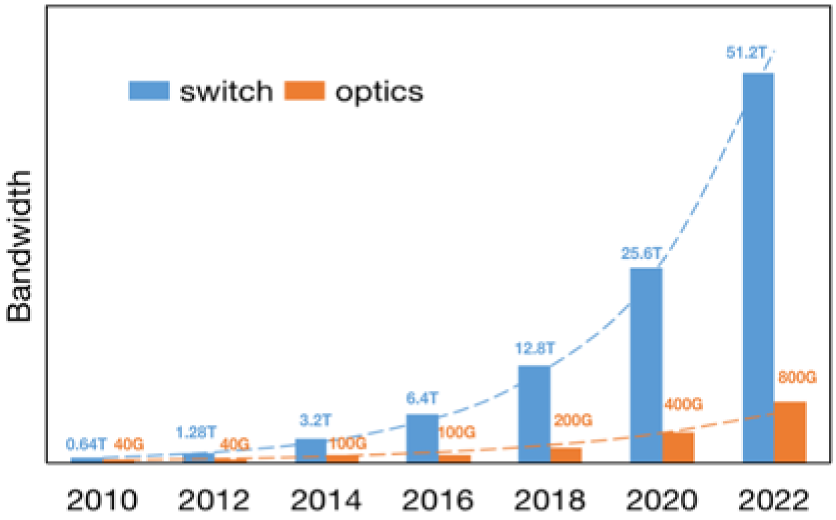

Fig. 1-6. Growth gap between optical switch and optics

1.2 Previous research about high-speed VCSELs

In general, there are two methods commonly employed for laser modulation. One approach involves direct modulation[24-27], which offers the advantages of low cost, low power consumption, and shorter transmission distances. The other method is electro-absorption modulation[28-29], which integrates the laser with an electro-absorption modulator, enabling long-distance transmission but at the expense of higher cost and increased power consumption.

Within the context of data centers, where transmission distances are typically less than 10km, the focus of this study will be on directly modulated lasers. Extensive investigations have been conducted on distributed feedback (DFB) lasers, distributed Bragg reflector (DBR) lasers, and vertical-cavity surface-emitting lasers (VCSELs). VCSELs, in particular, have garnered significant attention due to their surface-emitting characteristics, facilitating seamless coupling with optical fibers and the formation of two-dimensional arrays for achieving efficient 400GBd data transmission. Additionally, VCSELs offer advantages such as low threshold, low power consumption, cost-effective packaging, and the ability to undergo wafer-scale testing.

It is worth noting that the concept of VCSELs was first introduced by Professor Iga in 1977, involving the design of a laser cavity perpendicular to the wafer surface. Since then, VCSELs have gained widespread utilization, especially in optical interconnect applications within data centers [30-33].

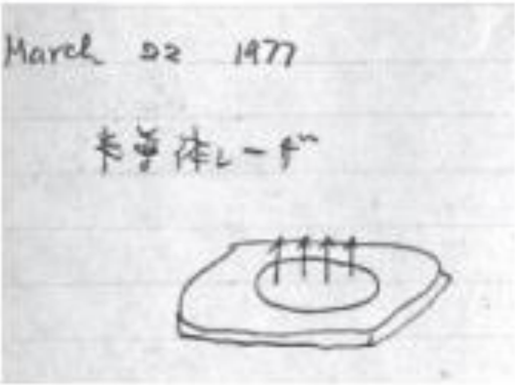

Fig. 1-7. A sketch of VCSEL idea from Prof. Iga in 1977[30]

Nevertheless, the modulation speed of directly modulated lasers is constrained by the relaxation oscillation frequency, which typically reaches around 20GHz for vertical-cavity surface-emitting lasers (VCSELs). Extensive research has been conducted to enhance the modulation bandwidth through the optimization of extrinsic series resistance, active region design, and other techniques [34-38].

In the case of VCSELs operating at the widely utilized 850nm wavelength for short-reach interconnects in the datacom and telecom markets, the modulation bandwidth has been increased to approximately 30GHz through multi-mode operation achieved by adjusting the active region, employing dielectric Bragg reflectors (DBRs), and optimizing parasitic effects [39-48]. In 2021, Yang et al[44]. introduced a high-speed 850nm VCSEL with two $Al_{0.98}Ga_{0.02}As$ oxidation layers for precise mode control and four $Al_{0.96}Ga_{0.04}As$ oxide layers for reducing mesa capacitance. This design approach enabled the realization of a modulation bandwidth of approximately 30GHz, approaching the intrinsic limitations of VCSEL responses, as illustrated in Figure 1-8. The notable enhancement in modulation bandwidth paves the way for 50-100Gbps (PAM4) modulation in next-generation optical interconnect systems. However, it is important to consider that the utilization of multi-mode operation introduces modal dispersion, which imposes a limitation on the maximum link length in multimode fiber (MMF) systems to below 100m.

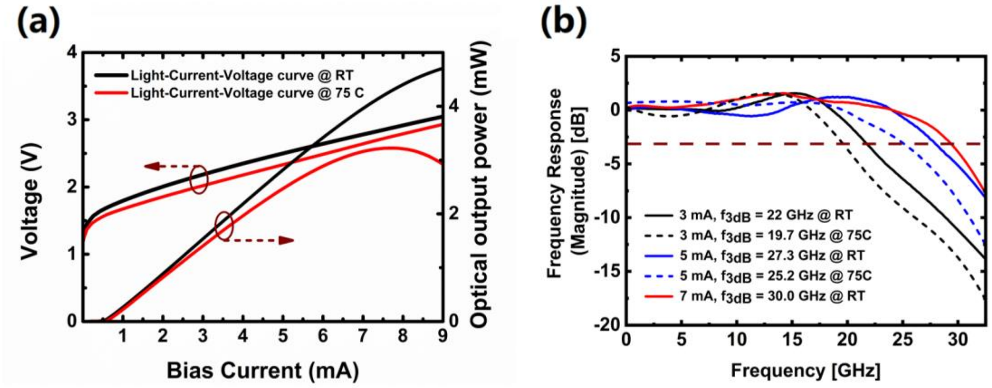

Fig. 1-8. (a) The L-I-V and (b) small signal bandwidth[44]

In 2022, Cheng et al[45]. presented a study on a single-mode vertical-cavity surface-emitting laser (VCSEL) operating at 850nm, which was passivated using atomic layer deposition (ALD). The research showcased a remarkable modulation bandwidth of 29GHz, as demonstrated in Figure 1-9. Specifically, a thin Al2O3 layer with a thickness of 10nm was deposited on the mesa sidewalls through the ALD process. This ALD-deposited film serves to mitigate non-radiative recombination losses, thereby enhancing the laser's overall efficiency. Furthermore, the introduction of this layer effectively reduces the RC parasitic component in the small-signal model, which often acts as a limiting factor in the modulation bandwidth of VCSELs. By implementing the mesa sidewall layer, the modulation bandwidth can be significantly increased, reaching approximately 29GHz while ensuring single-mode operation.

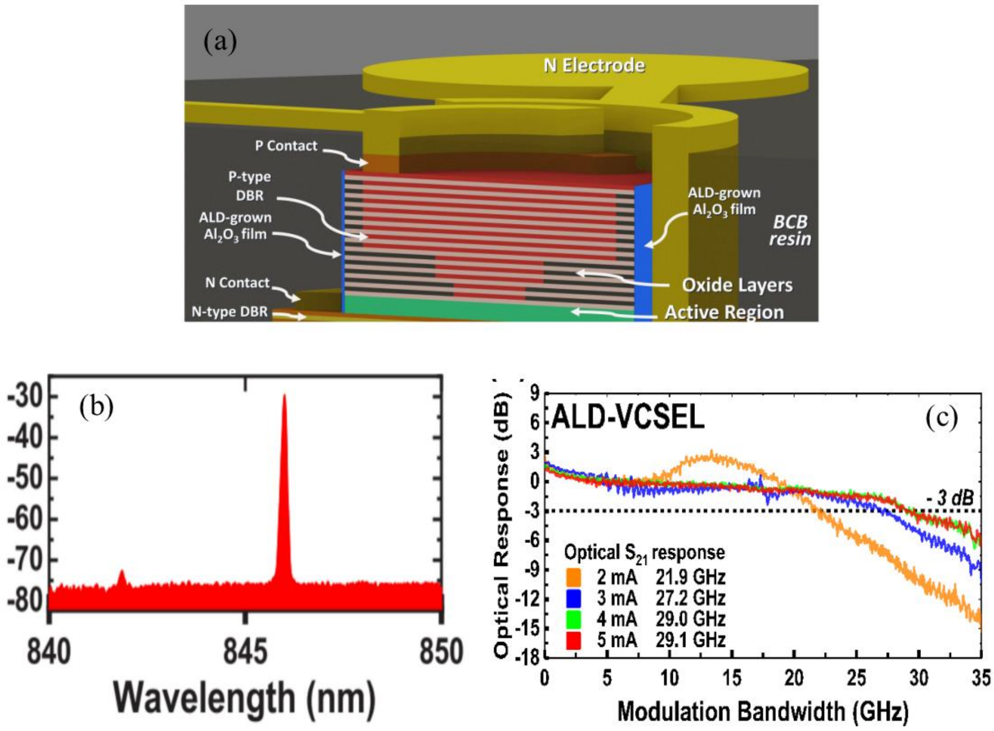

Fig. 1-9. (a) The schematic structure, (b) measured spectrum, and (c) small signal bandwidth[45]

However, the oxidation aperture diameter was merely 2.5 μ m, and the output power was approximately 1mW, posing a challenge for its usage in kilometer-long data transmission due to the significant attenuation losses experienced in the fiber. In order to facilitate long-range transmission within extensive data centers, the implementation of long-wavelength, single-mode operation vertical-cavity surface-emitting lasers (VCSELs) becomes imperative. An attractive option in this regard is the utilization of 1300-/1550-nm VCSELs with extended wavelengths.

In 2016, Kuchta et al.[46] conducted a 1500nm InP based VCSEL, featuring a buried tunnel junction, as depicted in Figure 1-10. The incorporation of the tunnel junction resulted in a reduced effective cavity length, thereby decreasing the photon lifetime. Consequently, the small signal modulation bandwidth could be further increased to

22GHz. However, it is important to acknowledge that the high thermal and electrical resistance associated with this configuration imposes limitations on the static performance of the VCSEL.

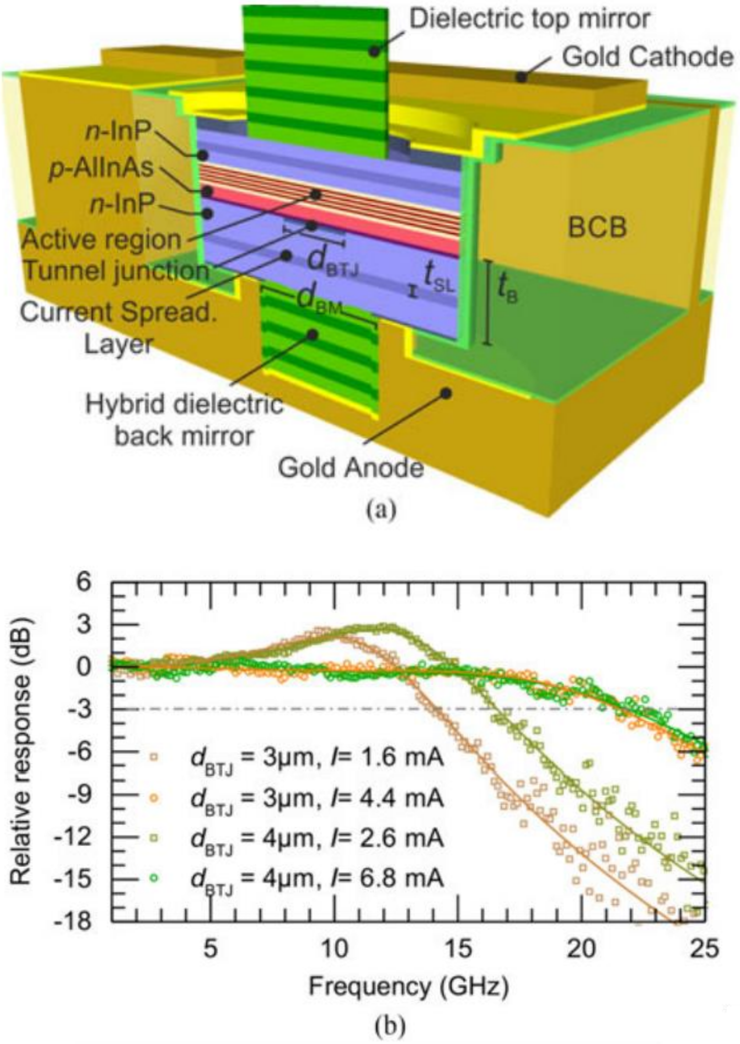

(a)

(b)

Fig. 1-10. (a) Schematic structure of InP based VCSEL with buried tunnel junction, (b) small signal modulation response of the VCSEL with 4μm tunnel junction[46]

To address the requirements of long-distance, high-speed data transmission, the utilization of 1060nm GaAs based VCSELs emerges as an appealing prospect. This wavelength choice is particularly advantageous due to the reduced fiber attenuation observed at 1060nm band compared to the 850nm band. In fact, the attenuation levels at

1060nm can be less than half of those experienced in the 850nm band, thus establishing the potential for kilometer-long data transmission[47-48].

In 2018, Larsson et al.[49] introduced a 1060nm vertical-cavity surface-emitting laser (VCSEL) that operates in a single-mode configuration and incorporates two primary oxide apertures, as illustrated in Figure 1-11. These primary oxide apertures serve the purpose of both transverse optical confinement and current confinement, while an additional four secondary apertures are implemented to reduce the capacitance associated with charge storage over the oxide layers. This innovative design enabled the attainment of a small signal modulation bandwidth of 22.5GHz, allowing for 40Gbps (NRZ) data transmission over a single-mode fiber (SMF) spanning a distance of 2km, as demonstrated in Figure 1-12. However, it should be noted that achieving single-mode operation necessitated the use of a relatively small oxidation aperture of only 4 μ m. Therefore, it is of utmost importance to prioritize the development of a 1060nm single-mode VCSEL that ensures stable single-mode operation, high modulation bandwidth, and a larger oxidation aperture.

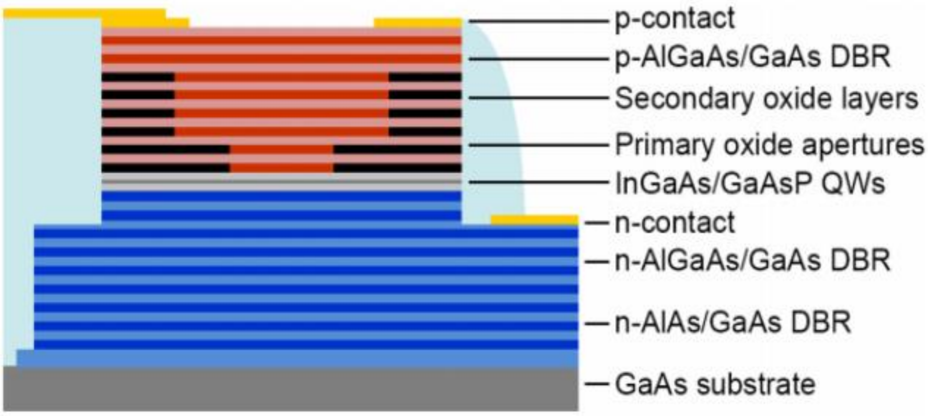

Fig. 1-11. Schematic structure of the 1060nm SM-VCSEL[49]

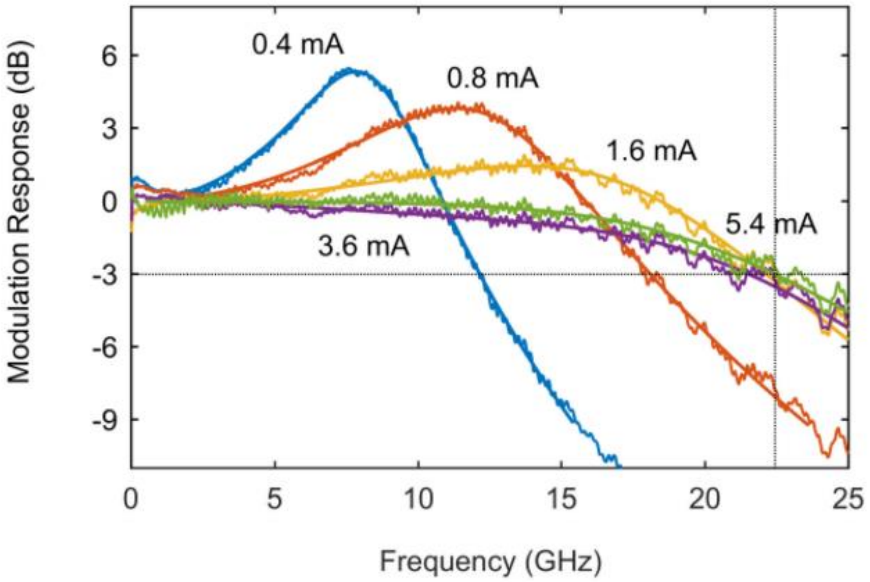

Fig. 1-12. Small signal modulation bandwidth[49]

To expand the modulation bandwidth and overcome the limitations imposed by the relaxation oscillation frequency of VCSELs, the phenomenon of photon-photon resonance holds promise. Photon-photon resonance has found extensive application in distributed feedback (DFB) lasers and distributed Bragg reflector (DBR) lasers. In 2014, Ibrahim et al.[50] introduced a bow-tie-shaped transverse coupled cavity (TCC) VCSEL, as depicted in Figure 1-13, which showcased a substantial enhancement in the modulation bandwidth, reaching up to 27GHz, as demonstrated in Figure 1-14. The bow-tie-shaped oxide aperture incorporated in the design served as a passive feedback cavity, enabling the occurrence of photon-photon resonance between the original optical frequency, devoid of feedback, and the modulated frequency subsequent to feedback. This photon-photon resonance (PPR) effect facilitated the customization of the modulation transfer function, thereby extending the frequency response to levels surpassing the relaxation oscillation frequency. However, it is important to note that the augmentation in bandwidth was exceptionally sensitive to the injection current within the laterally integrated feedback cavity. Furthermore, the injection current contributed to additional power consumption. Additionally, the presence of multiple modes in operation resulted in a broad spectral width, which significantly compromised the transmission bandwidth, even when employing high-bandwidth multi-mode fibers.

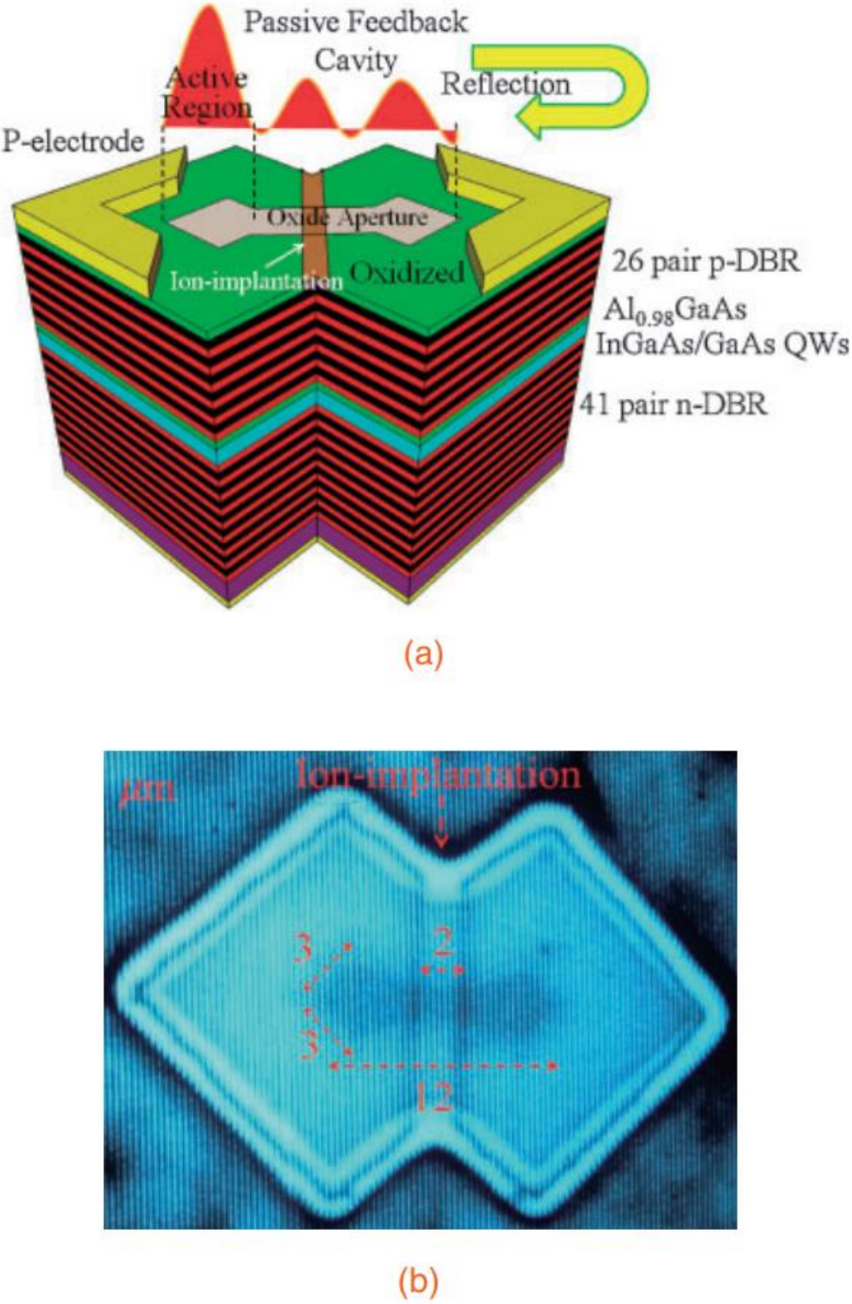

Fig. 1-13. (a) Schematic structure and (b) top view of the TCC VCSEL[49]

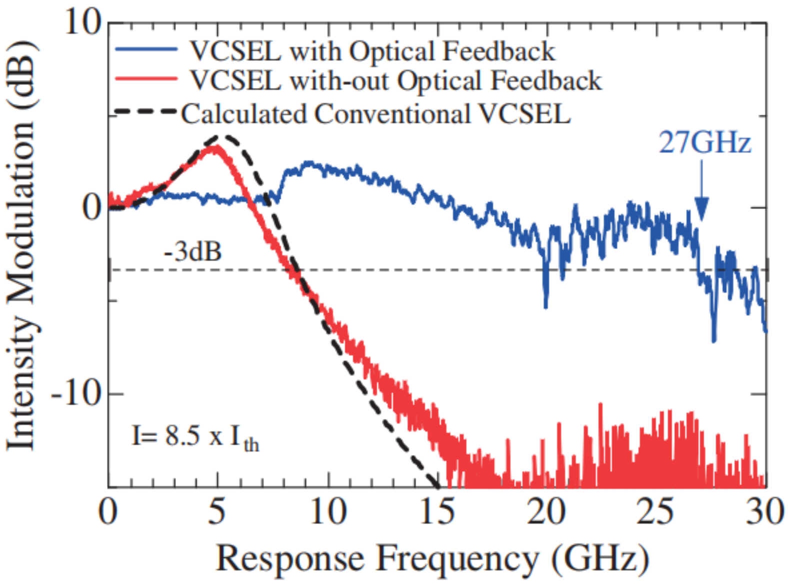

Fig. 1-14. Measured small-signal modulation response of the TCC VCSEL with and without optical feedback[50]

Recently, our research team presented a 1060nm VCSEL with a metal aperture that demonstrated an improved bandwidth of 22GHz and enhanced control over transverse modes by leveraging the transverse coupled cavity effect [51-54], as depicted in Figure 1-15[53]. The incorporation of an intra-cavity metal aperture facilitated the establishment of transverse coupled cavities, where the oxidation boundary and the metal boundary interacted to induce transverse resonance, as illustrated in Figure 1-15(b). Notably, the transmission exhibited a clear eye opening up to 46Gbps across a 5km single-mode fiber.

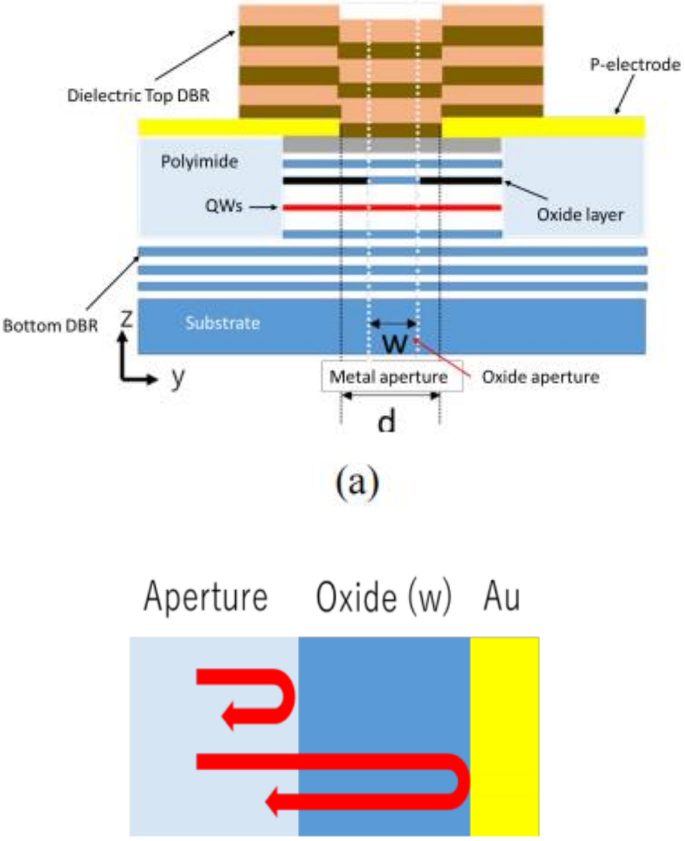

(a)

(b)

Fig. 1-15. (a) Schematic structure and (b) the physical picture of the transverse resonance[53]

While achieving stable single-mode operation is feasible, it remains a challenge to further augment the modulation bandwidth. A critical aspect in accomplishing this is the mitigation of extrinsic parasitic effects. Nonetheless, despite the attainment of stable single-mode operation, the potential for bandwidth enhancement remains constrained.

1.3 Research purpose

Given the escalating data traffic, substantial growth disparity in relation to optical switches, and the demand for 400GbE data transmission, the need for high-speed lasers has become more pronounced. VCSELs, known for the surface-emitting properties facilitating effortless fiber coupling, have emerged as pivotal light sources in data centers, particularly for short-reach applications. The objective of this thesis is to advance the development of a high-speed VCSEL beam by focusing on the following areas:

- Designing and fabricating intra-cavity metal-aperture VCSEL;
- Improving the modulation bandwidth of intra-cavity metal-aperture VCSEL by introducing polyimide layer to reduce parasitics;
- Realizing the km-long data transmission by intra-cavity metal-aperture VCSEL;
- Simulating the surface grating loaded VCSEL for mode control and bandwidth enhancement;
- Designing and fabricating surface grating loaded VCSEL with single mode operation and high-speed data transmission.

1.4 Organization of the thesis

- **Chapter 1**: The application of high-speed lasers and previous work about VCSEL were introduced.
- **Chapter 2**: The principle and theoretical analysis of bandwidth enhancement and mode control method by surface engineered process will be demonstrated..
- **Chapter 3**: The fabrication process and electrical and optical characteristics of intra-cavity metal-aperture VCSEL will be proposed and demonstrated. The parasitic optimization will also be demonstrated.
- **Chapter 4**: The experimental result of intra-cavity metal-aperture VCSEL for data transmission will be proposed and demonstrated.
- **Chapter 5**: The principle and simulation results of surface grating VCSEL will be demonstrated.

- **Chapter 5**: The fabrication and simulation results of surface grating VCSEL will be demonstrated.
- **Chapter 6**: The prospective and potential of intra-cavity surface engineered VCSEL will be discussed and the thesis will be concluded.

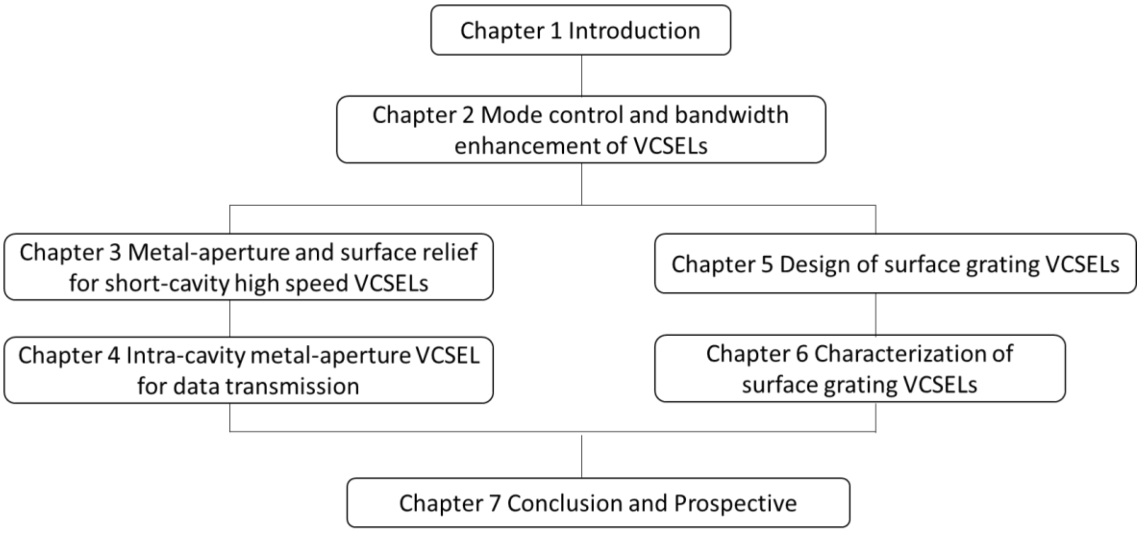

Fig 1-36 Organization frame of the thesis

Reference in Chapter 1

1) Kant, Krishna. "Data center evolution: A tutorial on state of the art, issues, and challenges." Computer Networks 53.17 (2009): 2939-2965.

2) Benson, Theophilus, et al. "Understanding data center traffic characteristics." ACM SIGCOMM Computer Communication Review 40.1 (2010): 92-99.

3) Liu, Yanan, et al. "Energy consumption and emission mitigation prediction based on data center traffic and PUE for global data centers." Global Energy Interconnection 3.3 (2020): 272-282.

4) Meng, Xiaoqiao, Vasileios Pappas, and Li Zhang. "Improving the scalability of data center networks with traffic-aware virtual machine placement." 2010 Proceedings

IEEE INFOCOM. IEEE, 2010.

5) Kachris, Christoforos, and Ioannis Tomkos. "A survey on optical interconnects for data centers." IEEE Communications Surveys & Tutorials 14.4 (2012): 1021-1036.
6) Sato, Ken-ichi. "Realization and application of large-scale fast optical circuit switch for data center networking." Journal of Lightwave Technology 36.7 (2018): 1411-1419.
7) Cisco Annual Internet Report (2018-2023) White Paper. https://www.cisco.com/c/en/us/solutions/collateral/executive-perspectives/annual-internet-report/white-paper-c11-741490.html.
8) Groumas, Panos, et al. "Multi-100 GbE and 400 GbE interfaces for intra-data center networks based on arrayed transceivers with serial 100 Gb/s operation." Journal of Lightwave Technology 33.4 (2014): 943-954.
9) Zhou, Yu Rong, and Kevin Smith. "Practical innovations enabling scalable optical transmission networks: real-world trials and experiences of advanced technologies in field deployed optical networks." Journal of Lightwave Technology 38.12 (2020): 3106-3113.
10) Carusone, Tony Chan, et al. "F6: Optical and Electrical Transceivers for 400GbE and beyond." 2021 IEEE International Solid-State Circuits Conference (ISSCC). Vol. 64. IEEE, 2021.
11) Shieh, William. "OFDM for flexible high-speed optical networks." Journal of lightwave technology 29.10 (2011): 1560-1577.
12) Routray, Sudhir K., et al. "The new frontiers of 800g high speed optical communications." 2020 4th International Conference on Electronics, Communication and Aerospace Technology (ICECA). IEEE, 2020.

13) Vetter, Ronald J., and David Hung-Chang Du. "Distributed computing with high-speed optical networks." Computer 26.2 (1993): 8-18.

14) Amiri, I. S., Ahmed Nabih Zaki Rashed, and P. Yupapin. "High-speed light sources in high-speed optical passive local area communication networks." Journal of Optical Communications 44.1 (2023): 61-67.

15) Sofia, Rute C. "A survey of advanced ethernet forwarding approaches." IEEE Communications surveys & tutorials 11.1 (2009): 92-115.

16) Hank, Peter, et al. "Automotive ethernet: in-vehicle networking and smart mobility." 2013 Design, Automation & Test in Europe Conference & Exhibition (DATE). IEEE, 2013.

17) Elmirghani, Jaafar MH, and Hussein T. Mouftah. "All-optical wavelength conversion: technologies and applications in DWDM networks." IEEE Communications Magazine 38.3 (2000): 86-92.

18) Gumaste, Ashwin, and Tony Antony. DWDM network designs and engineering solutions. Cisco press, 2003.

19) Kahn, Joseph M., and Keang-Po Ho. "Spectral efficiency limits and modulation/detection techniques for DWDM systems." IEEE Journal of selected topics in quantum electronics 10.2 (2004): 259-272.

20) Yu, Jianjun, and Xiang Zhou. "Ultra-high-capacity DWDM transmission system for 100G and beyond." IEEE Communications Magazine 48.3 (2010): S56-S64.

21) 100GbE Trends in Data Center Network Development. https://community.f s.com/ blog/100gbe-trends-in-data-center-network-development.html.

22) Achieving sustainable data center growth. https://www.delloro.com/ knowledge-center/white-papers/achieving-sustainable-data-center-growth/

23) Xue, Xuwei, et al. "Optical Switching Data Center Networks: Understanding Techniques and Challenges." arXiv preprint arXiv:2302.05298 (2023).

24) Yamamoto, Tsuyoshi. "High-speed directly modulated lasers." Optical Fiber Communication Conference. Optica Publishing Group, 2012.

25) Matsuo, Shinji, and Takaaki Kakitsuka. "Low-operating-energy directly modulated lasers for short-distance optical interconnects." Advances in Optics and Photonics 10.3 (2018): 567-643.

26) Zhu, Ning Hua, et al. "Directly modulated semiconductor lasers." IEEE Journal of Selected Topics in Quantum Electronics 24.1 (2017): 1-19.

27) Sudo, Tsurugi, et al. "Challenges and opportunities of directly modulated lasers in future data center and 5G networks." Optical Fiber Communication Conference. Optica Publishing Group, 2021.

28) Schrenk, Bernhard. "Electroabsorption-modulated laser as optical transmitter and receiver: status and opportunities." IET Optoelectronics 14.6 (2020): 374-385.

29) Mason, Beck, et al. "Widely tunable sampled grating DBR laser with integrated electroabsorption modulator." IEEE Photonics Technology Letters 11.6 (1999): 638-640.

30) Iga, Kenichi. "Forty years of vertical-cavity surface-emitting laser: Invention and innovation." Japanese Journal of Applied Physics 57.8S2 (2018): 08PA01.

31) Koyama, Fumio. "Recent advances of VCSEL photonics." Journal of Lightwave Technology 24.12 (2006): 4502-4513.

32) Söderberg, Emma, et al. "High-temperature dynamics, high-speed modulation, and transmission experiments using 1.3-µm InGaAs single-mode VCSELs." Journal of lightwave technology 25.9 (2007): 2791-2798.

33) Marc. A. Taubenblatt, "Optical Interconnects for high-performance computing." 2012 IEEE Photonics Conf. IPC 2012 30 [4], 183.

34) Iga, Kenichi. "Vertical-cavity surface-emitting laser: Its conception and evolution." Japanese Journal of Applied Physics 47.1R (2008): 1.

35) MacDougal, Michael H., et al. "Low resistance intracavity-contacted oxide-aperture VCSELs." IEEE Photonics Technology Letters 10.1 (1998): 9-11.

36) Ding, Y., et al. "Low threshold current density, low resistance oxide-confined VCSEL fabricated by a dielectric-free approach." Applied Physics B 98 (2010): 773-778.

37) Li, Hui, et al. "Corrections to “Impact of the Quantum Well Gain-to-Cavity Etalon Wavelength Offset on the High Temperature Performance of High Bit Rate 980-nm VCSELs”[Aug 14 613-621]." IEEE Journal of Quantum Electronics 50.9 (2014): 782-782.

38) Westbergh, Petter, et al. "Impact of photon lifetime on high-speed VCSEL performance." IEEE Journal of Selected Topics in Quantum Electronics 17.6 (2011): 1603-1613.

39) Haglund, Erik, et al. "High-speed VCSELs with strong confinement of optical fields and carriers." Journal of Lightwave Technology 34.2 (2016): 269-277.

40) Haglund, Erik, et al. "30 GHz bandwidth 850 nm VCSEL with sub-100 fJ/bit energy dissipation at 25–50 Gbit/s." Electronics Letters 51.14 (2015): 1096-1098.

41) Liu, Anjin, et al. "Vertical-cavity surface-emitting lasers for data communication and sensing." Photonics Research 7.2 (2019): 121-136.

42) Chorchos, Lukasz, et al. "Energy efficient 850 nm VCSEL based optical transmitter and receiver link capable of 80 Gbit/s NRZ multi-mode fiber data transmission."

Journal of Lightwave Technology 38.7 (2020): 1747-1752.

43) Cheng, Hao-Tien, et al. "Recent advances in 850 nm VCSELs for high-speed interconnects." Photonics. Vol. 9. No. 2. MDPI, 2022.

44) Yang, Yun-Cheng, Hao-Tien Cheng, and Chao-Hsin Wu. "30 GHz Highly Damped Oxide Confined Vertical-Cavity Surface-Emitting Laser." 2021 IEEE Photonics Conference (IPC). IEEE, 2021.

45) Cheng, Hao-Tien, et al. "29 GHz single-mode vertical-cavity surface-emitting lasers passivated by atomic layer deposition." Optics Express 30.26 (2022): 47553-47566.

46) Spiga, Silvia, et al. "Single-mode high-speed 1.5-μm VCSELs." Journal of Lightwave Technology 35.4 (2016): 727-733.

47) Lavrencik, Justin, et al. "Error-free 100Gbps PAM-4 transmission over 100m OM5 MMF using 1060nm VCSELs." Optical Fiber Communication Conference. Optica Publishing Group, 2019.

48) Simpanen, Ewa, et al. "1060 nm single-mode VCSEL and single-mode fiber links for long-reach optical interconnects." Journal of Lightwave Technology 37.13 (2019): 2963-2969.

49) Larsson, A., et al. "1060 nm VCSELs for long-reach optical interconnects." Optical Fiber Technology 44 (2018): 36-42.

50) Dalir, Hamed, and Fumio Koyama. "High-speed operation of bow-tie-shaped oxide aperture VCSELs with photon–photon resonance." Applied Physics Express 7.2 (2014): 022102.

51) Ibrahim, Hameeda R., et al. "1060nm single-mode metal aperture VCSEL array with transverse resonance for 5km single-mode fiber transmission." 2021 Optical

Fiber Communications Conference and Exhibition (OFC). IEEE, 2021.

52) M. Ahmed, "Modeling of generating ultra-high frequency oscillations in VCSEL integrated with cascaded transverse coupled cavities." Appl. Phys. B Lasers Opt. 126 [11], 1 2020.

53) Ibrahim, Hameeda R., et al. "1060nm Single-mode Metal-aperture VCSEL Array with Transverse Resonance and Low Power Consumption below 50 fJ/bit." 2021 European Conference on Optical Communication (ECOC). IEEE, 2021.

54) Hu, Shanting, et al. "1060-nm single-mode transverse coupled cavity VCSEL with intra-cavity surface relief for 58-Gbps modulation and 5-km single-mode fiber transmission." Applied Physics Letters 120.26 (2022): 261110.

Chapter 2

Mode control and bandwidth enhancement of VCSELs

In this chapter, the details about operation principle, optimized design of mode control and bandwidth enhancement will be discussed. The previous work of surface engineered will also be shown.

2.1 Dynamic characteristics and mode control of VCSEL

2.1.1 Rate equation and modulating response of VCSEL

The utilization of VCSELs in data transmission is contingent upon their dynamic behavior and modulation characteristics. These attributes are typically derived from rate equations, which encapsulate the temporal evolution of electrons and photons within the laser cavity and their reciprocal interactions. The analysis of rate equations serves as a highly valuable means of scrutinizing the static, spectral, and dynamic properties of lasers. For a single-mode laser stimulated by direct current, the rate equations elegantly express the time derivatives of electrons and photons as follows[1-5]:

$$\frac{dN}{dt}=\frac{\eta_i}{e}I(t)-\frac{N}{\tau_s}-\Gamma GS+f_N(t) \tag{2-3}$$

$$\frac{dS}{dt}=\left[\Gamma G-\frac{1}{\tau_p}\right]S+\Gamma R_{sp}+f_S(t) \tag{2-4}$$

$$\frac{d\theta}{dt}=\frac{1}{2}\left(\alpha\Gamma\frac{a}{V}\left(N-N_{th}\right)\right)+f_\theta(t) \tag{2-5}$$

Where N is the electron density, S is the photon density, η_i is the injection efficiency, Γ is the confinement factor, τ_s and τ_p are the carrier lifetime and photon lifetime, respectively. R_{sp} is the spontaneous emission factor, N_{th} is the electron number at threshold. G is the optical gain as:

$$G = \frac{a}{V}\left(N - N_T\right)\left(1 - \varepsilon S\right) \tag{2-6}$$

where a is the tangential gain of the active region with the volume of V, N_T is the electron numbers at transparency, and ε is the gain suppression coefficient. The $f_N(t)$ $f_S(t)$, and $f_\theta(t)$ are Langevin forces which are responsible for laser noise.

$$f_s(t) = \sqrt{\frac{2R_{sp}\Gamma S(t)}{\Delta t}}.x_s \tag{2-7}$$

$$f_N(t) = \sqrt{\frac{2N(t)}{\tau_s \Delta t}}.x_n - \sqrt{\frac{2R_{sp}S(t)}{\Delta t}}.x_s \tag{2-8}$$

$$f_\theta = \sqrt{\frac{R_{sp}\Gamma}{2S(t)\Delta t}}.x_\theta \tag{2-9}$$

From the rate equation, with the fluctuation of the current, there is a fluctuation of the photon density which as a function of the modulation frequency ν. The modulation transfer function relates the photon density fluctuations to the modulating current is obtained as:

$$\mathrm{H}(\nu) = \frac{\Delta \mathrm{N}(\nu)}{\Delta \mathrm{I}(\nu)/\mathrm{q}} = \frac{\mathrm{A}}{4\pi^2(\nu_r^2 - \nu^2) + \mathrm{i}2\pi\gamma\nu} \tag{2-10}$$

where A is the amplitude factor as:

$$\mathrm{A} = \frac{\eta_l v_{gr}\Gamma_r \bar{a} N_0}{V_p(1 + \varepsilon N_0)} \tag{2-11}$$

where ν_r is the resonance frequency as:

$$\nu_r = \frac{1}{2\pi}\sqrt{\mathrm{A}\frac{V_p}{\tau_p}\left(1 + \frac{\varepsilon}{\tau_{sp} v_{gr}\Gamma_r \bar{a}}\right)} \tag{2-12}$$

where γ is the damping coefficient as:

$$\gamma = \mathrm{K}\nu_r^2 + \frac{1}{\tau_{sp}} \tag{2-13}$$

$$\mathrm{K} = 4\pi^2\left(\tau_p + \frac{\varepsilon}{v_{gr}\Gamma_r \bar{a}}\right) \tag{2-14}$$

The maximum 3-dB modulation frequency can be calculated as[3]:

$$\nu_{max} = \sqrt{2}\frac{2\pi}{K} \tag{2-14}$$

which indicates the limitation of the intrinsic modulation of around 20GHz[6]. Minimizing the K factor provides guidance for determining photon lifetime, group velocity, optical confinement, gain suppression coefficient, and differential gain coefficient in high-speed designs. It appears that a smaller gain compression and photon lifetime, along with larger optical confinement and group velocity, result in a reduced K factor and increased bandwidth. Additionally, the overall 3-dB modulation bandwidth encompasses the extrinsic modulation, represented by the parasitic modulation transfer function $H_p(\nu)$, given by[3]:

$$H_p(\nu) = \frac{i_a(\omega)}{v_s} \propto \frac{1}{\frac{(i\omega)^2}{\omega_0^2}+\frac{\omega}{\omega_0 \cdot Q}+1} \tag{3-1}$$

where i_a is the current in the intrinsic diode, and v_s is the drive voltage. In total, the measured small-signal modulation response of the VCSEL is approximately by the fit function $H_t(\nu)$ as[4]:

$$H_t(\nu) = \frac{B{\nu_r}^4}{({\nu_r}^2-\nu^2)^2+(\gamma\nu/(2\pi))^2} \cdot \frac{1}{1+(\nu/\nu_p)^2} \tag{3-1}$$

where ν_p is the characteristics parameter expressed as:

$$\nu_p = 1/(2\pi RC) \tag{3-1}$$

The series resistance and parasitic capacitance will cause a serious frequency limit which should be considered.

In the investigation of lasers, a large-signal model is employed through the numerical integration of rate equations. This comprehensive analysis encompasses the evaluation of modulation performance, which is contingent upon factors such as signal power and the quality of the eye diagram. To construct the eye diagram, the modulated laser waveform is divided into segments of varying bit lengths and subsequently superimposed. Within the domain of data communications systems, the non-return to zero (NRZ) modulation format has gained substantial popularity due to its inherent ease of generation. Consequently, its adoption has become widespread. The rate equations governing the behavior of VCSELs under large signal conditions are derived from the rate equations with modulating currents exhibiting levels of "1" or "-1".

2.1.2 Mode control and optical confinement of VCSEL

For long-distance data transmission utilizing single-mode fiber, achieving a single-mode condition is of utmost importance. An effective approach to obtain enhanced beam characteristics and increased single-mode power is by employing the oxide confinement process. This technique has been successfully implemented in GaAs-based VCSELs, where partial oxidation of a high Al-content layer within one of the AlGaAs-based DBRs, situated close to the active region, establishes an aperture for efficient current and optical confinement, as depicted in Figure 2.1[3]. The adoption of a small-aperture, oxide-confined VCSEL[7-8] results in improved beam quality and stability. This is attributed to the intrinsic index guide, which mitigates the impact of thermal lensing and carrier-related effects on the transverse mode. However, the small oxide aperture also lead to higher series resistance and low output power.

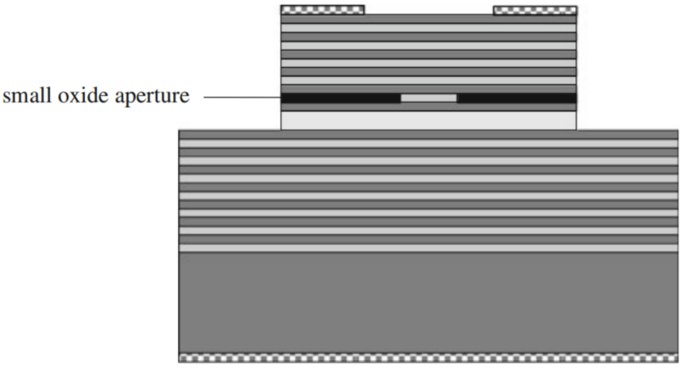

Fig.2-1. Schemes of oxide-confined VCSEL [3]

Some other solutions like buried heterostructure[9-10], photonic crystal structure[11-12], metal aperture[13-14], and surface relief[15-16] are investigated for mode selective and optical confinement.

By utilizing a photonic crystal structure, depicted in Figure 2-2[3], it is possible to establish a single-mode condition by carefully adjusting parameters such as depth, diameter, and refractive index.

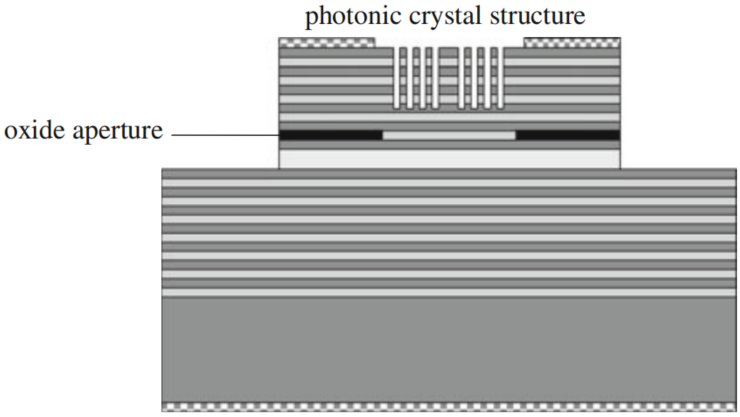

Fig.2-2. Schemes of photon crystal VCSEL [3]

Furthermore, the implementation of a metal-aperture structure combined with oxide confinement has yielded successful outcomes in attaining single-mode emission. This configuration effectively suppresses higher-order modes through a phase-mismatched reflection at the metal/semiconductor interface. As a result, cavity losses are increased within the metalized region, where the field intensity of higher-order modes exceeds that of the fundamental mode. Surface relief etching applied to the top DBR layer emerges as another efficacious method for achieving single-mode VCSELs. The introduction of shallow surface modifications has a substantial impact on the modal characteristics of VCSELs equipped with low-reflectivity top-DBR structures.

2.2 Modulation bandwidth enhancement method of photon-photon resonance effect

2.2.1 Principle and previous research of photon photon resonance effect

The intrinsic modulation speed of Directly Modulated Lasers (DMLs) faces limitations imposed by factors such as the RC time constant, damping effects, and the relaxation oscillation frequency[17-20], as exemplified in Chapter 2.1. The relaxation oscillation frequency, typically within the range of several GHz, represents an intrinsic limitation determined by the carrier-photon resonance. While modifying the laser's structure, such as employing multiple quantum wells, may enhance this frequency, there are still inherent constraints.

To surpass this limitation, one viable approach is to leverage the photon-photon resonance (PPR) effect[21-25], which can be achieved by incorporating an optical feedback cavity. Fig. 2-3 depicts the mechanism of the PPR effect, involving an active region accompanied by a passive external optical feedback cavity. The lasing light is coupled into the cavity, reflected by the oxidation aperture, and forms feedback. Photon photon resonance occurs between the original optical frequency without feedback and the modulated frequency after feedback. Through the utilization of the PPR effect, the 3-dB cut-off frequency can be significantly expanded, as illustrated in Fig. 2-4.

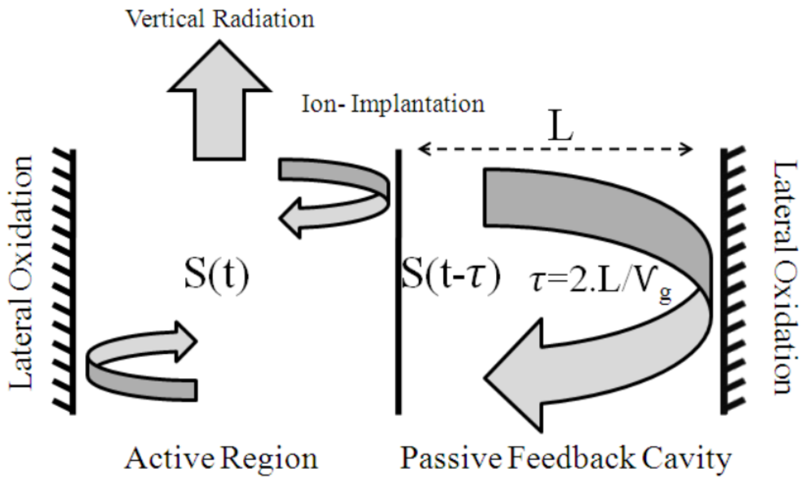

Fig.2-3. Mechanism of PPR effect [5]

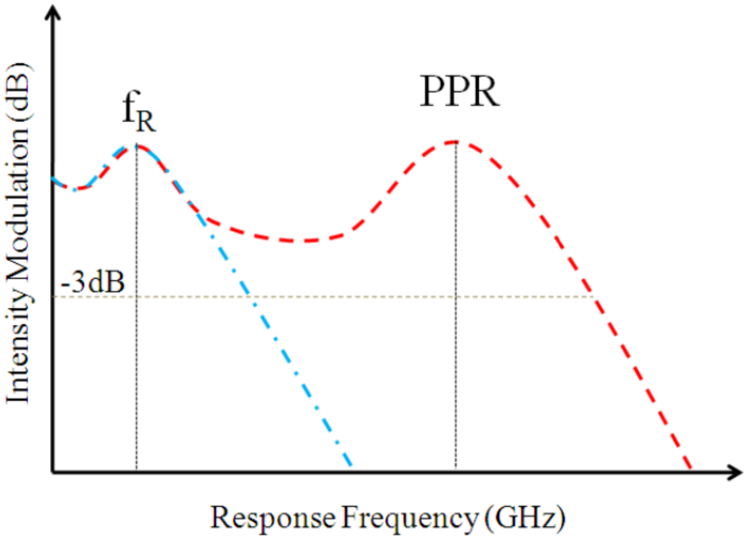

Fig.2-4. Small signal response with PPR effect [5]

The PPR effect has found widespread use in DBR lasers and DFB lasers. In 2016, Finisar[26] showcased a distributed reflector (DR) laser with a short cavity configuration, comprising a DFB laser integrated with a DBR section, as illustrated in Figure 2-5. By utilizing a 50µm gain length for the DFB section and a 200µm DBR section, a remarkable 3-dB modulation bandwidth of 55 GHz was achieved under a bias condition of 36.2 mA, as depicted in Figure 2-6.

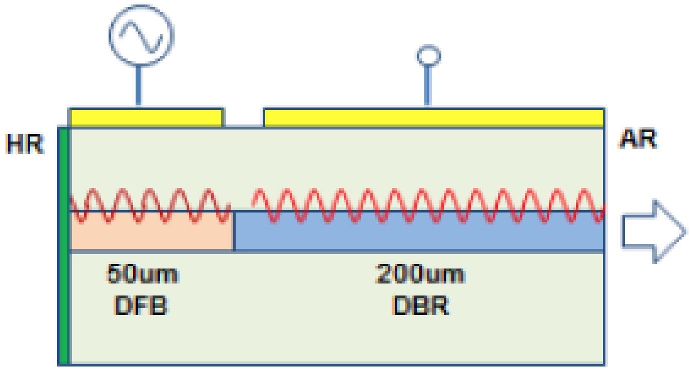

Fig.2-5. Schematic structure of DR laser [26]

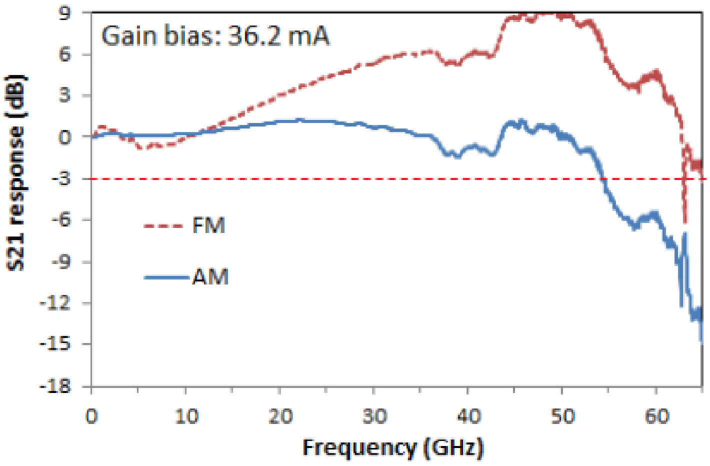

Fig.2-6. Small signal response of DR laser [26]

Yamaoka[27] demonstrated a lateral-current-injection membrane DR laser in 2020, featuring a DFB section, DBR, and output waveguide. The intricate structure is depicted in Figure 2-7. By harnessing the PPR effect, this configuration achieved an impressive 3dB modulation bandwidth of 108GHz at a bias current of 30mA, as illustrated in Figure 2-8. The utilization of a high-thermal-conductivity SiC substrate, with its capacity to support high values of bias current and possessing a high Γ factor, combined with the mitigation of damping effects and the incorporation of the PPR effect, enabled the expansion of the 3dB bandwidth to exceed 100GHz. This breakthrough offers a promising solution for low-power-consumption and high-capacity optical interconnects surpassing the capabilities of 400GbE. However, it is important to address the complexities associated with the structure and fabrication process, as well as the issue of mode instability, which arises from the precise control required for the passive feedback cavity in order to achieve single-mode operation.

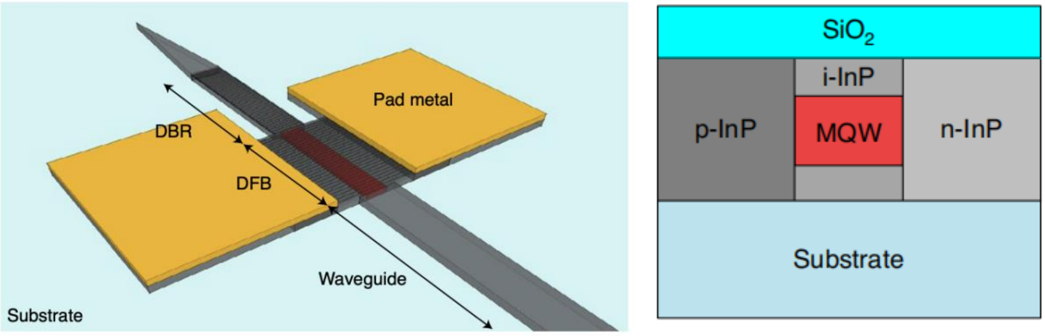

Fig.2-7. Schematic structure of membrane DR laser [27]

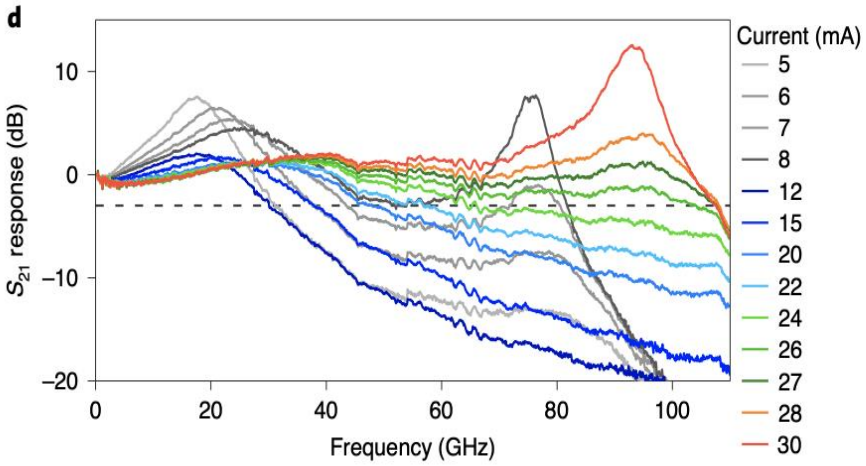

Fig.2-8. Small signal response of membrane DR laser [27]

2.2.2 Dynamic characteristics of VCSEL with PPR effect

A schematic structure of the VCSEL with the lateral optical feedback is shown in Fig. 2-9, where the VCSEL is laterally coupled with a TCC of length L_C through a bow-tie oxide aperture [22].

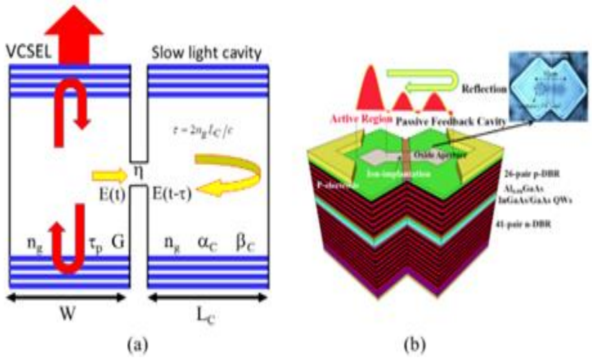

Fig.2-9. Schemes of (a) theoretical model and (b) TCC VCSEL [22]

The light is confined between the top and bottom mirrors of the VCSEL, resulting in a lateral zigzag propagation of the guided light. The coupling of light from a VCSEL to a Bragg reflector waveguide is achieved through a narrow oxide, leading to the perpendicular ambulation of light in the lateral direction, thereby inducing a slowing effect. For single-mode VCSELs, the group velocity (v_g) is significantly reduced by a factor exceeding 20. Specifically, light travels perpendicularly within the laterally coupled waveguide, exhibiting a slower group velocity (vg) given by $v_g = c / n_g$, where c represents the speed of light in vacuum, n_g corresponds to the group index calculated as the product of the average material refractive index n. The delay time (τ) accounts for the optical feedback. During each round trip within the transverse coupled cavity (TCC), the slow light experiences a loss factor and a phase delay factor, denoted by $\exp(-2\alpha_C Lc)$ and $\exp(-2j\beta_C Lc)$[5], respectively, where $\alpha_C = f\alpha_m$ and $\beta_C = 2\pi n/(f\lambda)$[5]. Here, α_m signifies the material loss, and λ represents the emission wavelength. Following each round trip, the slow light is injected into the VCSEL cavity with a coupling ratio η. The Optical Feedback (OFB) is considered as a time delay of the electric field associated with the slow light within the TCC, involving multiple round trips.

The rate equations of the TCC-VCSEL are as follow[5]:

$$\frac{dN}{dt} = \frac{\eta_i}{e} I(t) - \frac{N}{\tau_s} - \Gamma GS + f_N(t) \tag{1}$$

$$\frac{dS}{dt} = \left[\Gamma G - \frac{1}{\tau_p} + \frac{v_g}{W} \ln|U| \right] S + \Gamma R_{sp} + f_S(t) \tag{2}$$

$$\frac{d\theta}{dt} = \frac{1}{2}\left(\alpha\Gamma \frac{a}{V}(N - N_{th}) - \frac{c}{n_g W}\varphi \right) + f_\theta(t) \tag{3}$$

Due to this slow-light feedback, the threshold gain G_{th} of the VCSEL is modified to[5]:

$$G_{th} = G_{tho} - \frac{c}{n_D L_D} ln|U(t-\tau)|$$

where U(t-τ) is represented the time-delay function. By applying modulated current, we can obtain the small signal response of the TCC-VCSEL. In Fig. 2-10, the small signal response of the TCC-VCSEL with a 20μm coupled cavity and different coupling efficiency is compared to that of the conventional VCSEL. When modulation is applied, a peak corresponding to carrier-photon resonance (CPR) emerges at approximately 14GHz, and the 3-dB modulation bandwidth is around 23 GHz, as shown in curve a. When strong optical feedback is introduced, leading to photon-photon resonance (PPR), the small signal response can be extended to approximately 51GHz with a coupling efficiency of 96%. This PPR arises from modulation frequencies close to the beating frequencies of oscillating modes in the external cavity. Besides, the bandwidth enhancement is related to the coupling strength as shown in Fig. 2-11.

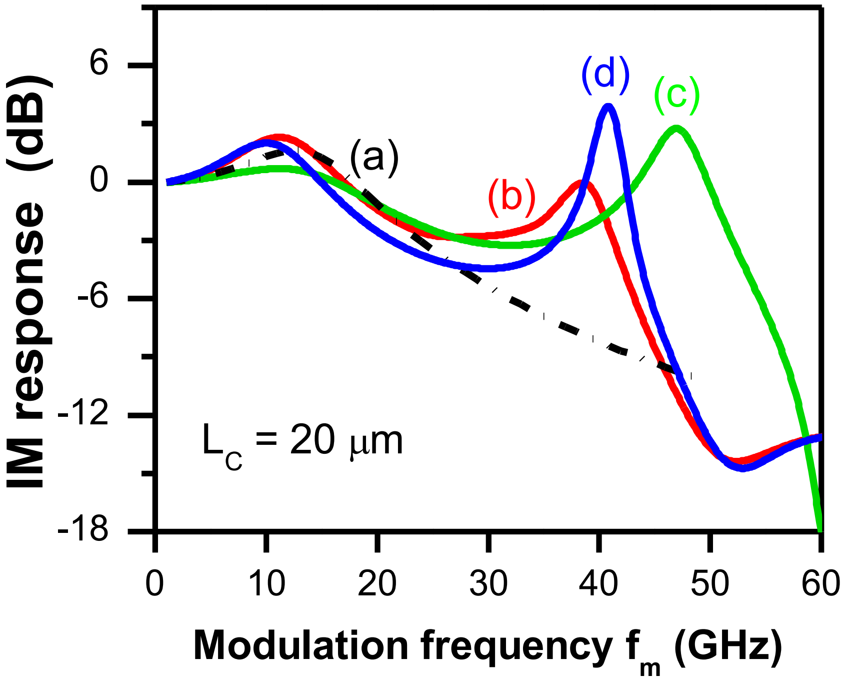

Figure 2-10. Small-signal modulation response of the TCC VCSEL when LC = 20 when η= 0.7 (curve b), η= 0.96 (curve c) and η= 0.77 (curve d). The IM response of the VCSEL, η= 0 (curve a) is plotted for comparison[4].

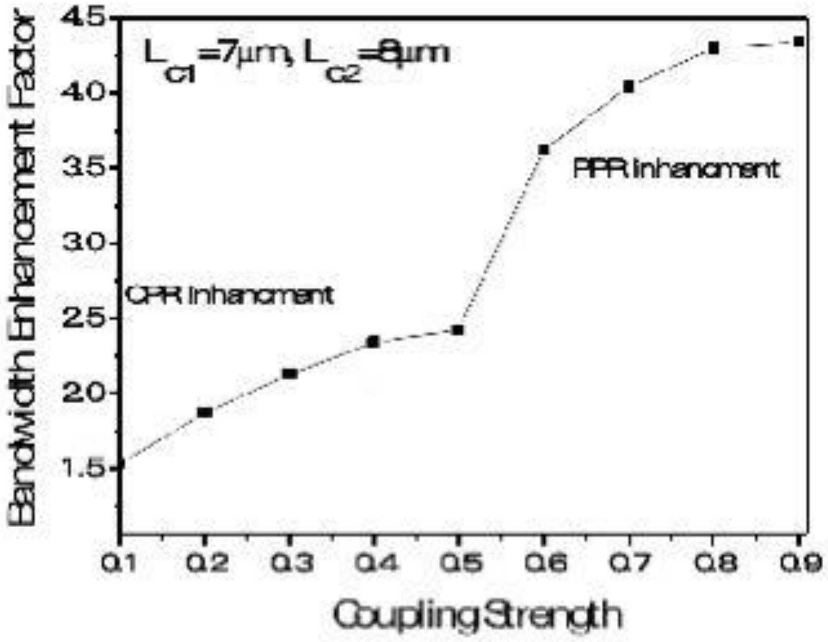

Figure 2-11. Bandwidth enhancement factor changed by coupling strength[4]

2.3 Principle of mode control and bandwidth enhancement process

2.3.1 Towards small oxide aperture VCSEL

As illustrated in Chap 1.2, Hameeda[28] demonstrated a metal-aperture half-cavity VCSEL, showcasing its ability to achieve 60Gbps PAM4 and 40Gbps NRZ modulations. The metal aperture within the cavity serves as transverse coupled cavities, enabling both single-mode operation and enhanced bandwidth in the modulation response. The spacing between the metal electrode and oxide aperture serves as an ultrashort external cavity, as depicted in Figure 2-12(a). The small signal response was analyzed using the rate equation model with optical feedback, considering both the presence and absence of the coupled cavity effect [29].

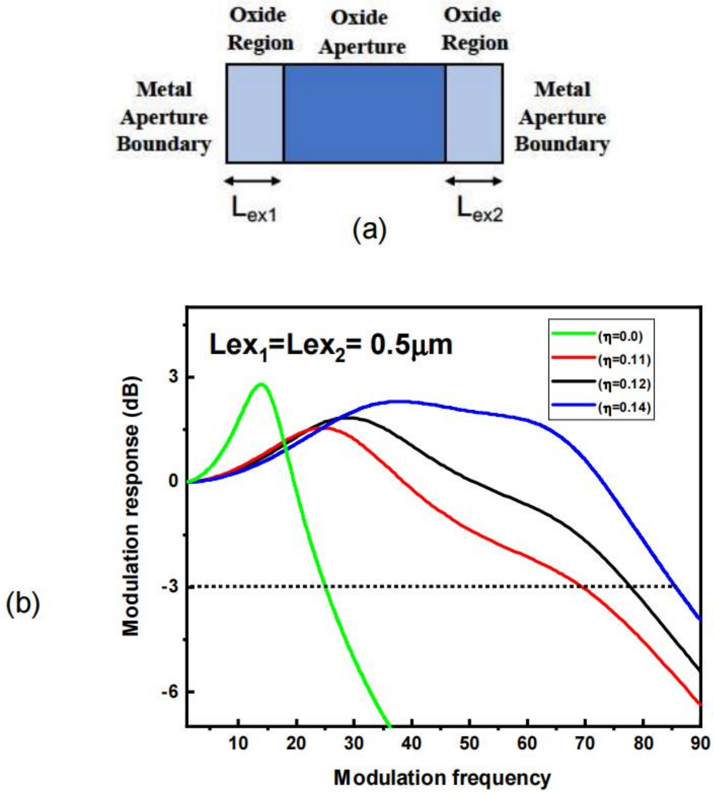

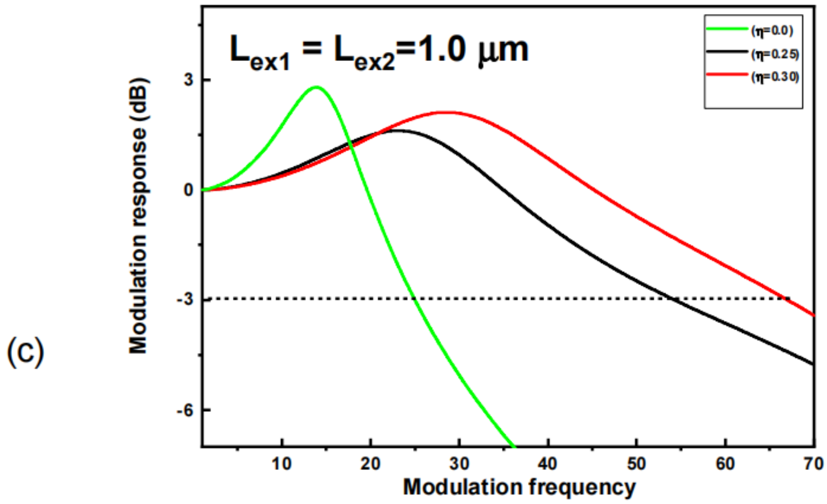

Fig. 2-12. Calculated small signal response of coupled-cavity VCSEL with external cavity length of (b) 0.5µm and (c) 1µm including conventional VCSEL (C-VCSEL) for comparison.[29]

The calculated results for different cavity lengths are depicted in Figures 2(b) and (c). Due to the coupled cavity effect, the modulation bandwidth increases by more than threefold compared to conventional VCSELs. Coupled cavities with dimensions smaller than 2µm facilitate stable bandwidth enhancement and enable single transverse mode operations, as illustrated in Figure 2-12.

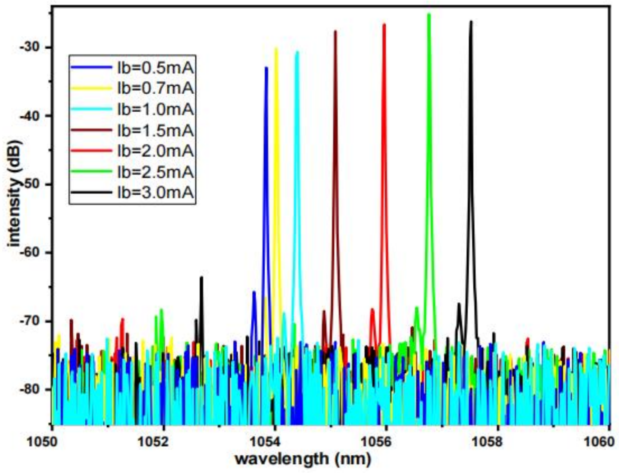

Fig. 2-12. Calculated small signal response of coupled-cavity VCSEL with external cavity[29]

2.3.2 Towards large oxide aperture VCSEL

For achieving transverse coupled cavity and mode control in short cavity VCSELs, the utilization of a metal-aperture surface process proves to be promising. However, when it comes to long cavity VCSELs, Hassan et al.[30] demonstrated the effectiveness of a surface grating VCSEL for achieving single mode operation, as depicted in Figure 2-13. The stability of the single mode is maintained even with increased cavity length, as illustrated in Figure 2-14. Notably, unlike DFB lasers, the grating in VCSELs can be fabricated directly on the surface. In 2021, Hassan et al.[31] conducted a successful demonstration of stable single mode operation in a full-cavity VCSEL incorporating a surface grating with a length of 6 mm as shown in Fig. 2-15. This achievement also enabled high power applications with an output power exceeding 6 W. However, the investigation of surface grating VCSELs with cavity lengths of less than a hundred micrometers remains unexplored, potentially offering new possibilities for high-speed applications.

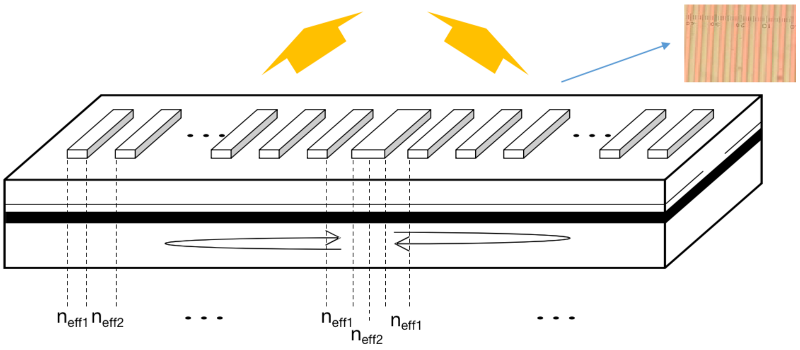

Fig. 2-13. Surface grating loaded VCSEL

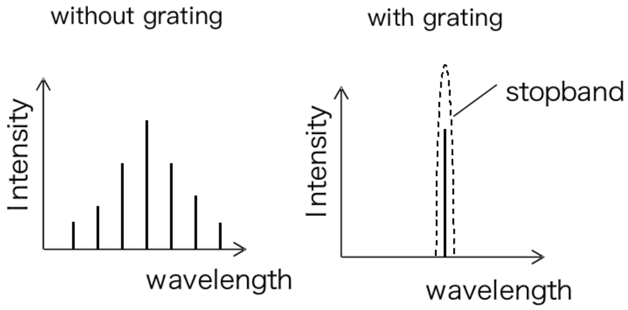

Fig. 2-14. Spectrum of VCSEL with and without the surface grating[30]

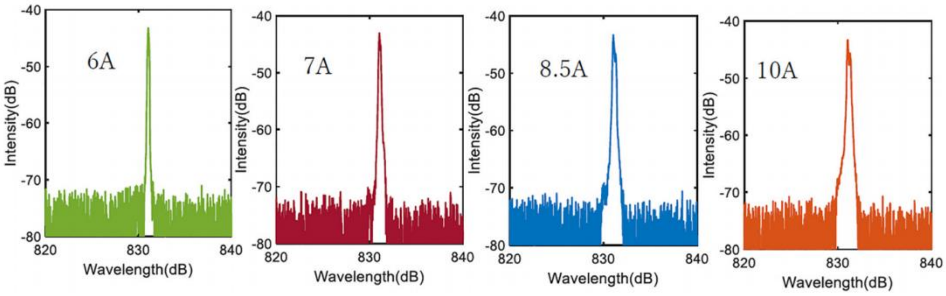

Fig. 2-15. Spectrum of VCSEL with 6mm cavity length at different current amplitude of 50ns pulse[31]

With the aim of achieving high-speed applications, our intention is to design a half-cavity VCSEL loaded with a grating and coupled cavity configuration. This design will allow for higher output power and modulation bandwidth. Furthermore, the incorporation of a half-cavity structure brings the surface grating closer to the active region. By carefully adjusting various grating parameters, such as grating height and depth, we can effectively control the lateral coupling strength.

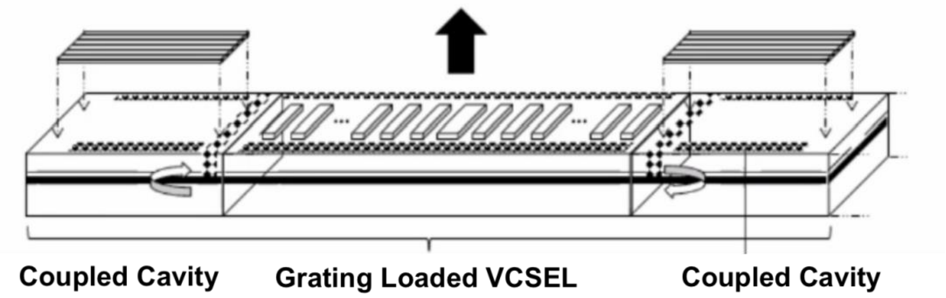

Fig. 2-16. Spectrum of VCSEL with and without the surface grating

Reference in Chapter 2

1) G. Steinle, “High Bandwidth VCSELTechnology and Industrial Applications,” VCSEL Technology EPIC Online Technology Meeting (2021).

2) L. A. Coldren, S. W. Corzine, Diode lasers and photonic integrated circuits, 2012, p.195-207.

3) R. Michalzik, VCSEL fundamentals, 2013, p.235-241.

4) Hameeda Ragab Ibrahim. Study on High-speed Transverse Coupled Cavity VCSELs. 2019

5) Hamed Dalir. Study on High Speed VCSELs Based on Lateral Resonator Integration for Optical Interconnects. 2014

6) K.L. Lear, V.M. Hietala, H.Q. Hou, M. Ochiai, J.J. Banas, B.E. Hammons, J.C. Zolper, S.P. Kilcoyne, Small and large signal modulation of 850 nm oxide-confined vertical cavity surface emitting lasers, in OSA Trends in Optics and Photonics, Advances in Vertical Cavity Surface Emitting Lasers, vol. 15, ed. by C.J. Chang-Hasnain (Optical Society of America, Washington, DC, 1997), pp. 69–74

7) Demeulenaere, Bart, et al. "Detailed study of AlAs-oxidized apertures in VCSEL cavities for optimized modal performance." IEEE journal of quantum electronics 35.3 (1999): 358-367.

8) Hawkins, Bobby M., et al. "Reliability of various size oxide aperture VCSELs." 52nd Electronic Components and Technology Conference 2002.(Cat. No. 02CH37345). IEEE, 2002.

9) Ohiso, Y., et al. "Single transverse mode operation of 1.55-µm buried heterostructure vertical-cavity surface-emitting lasers." IEEE Photonics Technology Letters 14.6 (2002): 738-740.

10) Chang-Hasnain, C. J., et al. "Low threshold buried heterostructure vertical cavity surface emitting laser." Applied physics letters 63.10 (1993): 1307-1309.

11) Song, Dae-Sung, et al. "Single-fundamental-mode photonic-crystal vertical-cavity surface-emitting lasers." Applied Physics Letters 80.21 (2002): 3901-3903.

12) Danner, Aaron J., et al. "Transverse modes of photonic crystal vertical-cavity lasers." Applied Physics Letters 84.7 (2004): 1031-1033.

13) Min, Szu-Yu, et al. "Oxide-confined VCSEL with metal apertures for high-speed 850nm transmission." 2020 Opto-Electronics and Communications Conference (OECC). IEEE, 2020.

14) Ibrahim, Hameeda R., et al. "Single-mode and high-speed intracavity metal aperture VCSEL with transverse coupled cavity effect." 2020 European Conference on Optical Communications (ECOC). IEEE, 2020.

15) Unold, Heiko J., et al. "Large-area single-mode VCSELs and the self-aligned surface relief." IEEE Journal of Selected Topics in Quantum Electronics 7.2 (2001): 386-392.

16) Martinsson, H., J. A. Vukusic, and A. Larsson. "Single-mode power dependence on surface relief size for mode-stabilized oxide-confined vertical-cavity surface-emitting lasers." IEEE Photonics Technology Letters 12.9 (2000): 1129-1131.

17) Majewski, Marian L., and Dalma Novak. "Method for characterization of intrinsic and extrinsic components of semiconductor laser diode circuit model." IEEE microwave and guided wave letters 1.9 (1991): 246-248.

18) Grabmaier, A., et al. "Carrier transport limited bandwidth of 1.55 μm quantum-well lasers." Applied physics letters 62.1 (1993): 52-54.

19) Ralston, John D., et al. "Control of differential gain, nonlinear gain and damping

factor for high-speed application of GaAs-based MQW lasers." IEEE Journal of quantum electronics 29.6 (1993): 1648-1659.

20) Simpson, T. B., and J. M. Liu. "Enhanced modulation bandwidth in injection-locked semiconductor lasers." IEEE Photonics Technology Letters 9.10 (1997): 1322-1324.

21) Takatsuji, M. "Theory of coherent two-photon resonance." Physical Review A 11.2 (1975): 619.

22) Dalir, Hamed, and Fumio Koyama. "High-speed operation of bow-tie-shaped oxide aperture VCSELs with photon–photon resonance." Applied Physics Express 7.2 (2014): 022102.

23) Uusitalo, Topi, et al. "Analysis of the photon–photon resonance influence on the direct modulation bandwidth of dual-longitudinal-mode distributed feedback lasers." Optical and Quantum Electronics 49 (2017): 1-14.

24) Bardella, Paolo, Weng W. Chow, and Ivo Montrosset. "Design and analysis of enhanced modulation response in integrated coupled cavities DBR lasers using photon-photon resonance." Photonics. Vol. 3. No. 1. MDPI, 2016.

25) Bardella, Paolo, and Ivo Montrosset. "A new design procedure for DBR lasers exploiting the photon–photon resonance to achieve extended modulation bandwidth." IEEE Journal of Selected Topics in Quantum Electronics 19.4 (2013): 1502408-1502408.

26) Matsui, Yasuhiro, et al. "55-GHz bandwidth short-cavity distributed reflector laser and its application to 112-Gb/s PAM-4." Optical Fiber Communication Conference. Optica Publishing Group, 2016.

27) Yamaoka, Suguru, et al. "Directly modulated membrane lasers with 108 GHz

bandwidth on a high-thermal-conductivity silicon carbide substrate." Nature Photonics 15.1 (2021): 28-35.

28) Ibrahim, Hameeda R., et al. "1060nm Single-mode Metal-aperture VCSEL Array with Transverse Resonance and Low Power Consumption below 50 fJ/bit." 2021 European Conference on Optical Communication (ECOC). IEEE, 2021.

29) H. Ibrahim, M. Ahmed, F. Koyama, “High speed modulation single mode 850 nm DTCC-VCSEL”. 300-301. MOC, Nov.2019.

30) Hassan, Ahmed MA, et al. "High power and high beam quality surface grating VCSEL." CLEO: Science and Innovations. Optica Publishing Group, 2021.

31) Hassan, Ahmed, et al. "High-power operations of single-mode surface grating long oxide aperture VCSELs." Applied Physics Letters 119.19 (2021).

Chapter 3

Metal-aperture and surface relief for high speed VCSEL

In this chapter, the details about principle, surface design, fabrication process and experimental characteristics of metal-aperture and surface relief VCSEL will be discussed. The introduction of parasitic optimization process will also be shown.

3.1 Intra-cavity metal-aperture VCSEL

3.1.1 Principle of intra-cavity metal-aperture VCSEL

The schematic of intra-cavity metal-aperture VCSEL is shown in Fig. 3-1. It was fabricated based on the half-cavity VCSEL wafer. In my study, I chose to use the epi wafer with resonance wavelength of 1060nm. The half-cavity VCSEL wafer used was deposited by metal-organic chemical vapor deposition (MOCVD) on the GaAs substrate. The $Al_xGa_{1-x}As$ layers with different x and thickness are repeatedly deposited to form the top and bottom distributed bragg reflector (DBRs). The 4 pairs of 5-nm/10-nm $In_{0.25}Ga_{0.75}As/GaAs$ quantum wells (QWs), which is compatible for 1060nm-band lasing, are sandwiched by the 4-pair of top DBRs and 30-pair of bottom DBRs. By increasing the number of quantum wells and decreasing their thickness, the effective confinement factor ($\Gamma=0.0406$) can be improved, thereby increasing the modulation bandwidth. Since the half-cavity VCSEL with insufficient top reflectivity, a Ta2O5/SiO2 top dielectric DBRs, consisting of 5 pairs, is deposited on the surface to achieve sufficient top reflectivity which is around 99%. A ring-shaped p-contact metal is evaporated on the surface of the half-cavity VCSEL with a different diameter and line width. Subsequently, a shallow-wet etching process is carried out at the center of the metal-ring. The round-oxidized mesa is formed via dry etching. The top view of the mesa is shown in Fig. 2-1(b). The CMin and CMout represent the inner and outer diameter of p-contact metal ring. Respectively. The semiconductor surface relief enables transverse resonance in intra-cavity metal-aperture VCSELs, resulting in bandwidth enhancement and transverse mode control [27, 29]. Because the surface relief region has a shorter resonance wavelength than the un-etched region, lasing light can laterally travel into the oxidized region and is reflected by the metal-aperture boundary [27], resulting in transverse resonance. To achieve single-mode operation and bandwidth enhancement via transverse coupled cavity effect, the distance between the metal electrode and oxidation aperture should be no more than 1μm.

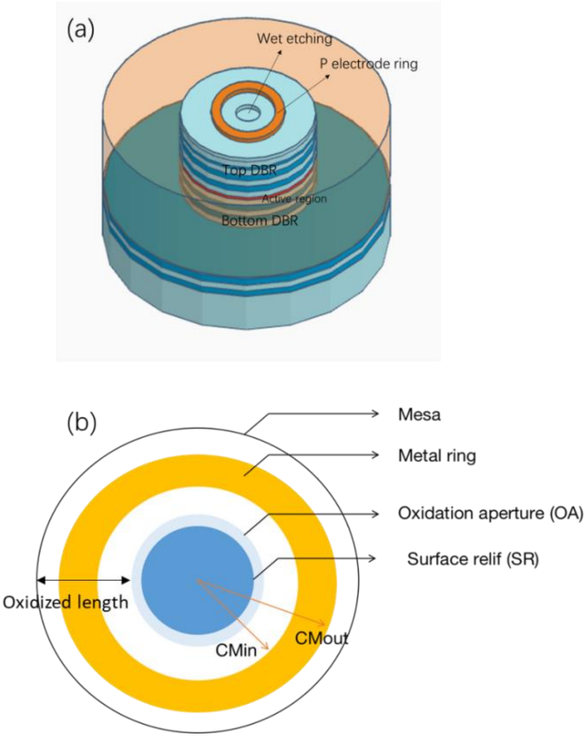

Fig. 2-1. The schematic of intra-cavity metal-aperture VCSEL

3.1.2 Fabrication process of full 3-inch wafer based intra cavity metal-

aperture VCSEL

The fabrication process of intra-cavity metal-aperture VCSEL is compatible with standard VCSEL massproduction process. It will go through wafer growth, p-contact metal evaporation and wet etching for surface relief region (just these two steps surface engineered process difference), SiO_2 protect layer deposition, inductively coupled plasma (ICP) dry etching for mesa form, wet oxidation, polyimide passivation, wet etching for n-contact window, SiO_2 protect layer etching to expose p-contact metal, n-electrode and p-electrode evaporation, dielectric DBRs deposition. In my study, the process of wet etching and dielectric DBRs patterning will be finished. The wafer growth and other processes were finished by external foundry. The fabrication process flow is shown in Fig. 3-4. The parameter of p-contact metal, surface relief (SR), and oxidation aperture (OA) diameter are shown in Table 3-1. There are 4 types of the mesa diameter ranges from 15μm to 18μm, and the oxidation length should be 5μm, which means the oxidation aperture are 5μm, 6μm, 7μm, 8μm, respectively. The surface relief diameter are 2 types: -1μm and +0μm based on the oxidation aperture diameter. For each mesa design, there are 4 types of contact metal ring: +1μm, +2μm, +3μm, and +4μm based on the oxidation aperture diameter with the distance between oxidation aperture and CMin of 0.5μm, 1μm, 1.5μm, and 2μm, and with 3.5μm, 3μm, 2.5μm, and 2.5μm line width, respectively.

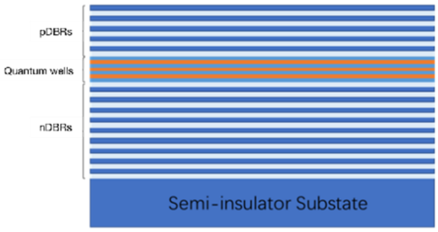

1. Wafer growth

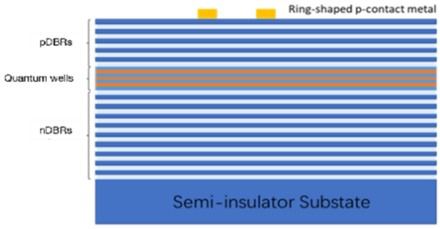

2. P-contact metal

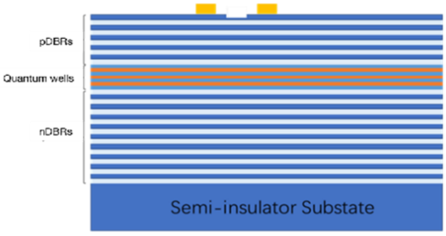

3. Surface relief etching

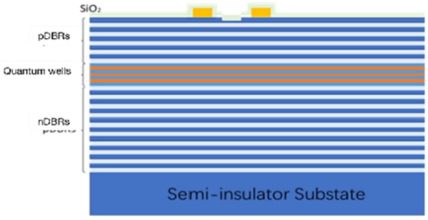

4. SiO_2 sputtering

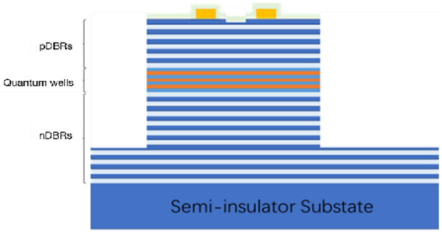

5. ICP mesa etching

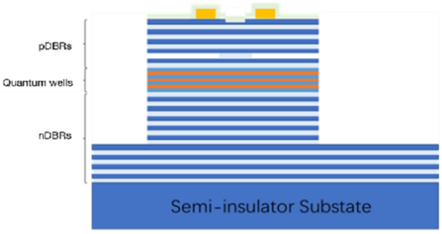

6. Oxidation

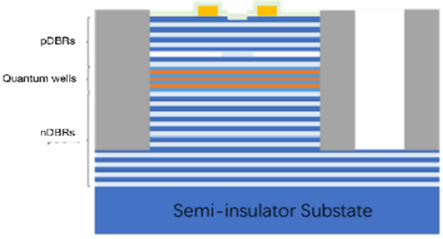

7. Polyimide passivation

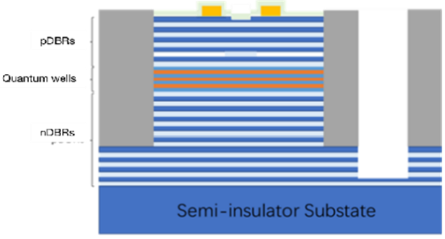

8. N-contact etching

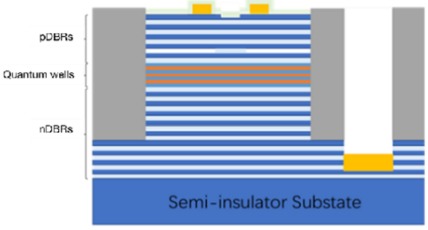

9. N-contact metal

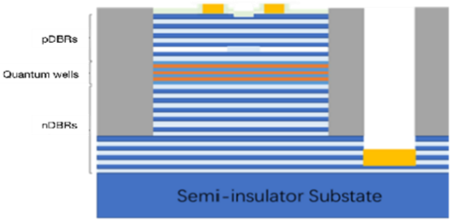

10. SiO_2 etching

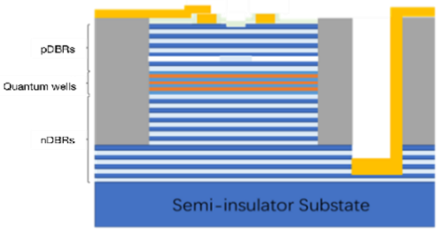

11. N-electrode and P-electrode

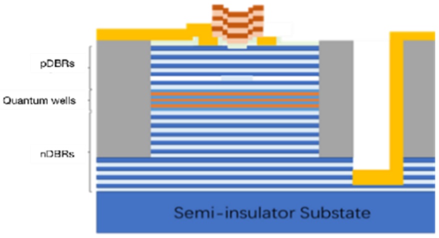

12. Dielectric DBR

Fig. 3-4. Fabrication process flow of intra-cavity metal-aperture VCSEL

Table 3-1. Parameter of p-contact metal, surface relief, and oxidation apertrue

Diameter	Value(μm)															
Mesa	15				16				17				18			
OA	5				6				7				8			
SR	4/5				5/6				6/7				7/8			
CMin	6	7	8	9	7	8	9	10	8	9	10	11	9	10	11	12
CMout	13	13	13	14	14	14	14	15	15	15	15	16	16	16	16	17

① The 3-inch half-cavity VCSEL wafer was finished by MOCVD. Since the fabrication process of intra-cavity metal-aperture VCSEL is almost same as the standard fabrication process. Full 3-inch fabrication process can be realized and with good uniformity. This could be benefit for massproduction and application.

② P-contact metal: The resist patterning should be realized to form the selective region. The region that we want to deposited the metal should be exposed, and the other region should be protected. We use PMGI and AZ5200NJ for the photoresist and coating it on the whole wafer by spin coating. The photoresist should be baked to solidify the material. Then, the photomask applied to form the shape we wanted, the photoresist of exposed region could be easily removed by AZ developer after exposure. The coating, exposure, and developing condition are shown in table 3-1. The ring-shaped p-contact metal should be firstly deposited for the transverse resonance by evaporation. The evaporation composition and thickness are shown in table 3-2. The Ti need to be alloyed with contact layer to decrease the resistance by annealing. After metal evaporation, the resist can be removed by PMGI, and the electrode on the unintended region could be lift off.

Table 3-2. Coating, exposure, and developing condition for p-contact metal patterning

Process	Condition
Spin coating	Speed: 4000rpm for 30s
Baking	Time: 90s
Exposure	Time: 7.6s
Developing	Time: 35s

Table 3-3. Evaporation composition and thickness for p-contact metal

Metal	Thickness
Ti	3nm
Au	1000nm

③ Surface relief etching: The photoresist of surface relief patterning is AZ 1500, the patterning condition is shown in table 3-4. The surface relief is formed by applying wet etching with 80ml H_2O + 8 drops H_2O_2 + 1 drop H_2SO_4. The depth of surface relief is 15, 20, and 30nm. With this shallow etching depth, the speed of etching need to be reduced. By changing the H_2O_2 and H_2SO_4 from ml to drop, the etching speed can be down to around 30nm/min. The surface relief pattern should be located at the center of the ring contact metal.

Table 3-4. Coating, exposure, and developing condition for surface relief

Process	Condition
Spin coating	Speed: 3000rpm for 20s
Baking	Time: 90s
Exposure	Time: 3.9s

Developing	Time: 5s

④ SiO_2 sputtering: The surface wafer is very sensitive and easy to be defected during the remining process. It’s important to protect the surface by SiO_2 layer with 100nm depth by sputtering.

⑤ ICP mesa etching: The ICP dry etching is used to form the round-shaped mesa pattern which with the same circle center as metal ring and surface relief to enable round-shaped and center-located oxidation aperture. The mesa etching will etch down to the n-type bottom DBR region. Since the surface is covered by SiO_2, we need to first coat the photoresist of OAP to stick the AZ 5200NJ with SiO_2, and then coat the resist AZ 5200NJ. The AZ developer is used to remove the resist after exposure. The spin coating and exposure condition are shown in table. 3-5. After patterning, the SiO_2 at exposed region need to be removed to enable ICP dry etching by using BHF. After ICP dry etching, we use the Acetone, 502A, and oxygen plasma etching to remove the resist. Since sometimes the resist could be hardly to remove, it’s better to use 502A solution and oxygen plasma etching to remove completely.

Table 3-5. Coating, exposure, and developing condition for mesa patterning

Process	Condition
Spin coating	Speed: 4000rpm for 20s
Baking	Time: 90s
Exposure	Time: 6.7s
Developing	Time: 60s

⑥ Oxidation: There is an oxidation layer buried in the wafer with AlAs, and this layer can be oxidized with flooding water carried by nitrogen at high temperature. Since the oxidized length is just 5μm which is rather small, the speed needs to be controlled and the temperature need to be reduced. In my study, the temperature was at 340°C to reduce the oxidation speed to around 0.085μm/min.

⑦ Polyimide passivation: The polyimide layer should be formed to protect the side wall of the mesa and support the p-electrode pad and n-electrode pad. The polyimide can be formed by spin coating as the photoresist. The difference is that the unexposed region will be developed. The spin coating, exposure, and developing condition is shown in table 3-6. After exposure, the post exposure bake is needed to stabilize the material. After developing, the height could be around 5μm. The height can be adjusted by the speed of spin coating. Then, the polyimide is still in an uncured state and requires further curing to enhancing the stability and optimizing the properties. It processed at 340°C by nitrogen atmosphere for 50min. After cure, the height of polyimide could be around 2μm reduced which is almost the mesa height. If the height of polyimide is higher or lower too much than the mesa height, the electrode may disconnect at edge of the mesa.

Table 3-6. Coating, exposure, and developing condition for polyimide

Process	Condition
Spin coating	Speed: 4000rpm for 30s
Baking	Time: 4min
Exposure	Time: 30s
Post exposure bake	Time: 60s
Developing	Time: 1min 40s

⑧ N-contact etching: To open the window of n-contact region, wet etching process is used to etch down to near the substrate about several micrometers. With this deep etching depth, the etching solution should be: 80ml H_2O + 8ml H_2O_2 + 1ml H_2SO_4 to realize the faster etching speed around 1.2μm/min.

⑨ N-electrode and P-electrode evaporation: Since the p-contact and n-contact metal have been deposited. The n electrode and p electrode can be formed simultaneously by 500nm Au. The photoresist and exposure condition is same as the contact metal ring process. Before the electrode evaporation, the SiO_2 on the surface of the p-contact metal should be removed by BHF solution. The etching time is around 1min.

⑩ Dielectric DBR: For half-cavity VCSEL, the dielectric DBR is formed on the mesa to ensure sufficient reflectivity. The photoresist is same as electrode evaporation patterning process. The spin coating speed is 3000rpm for 30s, the exposure time is 10s. Then, 5 pairs of SiO_2/ Ta_2O_5 are deposited on the surface of the mesa.

3.2 Characteristics of intra-cavity metal-aperture VCSEL

3.2.1 Electrical and optical characteristics of intra-cavity metal-aperture VCSEL

The photo of full 3-inch processed wafer and the fabricated device is shown in Fig. 3-4. The device length is around 200nm. The p-contact metal ring and surface relief feature can be seen in the Fig. 3-4(b). The exact length of the metal ring, surface relief, oxidation aperture, and mesa are shown in table 3-1. The depth of surface relief is 15nm. The first assessment of the intra-cavity metal-aperture VCSEL is the electrical and optical properties including the threshold current, voltage, optical power, and lasing spectrum.

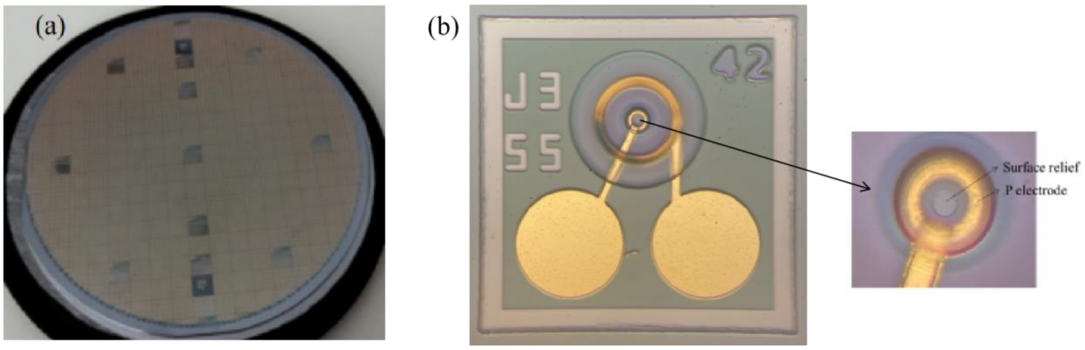

Fig. 3-4. Photo of 3-inch processed wafer and fabricated device

The electrical and optical characteristics could be measured by VCSEL laser tester as shown in Fig. 3-5. Fig. 3-5 shows the relation of voltage versus injected current with 5μm oxidation aperture diameter and different CMin parameter. Because of the high p-doping level and the fabrication process, the voltage is around 2.9V at 6mA bias current. This high voltage can be avoided by modify the n-electrode contact window to reduce the series resistance and reduce the p-doping level, the voltage can be reduced to around 2.2V at 6mA bias current as shown in Fig. 3-6. With larger contact metal ring CMin, the metal ring linewidth reduced which lead to higher voltage.

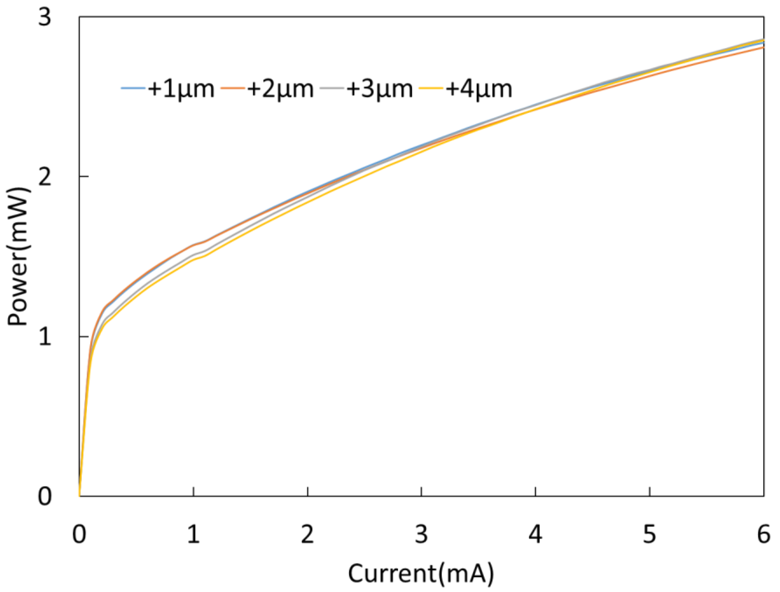

Fig. 3-5. Measured voltage versus injected current with 5μm oxidation aperture

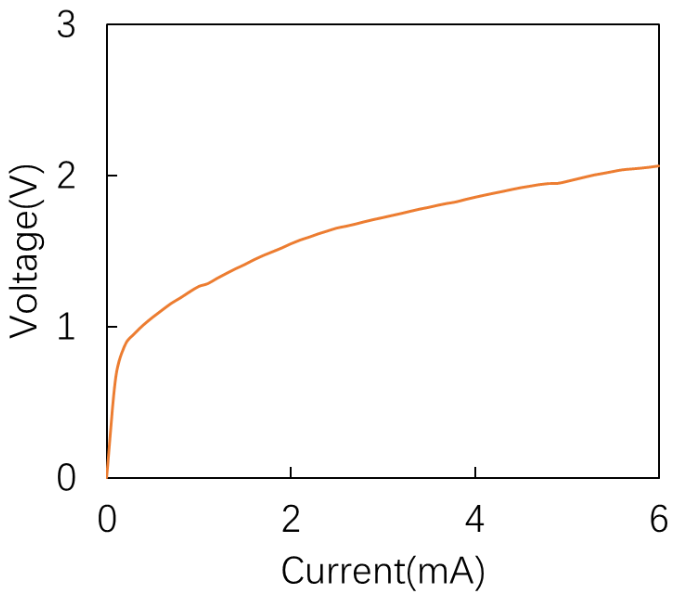

Fig. 3-6. Measured voltage versus injected current with 5µm oxidation aperture

Fig. 3-7 shows the optical power - injected current. The threshold current is around 0.7mA. The output power is around 2.5mW at 6mA with 47% slope efficiency. With the larger CMin, the metal absorption could be reduced and the power has a slighly increased as shown in the figure.

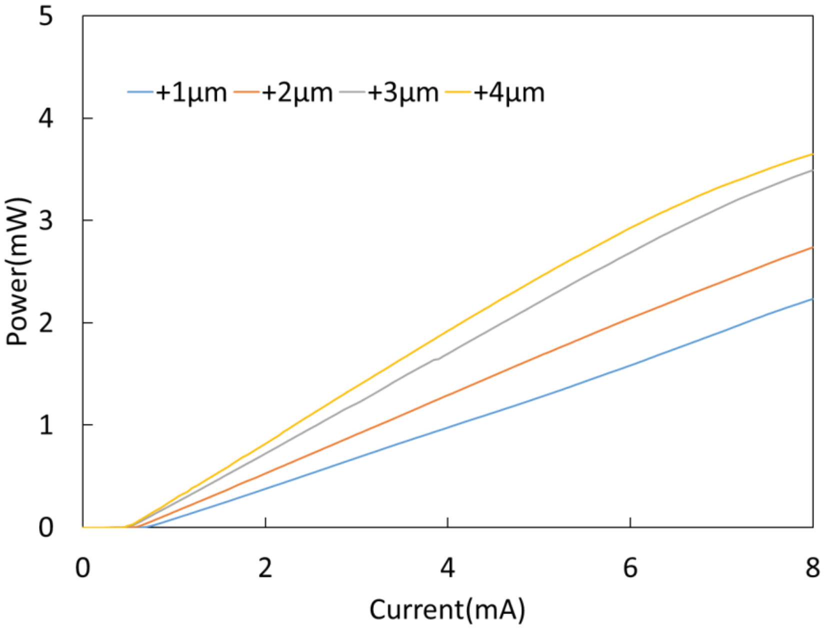

Fig. 3-7. Measured output power versus injected current with 5µm oxidation aperture

Fig. 3-8 shows the comparison of lasing spectrum with conventional VCSEL and intra-cavity metal-aperture VCSEL of 5μm oxidation aperture. These devices are all fabricated on the same wafer, the difference is the contact metal ring. Compared to the conventional VCSEL as shown in Fig. 3-8(a), multi-mode operation can be seen even at 4mA with less than 5dB SMSR, the stable single mode can be realized at the entire current range of intra-cavity metal-aperture VCSEL as shown in Fig. 3-8(b). Stable single mode operation can be realized at the entire current range with larger than 40dB SMSR. These are because of the transverse mode control thanks to the surface relief and metal aperture process.

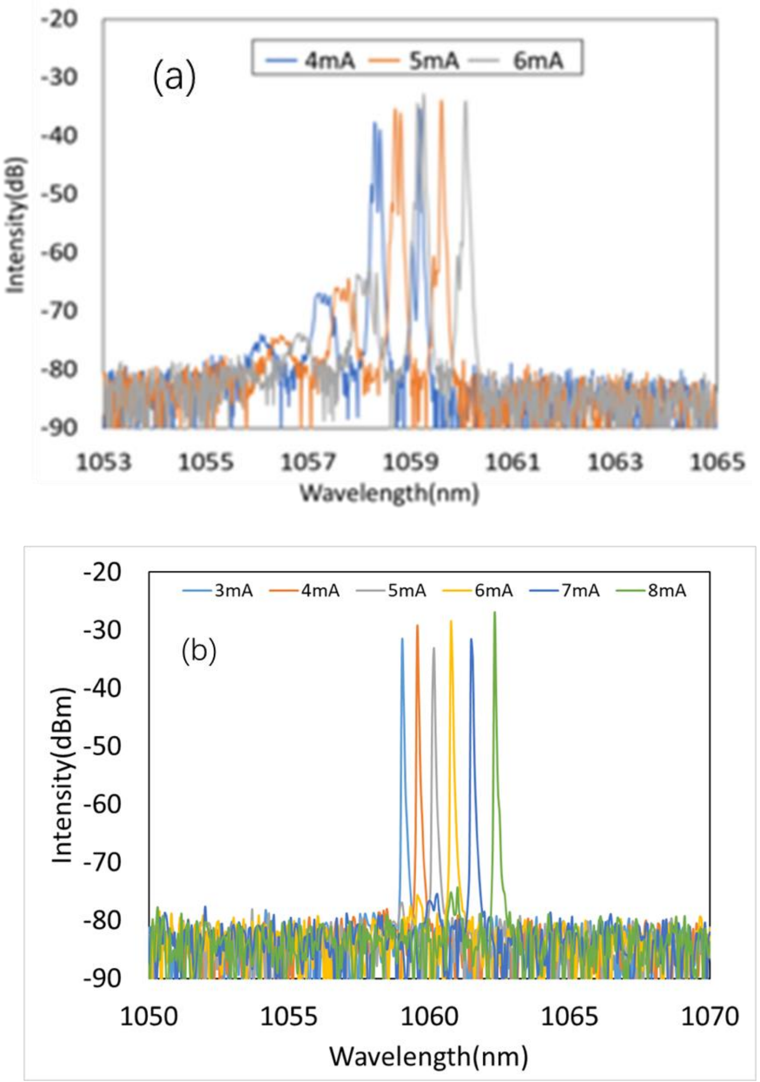

Fig. 3-8. Spectrum of conventional VCSEL and intra-cavity metal-aperture VCSEL with

5μm oxidation aperture

There are two designs of surface relief depth: 15nm and 30nm. By changing the grating depth, the transverse mode control can be changed. Besides, the spectrum is fitting to the changes of surface relief depth at 6mA bias current as shown in Fig. 3-9. These are fabricated on the same wafer, the only difference is the depth of the surface relief. With 30nm depth, the lasing wavelength will have a 2nm deviation of the 15nm depth.

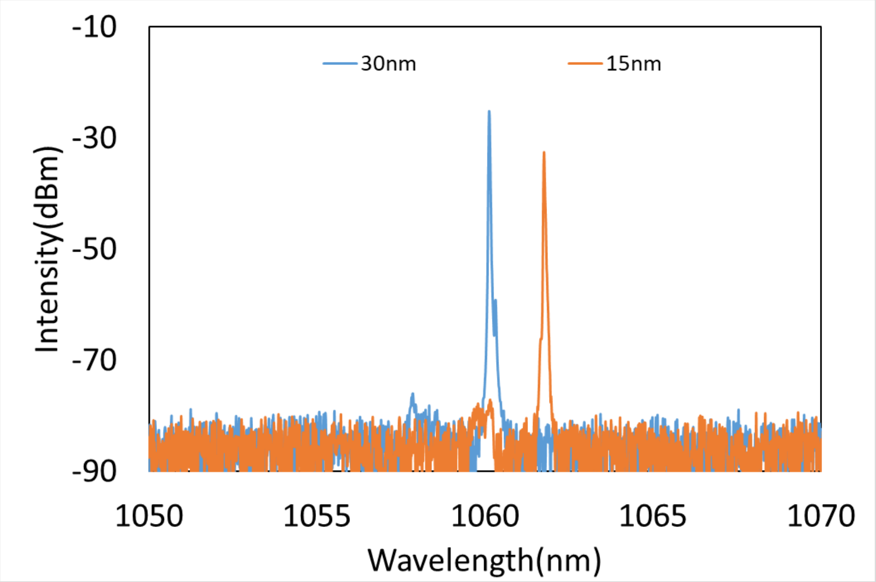

Fig. 3-9. Spectrum of intra-cavity metal-aperture VCSEL with 15nm and 30nm surface relief depth

In general, the grating depth with 30nm which means stronger coupling strength shows better single mode condition. The spectrum comparison of 5μm oxidation aperture, +1μm and +2μm of contact metal CMin, with 15nm and 30nm depth of surface relief are shown in Fig. 3-10. With 15nm depth of surface relief as shown in Fig. 3-10(a) and Fig. 3-9(b). Single mode operation can be realized with +1μm of contact metal because of the metal absorption. When the CMin increased to +2μm, although the single mode operation with larger than 40dB SMSR can be obtained at low current, high order mode will appear at 6mA with 10dB SMSR. The weak coupling strength can just maintain the single mode operation at very low current. When increasing the depth to 30nm as shown in Fig. 3-9(c) and Fig. 3-10(d), single mode operation with larger than 30dB SMSR at entire current range can be obtained for 5μm oxidation aperture with +1μm and +2μm contact metal CMin. Therefore, by increasing the depth of surface relief is an effective way to increase the transverse mode control.

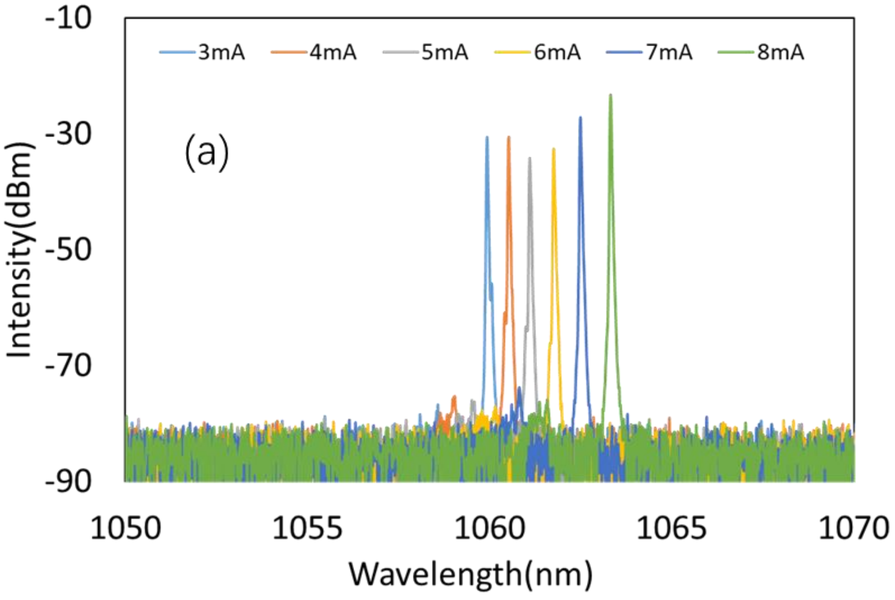

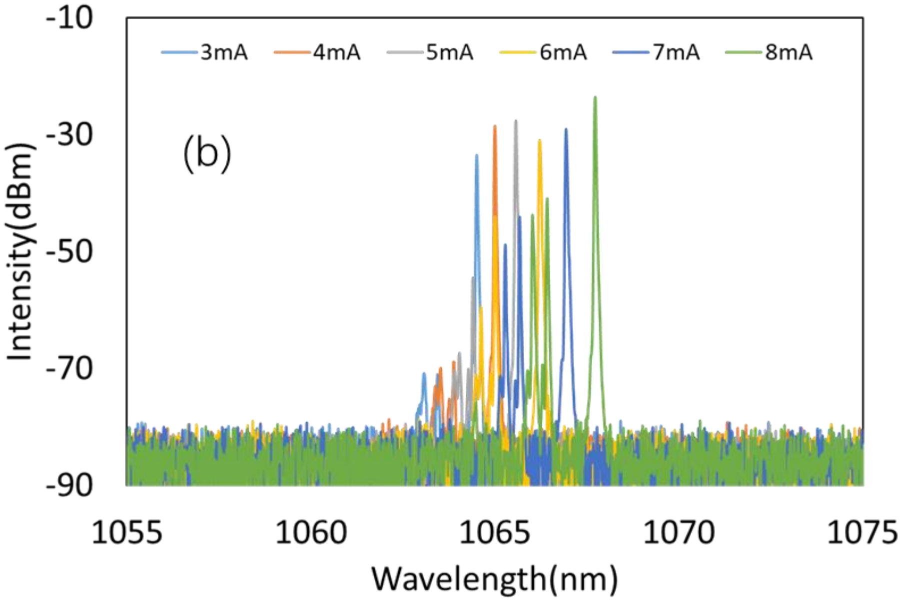

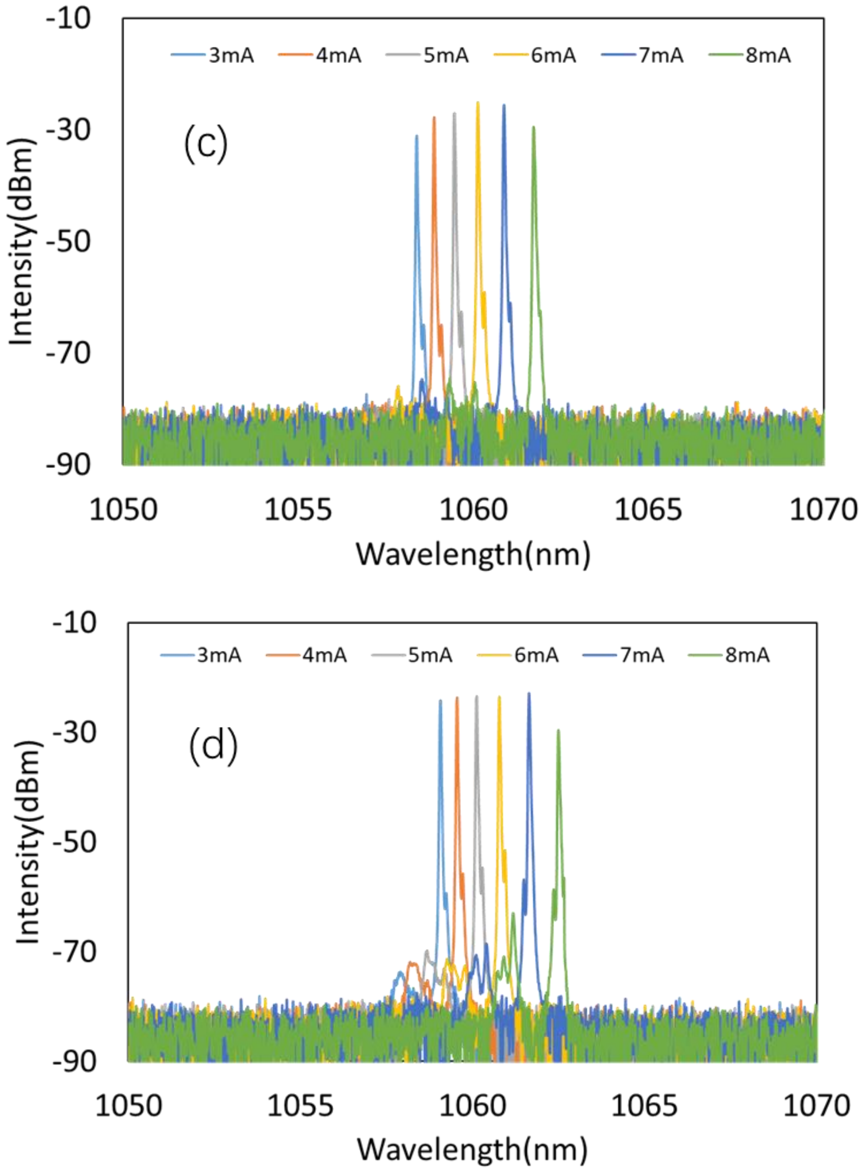

Fig. 3-10. Spectrum of intra-cavity metal-aperture VCSEL with 15nm and 30nm surface relief depth

Besides, for 30nm depth, even with larger contact metal CMin of +3µm and +4µm can realize the single mode operation as shown in Fig. 3-11. Single mode operation can be realized at 3mA to 7mA with larger than 30dB SMSR. When continue increasing the bias current to 8mA, although the multi-mode operation, still larger than 25dB SMSR can be obtained. However, the yield of single mode condition of +4µm contact metal is not good just around 20% because of the not enough transverse mode control. As illustrated in chap. 2.3.1, the distance between the oxidation aperture and contact metal should be less than 1μm to observe transverse coupled cavity effect. With the 30nm depth of surface relief which provide higher coupling strength, even with +3μm and some of +4μm of CMin which means the distance are 1.5μm and 2μm can realized transverse resonance.

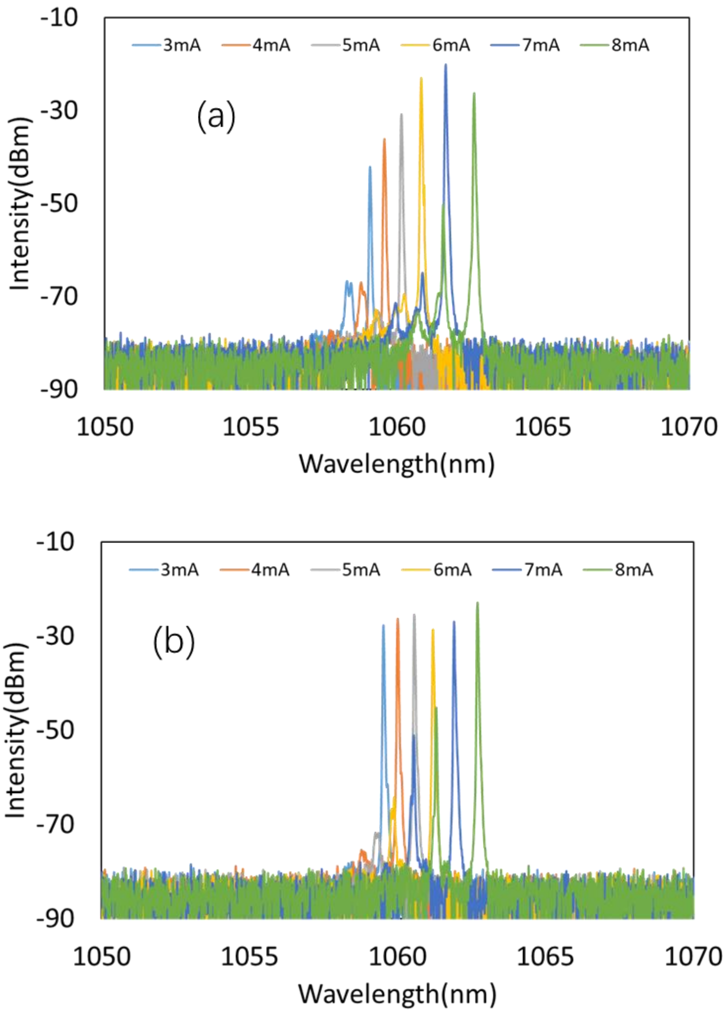

Fig. 3-11. Spectrum of intra-cavity metal-aperture VCSEL with (a)+3μm, (b)+4μm contact metal CMin

Thanks to the large coupling strength, the intra-cavity metal-aperture VCSEL with 6μm and 7μm oxidation aperture can also realized single mode operation as shown in Fig.

3-12. These are all with +1μm contact metal CMin. Stable single mode in the entire current range could be realized for 6μm oxidation aperture. Even for 7μm oxidation aperture, single mode can also be obtained at 8mA with larger than 25dB SMSR. Thanks to the large coupling strength, single mode operation can be realized even for 6μm and 7μm oxidation aperture VCSEL.

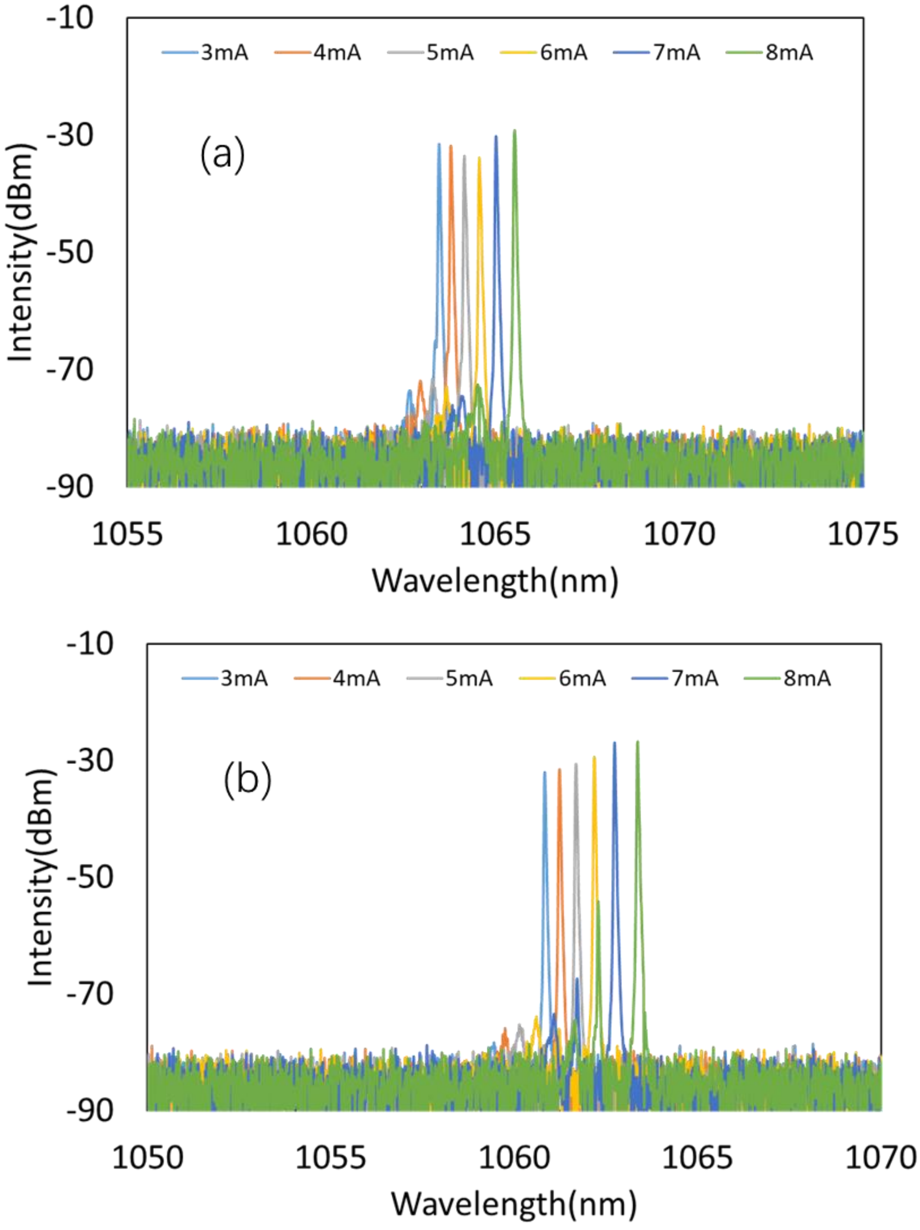

Fig. 3-12. Spectrum of intra-cavity metal-aperture VCSEL with (a)6μm, (b)7μm oxidation aperture

The near-field pattern (NFP), far-field pattern (FFP) are also measured as shown in Fig. 3-12. For 5μm oxidation aperture diameter devices, the mode field diameter is around 4.2μm which is corresponding to the oxidation aperture. The divergence angle is around 13° which is reasonable for the 5μm oxidation aperture diameter.

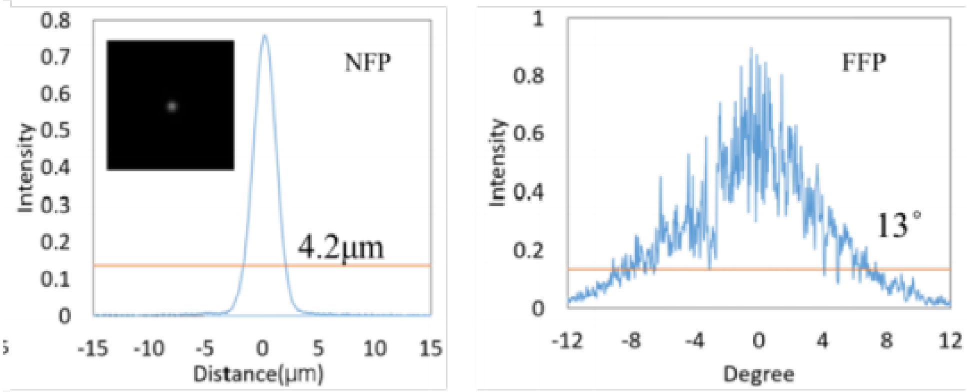

Fig. 3-12. (a) NFP and (b) FFP of intra-cavity metal-aperture VCSEL with 5μm oxidation aperture diameter

3.2.2 Small signal modulation response of intra-cavity metal-aperture VCSEL

The small signal measurement of the intra-cavity metal-aperture VCSEL will be demonstrated. The measurement setup was shown in Fig. 3-13. The metal aperture VCSEL is directly modulated by adding a RF signal with SHF BT45A bias tee. The output power is coupled into the multimode fiber towards the RXM42AF photo detector with a bandwidth of 42GHz. Then the digital signal is analyzed by the 40GHz vector network analyzer. The measurement setup is suitable for the high speed VCSEL.

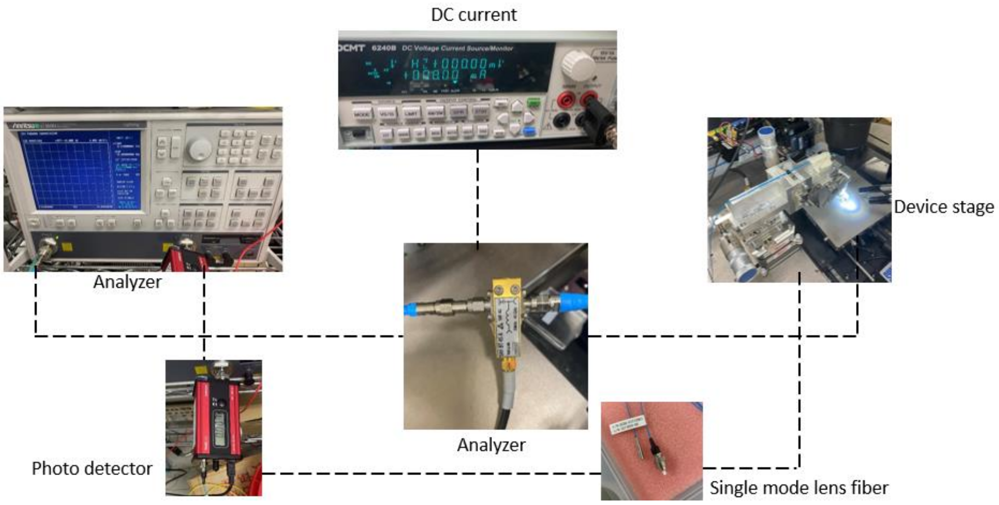

Fig. 3-13. Measurement setup of small signal measurement

The small signal modulation response of the intra-cavity metal-aperture VCSEL with 5μm oxidation aperture diameter and the four different contact metal diameter CMin at bias current of 6mA were shown in Fig. 3-15. For the devices with CMin: +2μm and +3μm are shown with higher modulation bandwidth. Which means the stronger coupled cavity effect is realized when the distance between the oxidation edge and the contact metal is around 1 to 1.5μm, which is consistence with the simulation results illustrated in Chap.2.

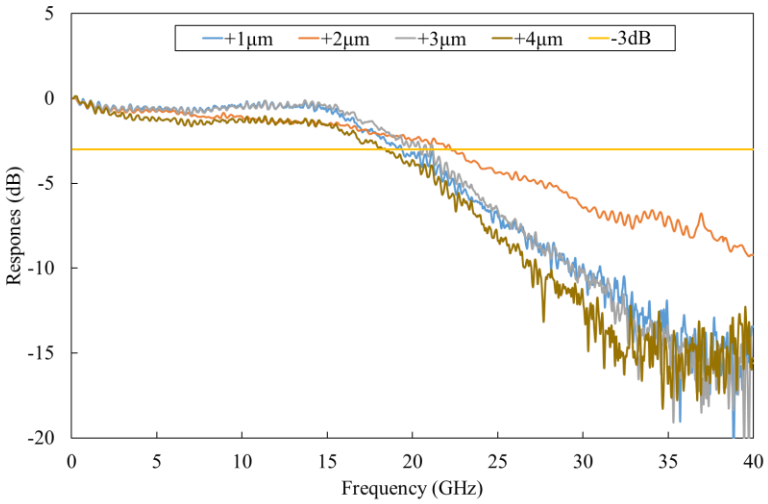

Fig. 3-15. The small signal response of intra-cavity metal-aperture VCSEL with 5μm

oxidation aperture diameter and the four different contact metal diameter CMin at bias current of 6mA

Figure 3-16 shows the small signal modulation response of the intra-cavity metal-aperture VCSEL with 5μm oxidation aperture diameter and +2μm CMin under different bias current which with highest modulation bandwidth. The highest bandwidth is around 23GHz at bias current of 7mA.

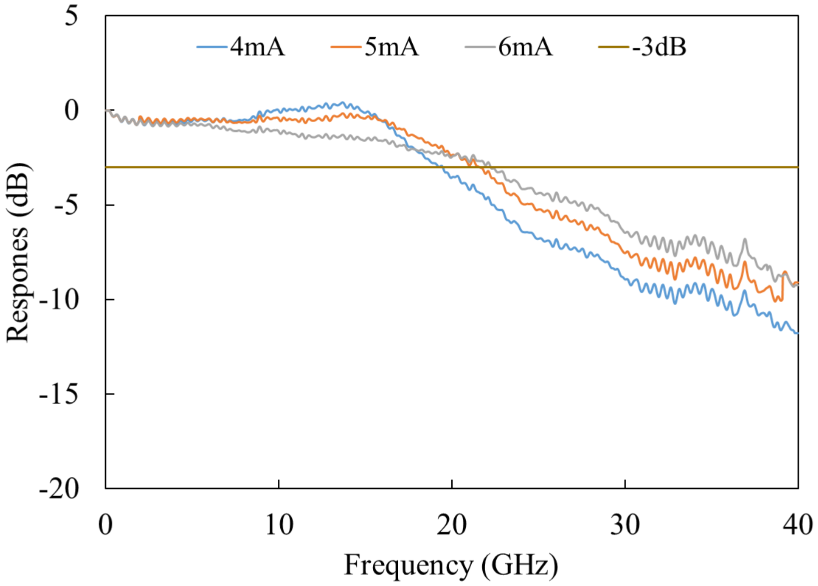

Fig. 3-16. The small signal response of intra-cavity metal-aperture VCSEL with 5μm oxidation aperture diameter and CMin of +2μm

3.3 Parasitic optimization of intra-cavity metal-aperture VCSEL

3.3.1 Theoretical model of parasitic optimization process

The parasitic optimization of intra-cavity metal-aperture VCSEL will be demonstrated. Figure 3-17 depicts the small signal model with the driving source, the extrinsic parasitic response, and the overall electrical modulation frequency response [1-3]. Rm denotes the combined resistance of sheet resistance, contact resistance, and mirror resistance. Ra represents the diode junction resistance. Cm includes mesa and junction capacitance. We aim to reduce the pad capacitance, which is represented by Cp. We use Rm, Cp, Cm, and Ra to represent the VCSEL. The extrinsic parasitic response can be computed using the transfer function in Eq. (1) [2], which is the injection ratio, Hext(ω):

$$H_{ext}(\omega) = \frac{i_a(\omega)}{v_s} \propto \frac{1}{\frac{(i\omega)^2}{\omega_0^2} + \frac{\omega}{\omega_0 \cdot Q} + 1} \tag{3-1}$$

where i_a is the current in the intrinsic diode, and v_s is the drive voltage.

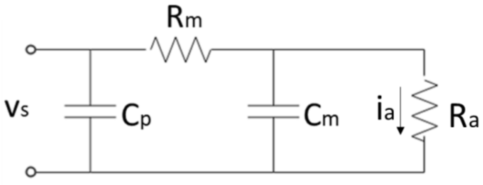

Fig. 3-17. Small signal model with the driving source

In my study, another polyimide layer will be added under the p-electrode pad as shown in Fig. 3-18. the extrinsic parasitic response with changes in pad capacitance Cp is shown in Fig. 3-19. The dielectric constant of the polyimide material used is 3.2. By increasing the height of the inserted polyimide layer from 0.1μm to 3μm when changing the pad capacitance from 2pF to 0.1pF, the extrinsic response can be significantly improved. However, further reduction of capacitance will not improve the response.

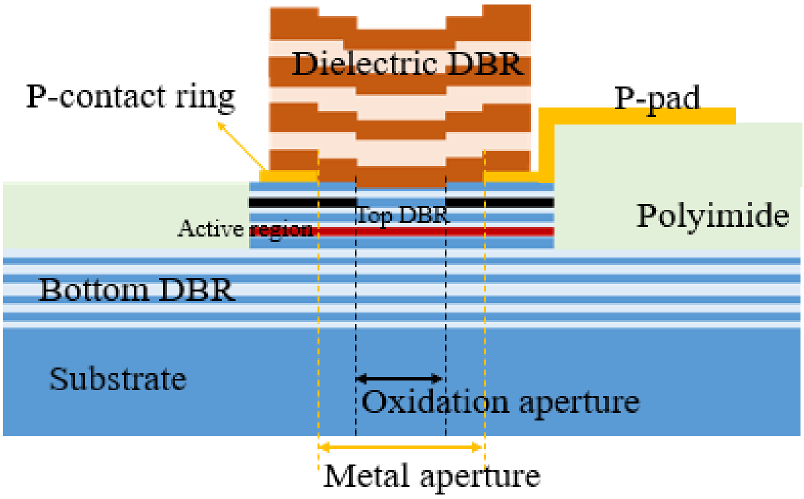

Fig. 3-18. Schematic structure of intra-cavity metal-aperture VCSEL with parasitic optimization process

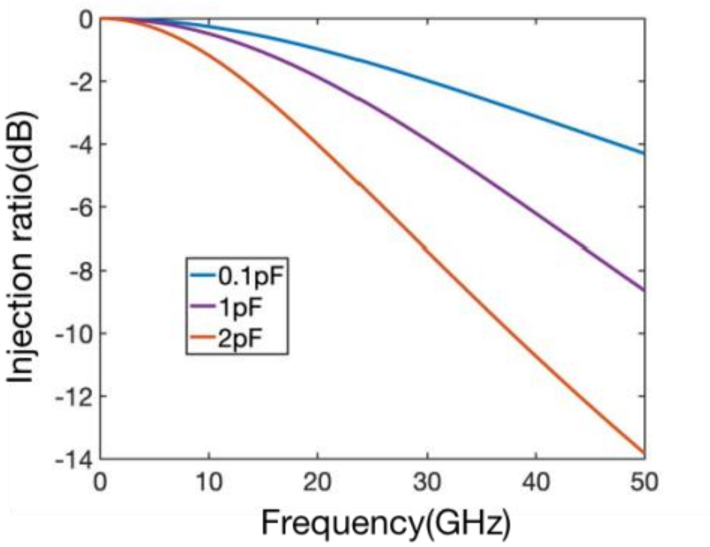

Fig. 3-19. Schematic structure of intra-cavity metal-aperture VCSEL with parasitic optimization process

3.3.2 Characteristics of intra-cavity metal-aperture VCSEL with parasitic optimization process

The photo of the fabricated intra-cavity metal-aperture VCSEL with parasitic optimization process is shown in Fig. 3-20.

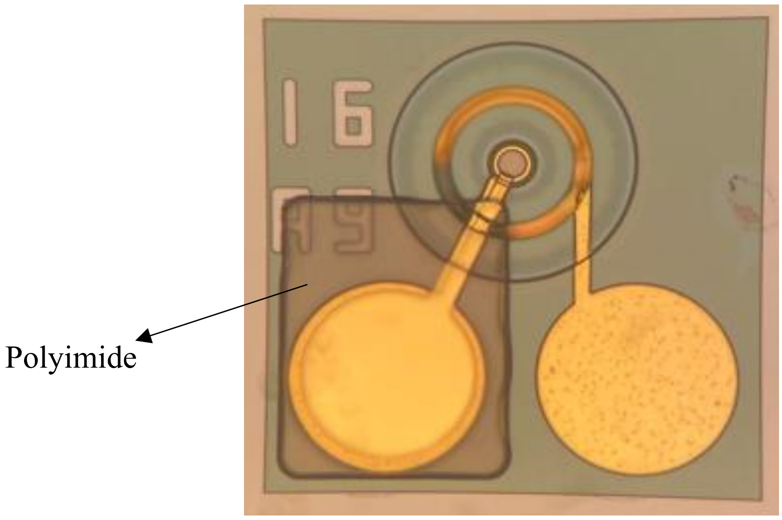

Fig. 3-20. Photo of intra-cavity metal-aperture VCSEL with parasitic optimization process

Figure 3-21 demonstrates the V/I and L/I characteristics and lasing spectrum of the low-parasitic metal aperture VCSEL under continuous wave excitation at room temperature. Figures 3-21(a) and 3-21(b) illustrate the results of the low-parasitic metal-aperture VCSEL with a 5μm oxidation aperture. At a bias current of 6mA, the single-mode power is 2.5mW, and the voltage is 2.9V. The slope efficiency is around 0.48W/A. Stable single-mode operation with SMSR over 50dB can be observed throughout the current range, as demonstrated in Fig. 3-21(b). Furthermore, we performed the low-parasitic metal-aperture VCSEL with a 6μm oxidation aperture and a 3.5μm width of p-contact metal ring, and the optical characteristics are presented in Fig. 3-21(c) and 3-21(d). Thanks to the transverse mode control due to the intra-cavity metal-aperture structure, single-mode operations over 40dB can still be observed. The high voltage of this wafer could be attributed to the high p-doping level and metallization process, which can be resolved by optimizing the fabrication process.

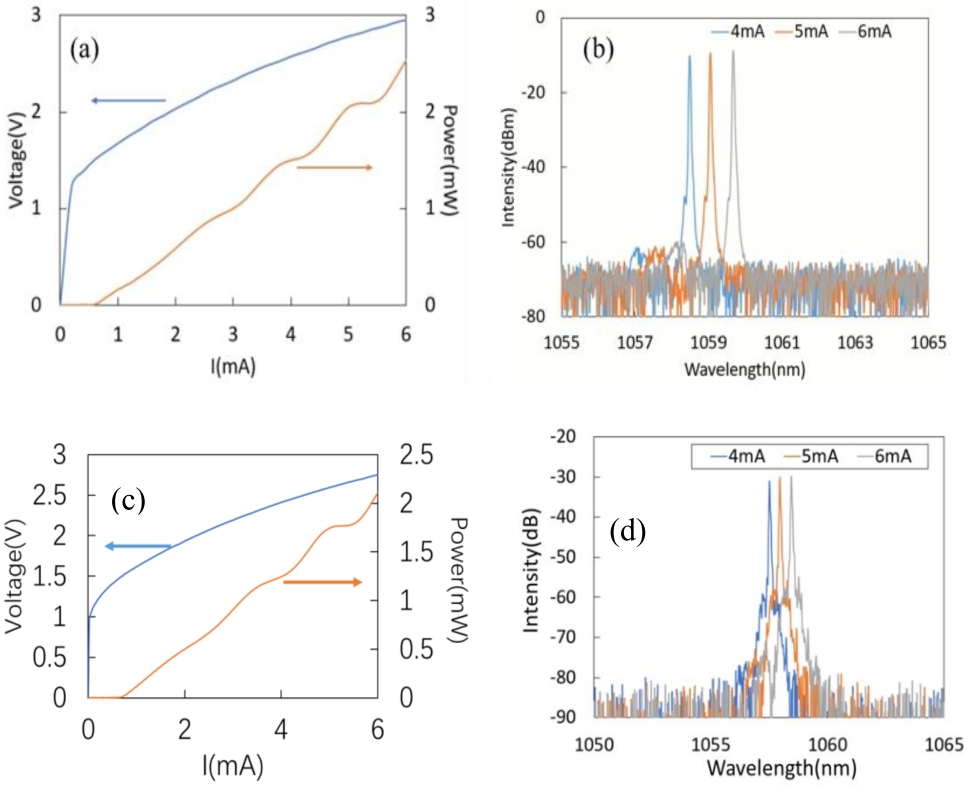

Fig. 3-21. (a) Measured V/I & L/I, and (b) lasing spectra of the metal-aperture VCSEL with 5μm oxidation aperture, (c) measured V/I & L/I, and (d) lasing spectra of the metal-aperture VCSEL with 6μm oxidation aperture.

Figure 3-22 presents the small signal modulation bandwidth of conventional VCSELs, metal-aperture VCSELs with and without a polyimide layer under back-to-back at a bias current of 6mA. All devices are fabricated from the same wafer and process. The metal-aperture process and inserted polyimide layer with 3.5μm height are the only differences. The small signal bandwidth of the conventional VCSEL is 18GHz. An increase in bandwidth is caused by the 4-pair 5nm-thick InGaAs quantum wells (QWs) compared to the 3-pair 7nm-thick QWs described in Ref. 29. The 3-dB modulation bandwidth for the metal-aperture VCSEL is increased to 24GHz with the same wafer structure due to the TCC effect from the metal aperture and surface relief process. Additionally, by inserting the polyimide layer under the p-pad to reduce parasitic capacitance, the bandwidth can be further improved to 29GHz. By improving the VI characteristics, higher modulation bandwidth can be expected.

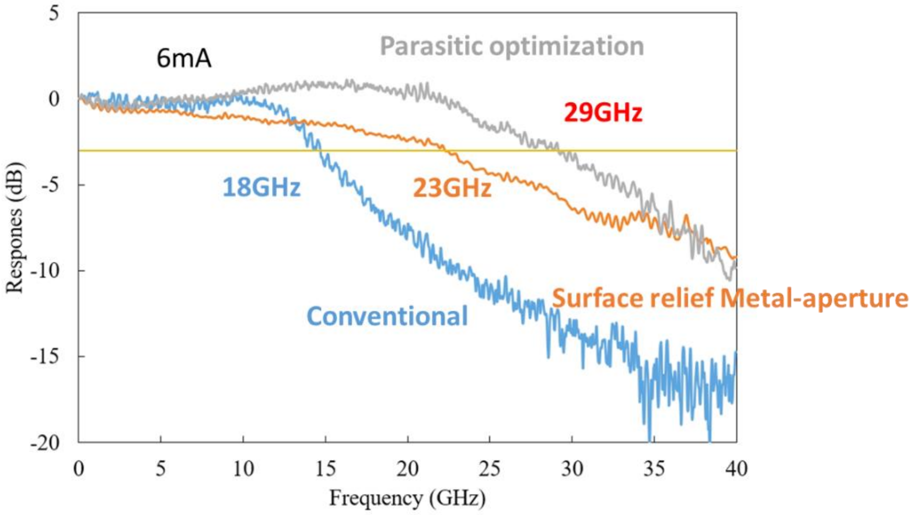

Fig. 3-22. Small signal modulation response of conventional VCSEL, metal aperture VCSEL with and without polyimide.

Figure 3-23 shows the small signal modulation characteristics at the bias current from 6mA to 8mA at room temperature. The record modulation bandwidth of over 31GHz at bias current of 8mA was obtained for 1060nm single-mode VCSELs.

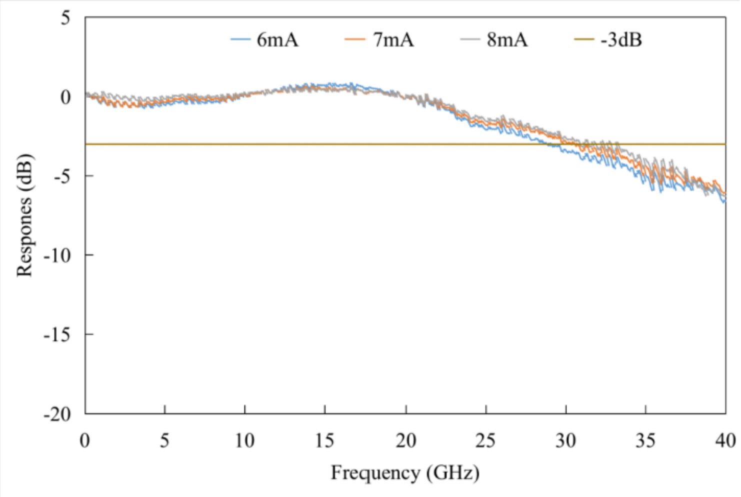

Fig. 3-23. Small signal modulation bandwidth under different bias current at room temperature

3.4 Uncooled operations of intra-cavity metal-aperture VCSEL

The uncooled operation of parasitic optimization intra-cavity metal-aperture VCSEL will be demonstrated. Figure 3-24 shows the L/I and V/I characteristics of the fabricated metal aperture VCSEL at 25°C, 55°C, and 85°C. The single-mode power at 7mA is 3.2mW at 25°C and 2.8mW at 55°C, respectively. A reduction in output power is as small as -0.6dB thanks to highly strained InGaAs quantum wells for 1060nm wavelengths band [11]. Stable single mode operations can be seen with SMSR over 30dB in the entire current range even for 5-6um oxide apertures thanks to the transverse mode control as shown in Fig. 3-25.

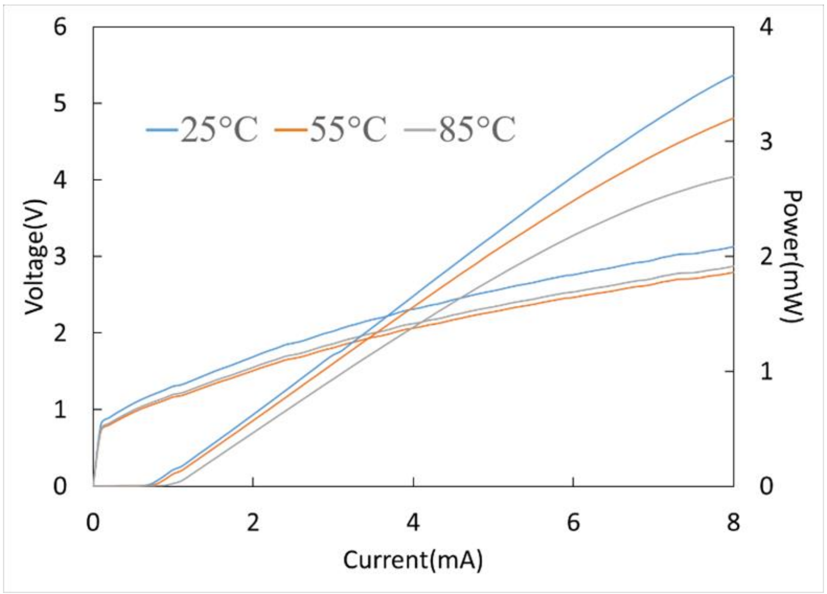

Fig. 3-24. L/I and V/I characteristics of intra-cavity metal-aperture VCSEL at 25°C, 55°C, and 85°C.

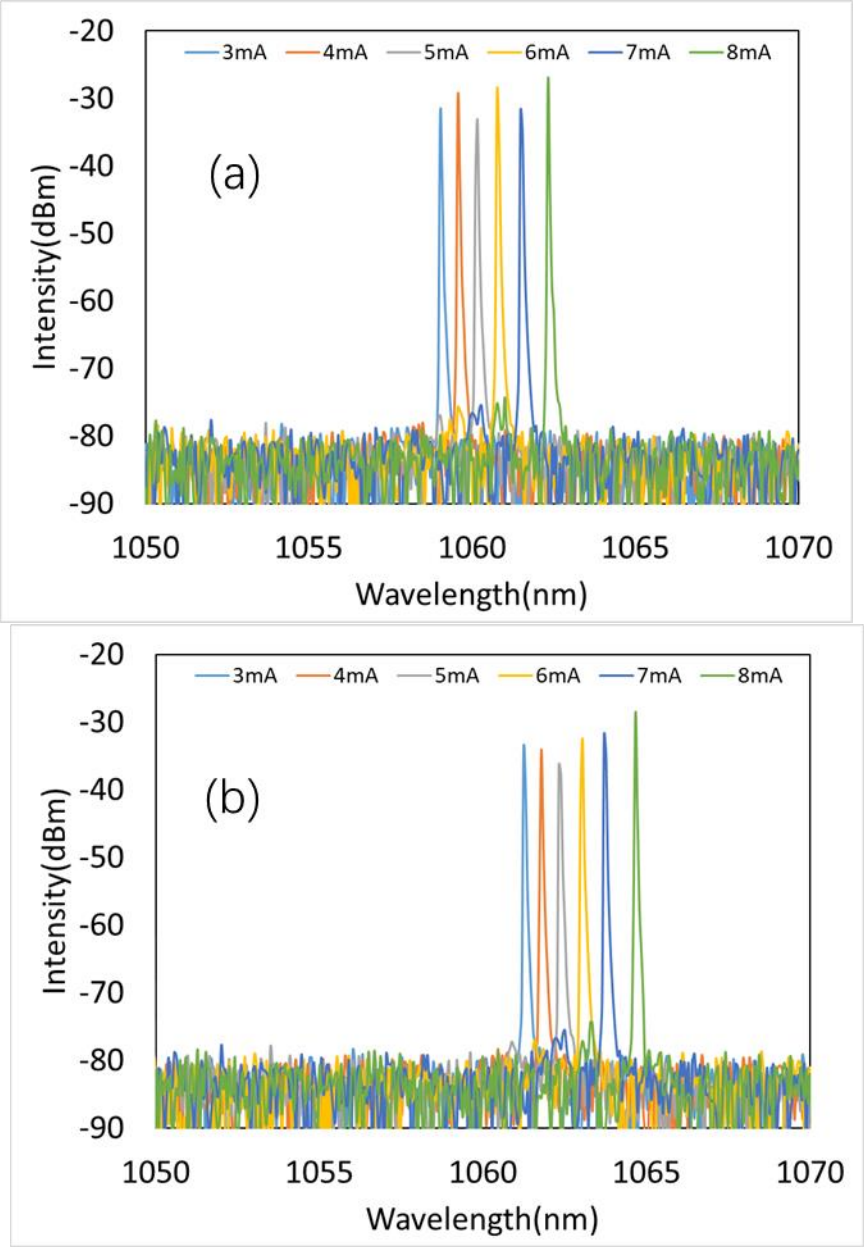
(a)
3mA
4mA
5mA
6mA
7mA
8mA
Intensity(dBm)
-20
-30
-40
-50
-60
-70
-80
-90
1050
1055
1060
1065
1070
Wavelength(nm)
(b)
3mA
4mA
5mA
6mA
7mA
8mA
Intensity(dBm)
-20
-30
-40
-50
-60
-70
-80
-90
1050
1055
1060
1065
1070
Wavelength(nm)

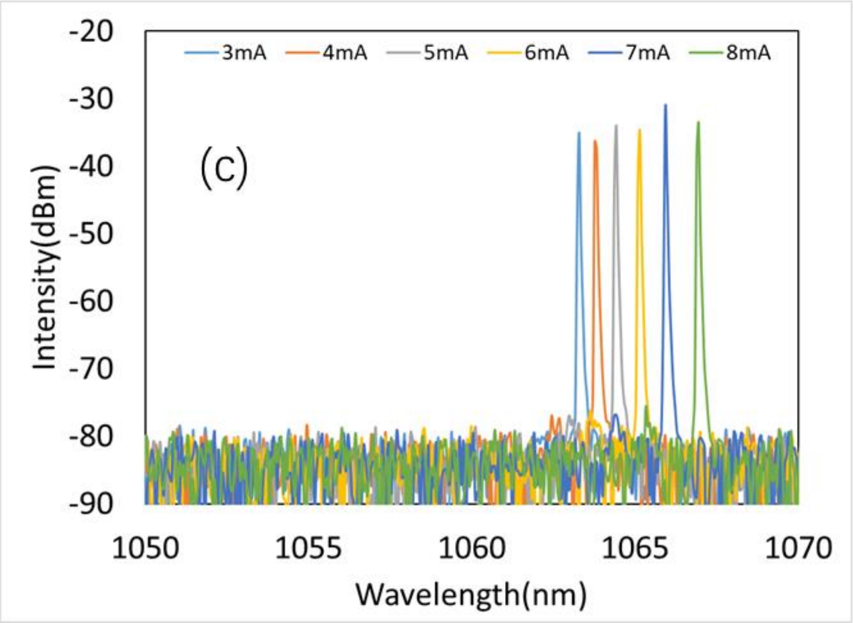

Fig. 3-25. Lasing spectra of intra-cavity metal-aperture VCSEL at (a) 25°C, (b) 55°C, and (c) 85°C.

The heat plate is added on the measurement stage for small signal test system as shown in Fig. 3-24.

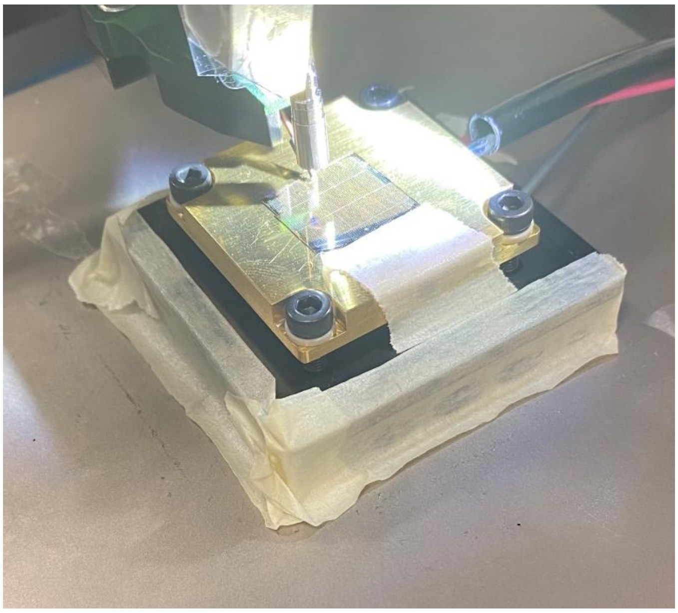

Fig. 3-26. Hot plate under device

Figure 3-27 shows the small signal modulation characteristics at the bias current from 6mA to 8mA at 55°C. As shown in Fig. 3-27, when the temperature increased to 55°C, the modulation bandwidth could reach at 27GHz. Just 4GHz reduced compared to which at the room temperature. When the temperature continues increase to 88°C, the small signal modulation bandwidth will reduce to around 20GHz. The parasitic optimization intra-cavity metal-aperture VCSEL shows good temperature stability at 55°C, however, the modulation bandwidth will be reduced larger than 10GHz at 88°C. Further modification of the structure to increase the temperature robustness should be concerned.

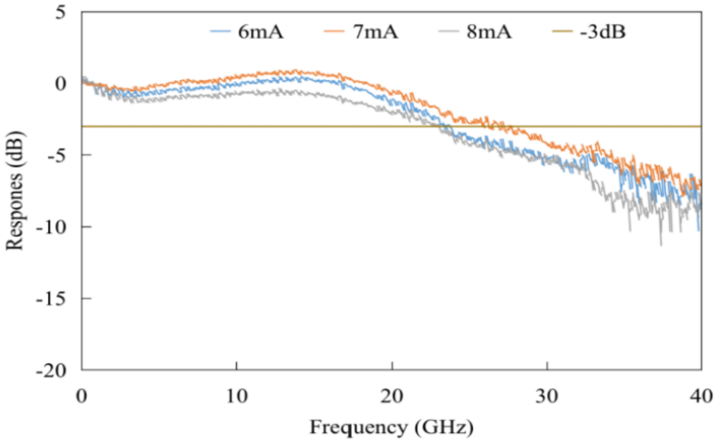

(a)

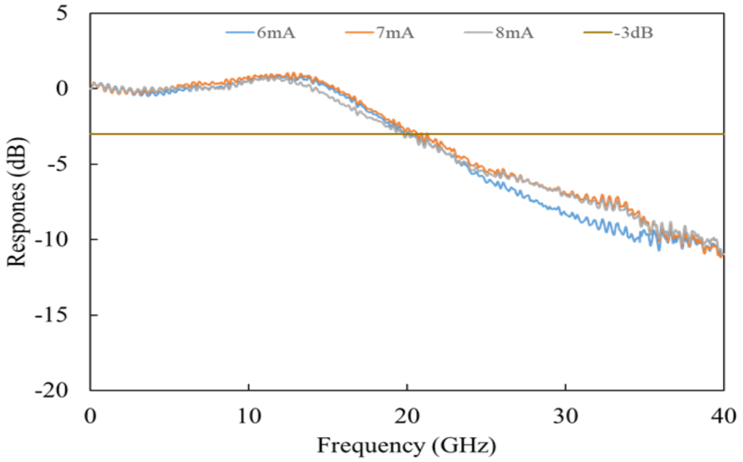

(b)

Fig. 3-27. Small signal modulation bandwidth under different bias current at (a) 55°C , and (b) 85°C.

Reference in Chapter 3

1) L. A. Coldren, S. W. Corzine, Diode lasers and photonic integrated circuits, 2012, p.195-207.

2) R. Michalzik, VCSEL fundamentals, 2013, p.235-241.

3) Hamad, Wissam, et al. "Impedance characteristics and chip-parasitics extraction of high-performance VCSELs." IEEE Journal of Quantum Electronics 56.1 (2019): 1-11.

Chapter 4

Intra-cavity metal-aperture VCSEL for single-mode fiber data transmission

In this chapter, high speed data transmission of intra-cavity metal-aperture VCSEL will be demonstrated. Small signal response and large signal measurement through single mode fiber with different fiber length will be illustrated.

4.1 Small signal modulation analysis through single-mode fiber transmission

The small signal modulation response through back-to-back, 2km, 5km, 10km single mode fiber transmission will be demonstrated. Figure 4-1 shows the small signal modulation of the low parasitic VCSEL with back-to-back, 2km, 5km, and 10km transmission through standard 1300nm-SMF (G652). The device used is the low parasitic intra-cavity metal-aperture VCSEL with 5μm-long oxidation diameter and +2μm CMin, which shows 29GHz modulation bandwidth at 6mA bias current under multi-mode fiber transmission as illustrated in Chap. 3.3.2. To analysis the km-long data transmission, the small signal modulation response is measured through different km-long SMF. The fiber are shown in Fig. 4-1. For the back-to-back transmission, the output power will be coupled in the single mode lens fiber with a 48% coupling efficiency. For longer transmission, the 2km, 5km, 10km single mode fiber can be connected with the single mode lens fiber. The fiber attenuation is approximately 1dB/km at 1060nm[1]. Through the km-long single mode fiber, the pulse compression takes place due to the fiber negative dispersion and frequency chirp[2-5]. The modulation bandwidth can be increased to 36GHz and 32GHz through 2km and 5km SMF, respectively, thanks to the frequency chirp and negative dispersion of the fiber. Figure 4-2 shows the transfer function of different fiber lengths, which is consistent with the calculated transfer function with a chirp parameter of 2.5. The result demonstrates the potential for 50Gbps (NRZ) and 100Gbps (PAM4) transmission up to 5km. For 10km transmission, the modulation bandwidth is reduced to around 25GHz, which also shows the possibility for over 40Gbps (NRZ) transmission.

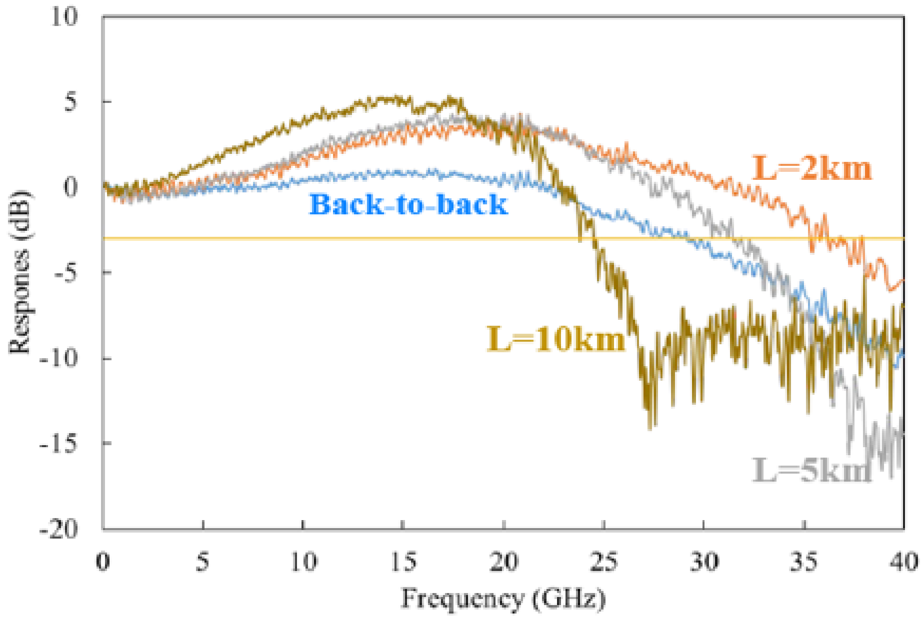

Fig. 4-1. Small signal modulation bandwidth through back-to-back, 2km, 5km, and 10km SMF

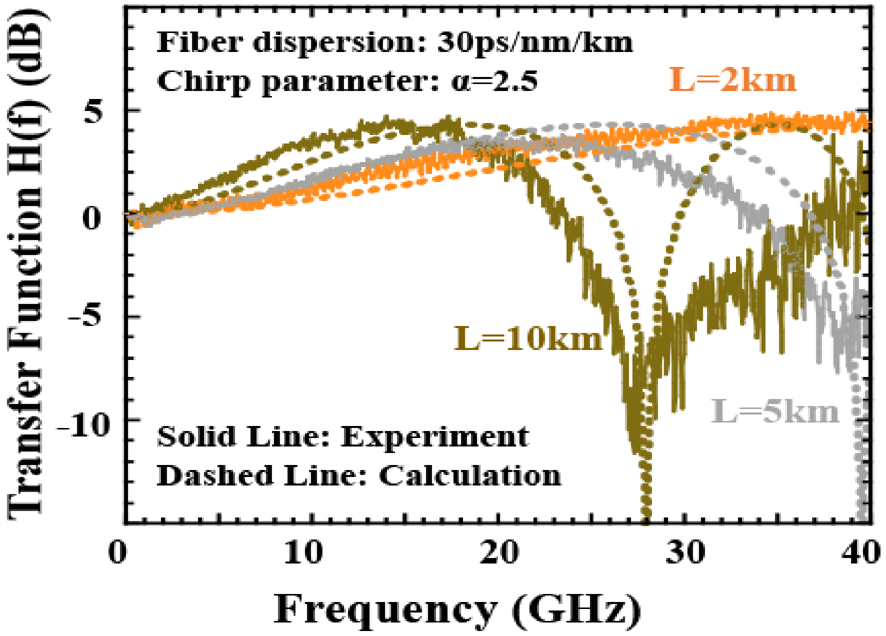

Fig. 4-2. Transfer function of SMF with different fiber length

4.2 Large signal modulation analysis through single-mode fiber transmission

The large signal measurement of the intra-cavity metal-aperture VCSEL will be demonstrated. The measurement setup was shown in Fig. 4-3. The arbitrary waveform generator (AWG) M8194A is responsible for generating the different types of electrical waveforms, such as NRZ and PAM4 signal. Then, the simulated signal is loaded through the bias tee with the amplifier which ensures that the generated electrical signals have sufficient power to drive the laser effectively on the tested device. The output power is coupled into the single mode lens fiber towards the DCA-M N1092A oscilloscope. Then, we use the software Keysight IQtools to generate the desired signal, the Keysight Oscilloscope to show the eye pattern waveform.

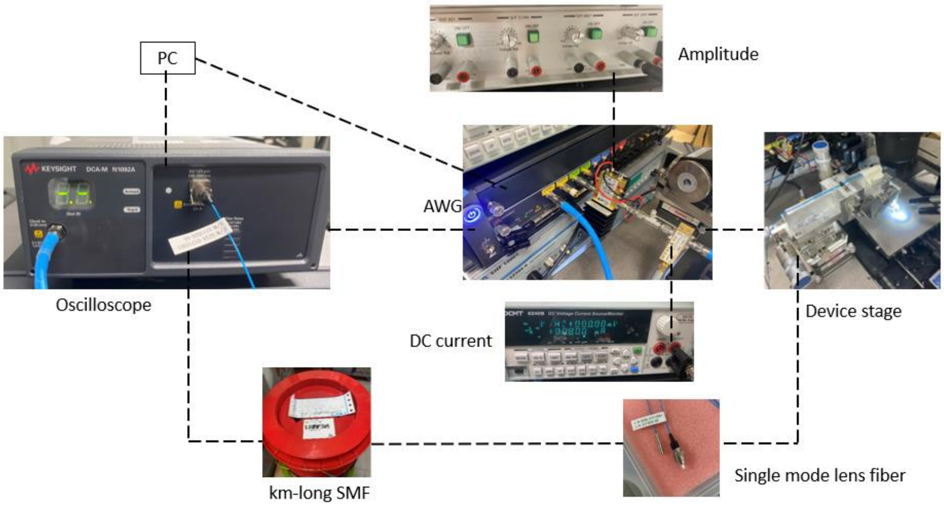

Fig. 4-3. Measurement setup of large signal measurement

High-speed large signal modulations at a 8mA bias current were measured. A test pattern of PRBS9 NRZ modulation signal was generated by the Keysight M8194A pattern generator. The results of NRZ eye pattern with different bit rates through back-to-back, 2km, 5km, and 10km SMF transmission without pre-equalization are shown in Figure 4-5. For back-to-back transmission, an output optical coupling in the lens fiber with a 48% coupling efficiency around 1.4mW can be achieved. A clear eye-opening up to 55-Gbps NRZ with an extinction ratio of 4dB can be observed under back-to-back transmission. The bit error rate (BER) could be less than 2E-14. Eye-closing can be seen at 60-Gbps due to the limit of the modulation bandwidth. Up to a clear eye-opening of 60-Gbps after 2-km SMF transmission without pre-equalization is shown in Figure 4-5(b) due to the high modulation bandwidth brought by the negative fiber dispersion. For longer transmission, the optical power through 5km and 10km SMF transmission is around 0.7mW and 0.3mW, respectively, since the fiber attenuation is approximately 1dB/km at 1060nm. Eye-opening up to 55-Gbps NRZ through 5km SMF transmission and 40-Gbps through 10km SMF transmission without pre-equalization can be observed, as shown in Figures 4-5(c) and 4-5(d).

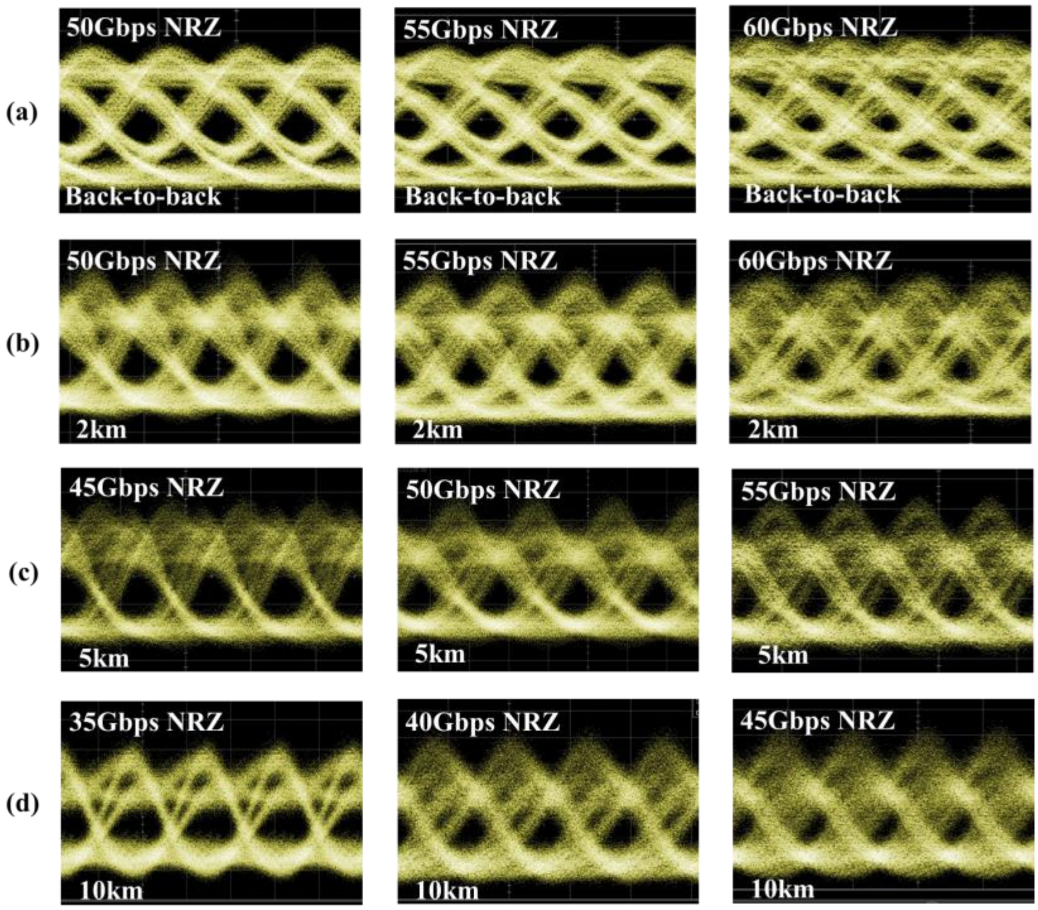

Fig. 4-5. Eye diagrams of large signal modulation NRZ without pre-equalization through (a) back-to-back, (b) 2km SMF, (c) 5km SMF, and (d) 10km SMF.

By utilizing 5-Taps pre-equalization, the outcome can be further enhanced with a 4dB extinction ratio, as demonstrated in Fig. 4-6. The results show clear eye-openings of up to 65-Gbps under back-to-back conditions, with a BER less than 1E-6, 75-Gbps through 2km SMF with a BER less than 3E-4, 70-Gbps through 5km SMF with a BER less than 3E-3, and 45-Gbps through 10km SMF with a BER less than 2E-4, demonstrating a bandwidth·distance product of 450 Gbps·km. The BERs are estimated from the waveform analysis software. The high modulation bandwidth and output power exceeding 3.2mW enable data transmission over a distance of 10km.

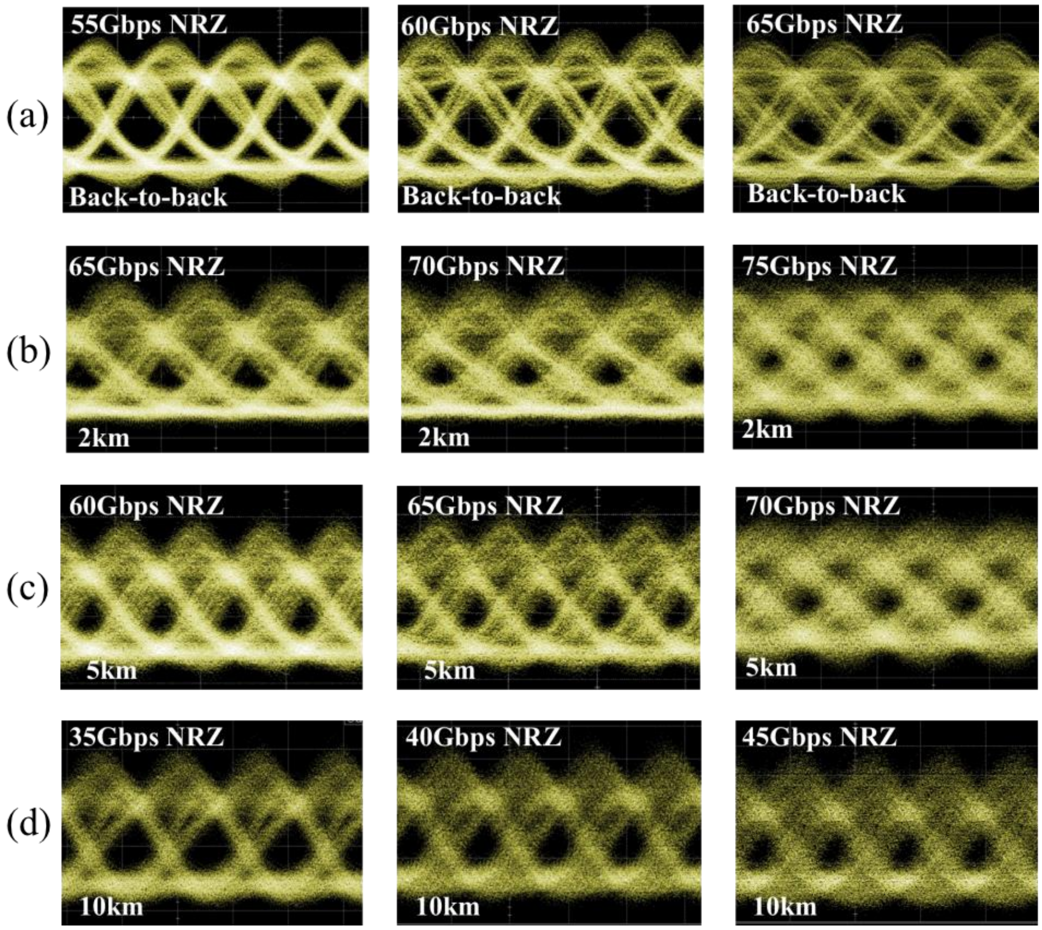

Fig. 4-6. Eye diagrams of NRZ modulation with pre-equalization through (a) back-to-back, (b) 2km SMF, (c) 5km SMF, and (d) 10km SMF.

Additionally, the eye diagrams of PAM4 modulation with 5-taps pre-equalization were measured and presented in Figure 9. The findings indicate eye-openings of up to 110-Gbps under back-to-back conditions with a 4.2dB transmitter and dispersion eye closure (TDECQ), 110-Gbps through 2km SMF with a 5.1dB TDECQ, 80-Gbps through 5km SMF with a 4.6dB TDECQ, and 40-Gbps through 10km SMF with a 3.5dB TDECQ transmission. TDECQ is called the Transmitter and Dispersion Eye Closure which is am important value to evalute the optical emission communication quality for PAM4. While the maximum TDECQ penalty for 50 GBd PAM4 Ethernet links is not defined yet, the maximum allowed for 26GBd PAM4 links is 4.5dB[]. The results show above are almost near the limit. TDECQ could be improved by increasing the modulation speed and linearity of the device. The device is capable of transmitting data at a speed of up to 110-Gbps, making it suitable for short-reach data centers and 6G network applications. The intra-cavity metal-aperture structure with low parasitics, stable single-mode, and high modulation bandwidth make mass production for high-speed data transmission possible. Additionally, modeling predicts that a lower chirp parameter could improve eye patterns, which could be achievable in coupled cavity VCSELs [28]. By increasing the output power, higher modulation speeds for 5km and 10km SMF transmission could be expected.

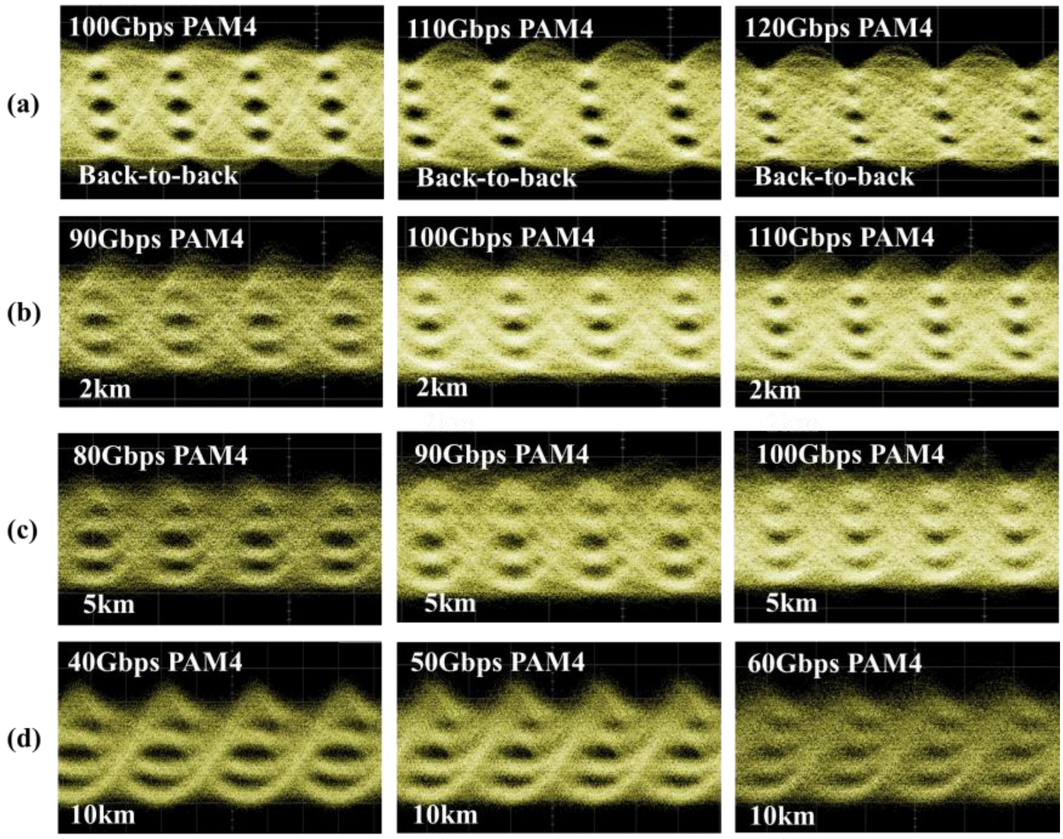

Fig. 4-7. Eye diagrams of PAM4 modulation with pre-equalization through (a) back-to-back, (b) 2km SMF, (c) 5km SMF, and 10km SMF.

Besides, the large signal measurement under uncooling operations will be demonstrated. The heat plate is put on the stage as same as small signal measurement setup.

The eye diagrams of NRZ modulation with 5-taps pre-equalization at 55°C were measured and presented in Figure 4-9. When the temperature increased to 55°C, the power is a little reduced from 3.2mW to 2.8mW. Also, the modulation bandwidth is around 4GHz reduced as described in Chap. 3.4. The findings indicate eye-openings of up to 55-Gbps under back-to-back conditions with a BER less than 8E-7, 70-Gbps through 2km SMF with a BER less than 9E-4, 50-Gbps through 5km SMF with a BER less than 5E-4, and 40-Gbps through 10km SMF with a BER less than 8E-3 transmission. Although the temperature increased, still up to 70Gbps NRZ transmission can be realized. Up to 50Gbps for 5km long and 40Gbps for 10km long transmission are achieved. In addition, the eye diagrams of PAM4 modulation with 5-taps pre-equalization through 2km SMF transmission at 55°C are shown in Figure. 4-10. We observe eye-openings of up to 90-Gbps with a 4.7dB TDECQ and 100Gbps with a 5.6dB TDECQ for 2km SMF transmission. Uncooling operations at 55°C of intra-cavity metal-aperture single mode VCSELs were obtained up to 100Gbps which shows a good temperature robustness up to 55°C. Further extensions on link lengths and higher bit rates could be expected by chirp reduction and bandwidth enhancement in transverse coupled cavity VCSELs. A large-scale 2D array of transverse coupled cavity VCSELs could offer a potential for increasing aggregate bandwidths of over Tbps.

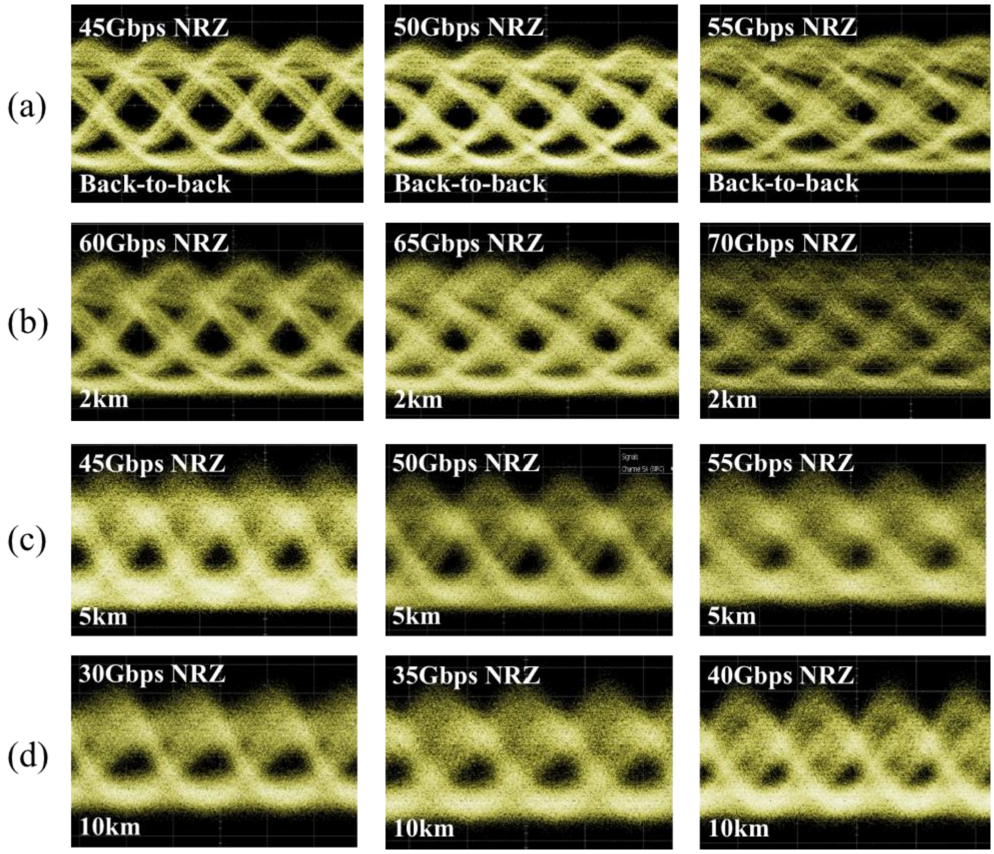

Fig. 4-9. Eye diagrams of NRZ modulation with pre-equalization through (a) back-to-back, (b) 2km SMF, (c) 5km SMF, and (d) 10km SMF at 55°C.

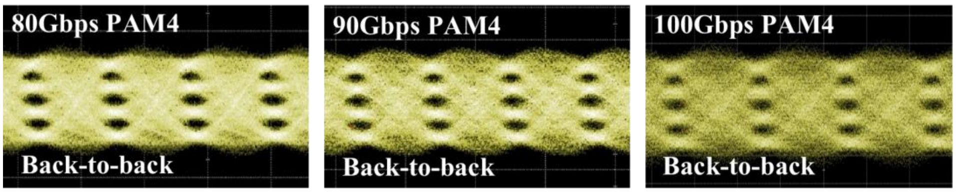

Fig. 4-10. Eye diagrams of PAM4 modulation with pre-equalization through back-to-back at 55°C.

Reference in Chapter 4

1) Liu, Anjin, et al. "Vertical-cavity surface-emitting lasers for data communication and sensing." Photonics Research 7.2 (2019): 121-136.

2) Wright, J. V., and B. P. Nelson. "Pulse compression in optical fibres." Electronics Letters 12.13 (1977): 361-363.

3) Koyama, F. U. M. I. O., and Y. A. S. U. H. A. R. U. Suematsu. "Analysis of dynamic spectral width of dynamic-single-mode (DSM) lasers and related transmission bandwidth of single-mode fibers." IEEE journal of quantum electronics 21.4 (1985): 292-297.

4) Koyama, F, et al. "Data transmission over single-mode fiber by using 1.2-μm uncooled GaInAs-GaAs laser for Gb/s local area network." IEEE Photonics Technology Letters 12.2 (2000): 125-127.

5) Kondo, T., et al. "Isolator-free 10 Gbit/s singlemode fibre data transmission using 1.1 μm GaInAs/GaAs vertical cavity surface emitting laser." Electronics letters 40.1 (2004): 1.

Chapter 5

Design of surface grating VCSELs

In this chapter, principle of surface grating loaded VCSEL will be demonstrated. The coupled mode theory of surface grating VCSEL will be shown. The simulation of grating loaded VCSEL with short cavity and long cavity length will also be discussed.

5.1 Principle of surface grating loaded VCSEL

Grating structures have been widely used in such as distributed feedback (DFB) lasers [1-3]. The grating structure provides narrow passband filtering and single-mode operations of semiconductor lasers. The wave propagation in periodic waveguide structures has been studied [4-7]. Former studies provided the theoretical calculation of coupling modes including the calculation of refractive index perturbation [8] and coupling coefficient (κ) [9-10]. These analyses discuss the lasing condition and mode selectivity for DFB lasers with different coupling constants (κ L) by applying the coupling mode theory [9-16] and discuss the influence of phase shift and AR-coated facet on the lasing condition [17-24].

To figure out the lasing condition of the grating loaded VCSEL structure and the limitation of the device length, we should model the grating loaded VCSEL structure. In contrast to DFB lasers with guided modes, the light travels as “Zigzag” format in VCSELs which leads to slow-wave. As a result, the group index and phase index largely changed [25]. In our preliminary work [28], the reflection spectrum and threshold conditions of grating loaded VCSELs were presented.

Figure 5-1 shows the schematic structure of the grating loaded VCSEL, where the grating is formed by shallow etching on the surface of a conventional 850nm GaAs VCSEL. The layer structure is the same as conventional 850 nm VCSELs with three quantum wells (QWs) sandwiched by top and bottom distributed Bragg reflectors (DBRs). The reflectivity of both ends are ρ_l and ρ_r, respectively. If an oxide aperture is formed at an end, the reflectivity $\rho_{l,r}$ is nearly unity, and also a tapered shape could offer $\rho_{l,r} \sim 0$ at an end [31]. Since light travels laterally in the VCSEL structure as a slow wave, the output light radiates through the surface. The surface grating makes a small perturbation of the phase refractive index which provides the feedback mechanism as same as DFB lasers. We have seen the unique features in the surface grating VCSEL. The phase refractive index of a slow light is below unity as shown later. Thus, this unique feature makes the fabrication of surface gratings easy. A grating depth of ~ 30 nm on the surface of the mesa is large enough to select a single mode since the field of a slow wave penetrates to the surface. The coupling strength κ between forward and backward waves is large enough for mm long cavities. Fabrication steps are the same as those for conventional 850 nm VCSELs except making the surface grating. Also, we confirmed that the 2nd-order grating can be made by a standard stepper lithography, which could be suitable for mass-production.

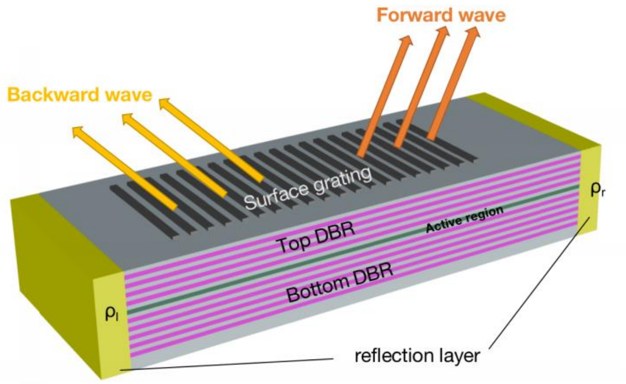

Fig. 5-1 Schematic structure of grating loaded VCSEL.

We assume that a grating-loaded VCSEL has 19 pairs of top DBR, 30 pairs of bottom DBR, and the grating depth is 20 nm. We chose 19 pairs of a top DBR for high-power operations, which was experimentally demonstrated in ref. 26. Proper pairs of top-DBR are needed to enable low thresholds and high slope efficiencies as optimized for conventional VCSELs. This figure is one example of grating loaded VCSELs, the pairs of top-DBR could be changed to meet the demands of different applications. The refractive index of the high index and low index regions in grating are simulated by the film mode matching method [29]. The refractive index of this periodic structure can be solved by Fourier expansion in the following equations [13,15,24],

$$\mathrm{n(z)} = n_0 + (\Delta \mathrm{n})\cos(2\pi \mathrm{m z}/\Lambda) \tag{1}$$

$$n_0 \approx \mathrm{n_1}(1 - \mathrm{D}) + \mathrm{n_2 D} \tag{2}$$

$$\Delta \mathrm{n} \approx \frac{2(\mathrm{n_1} - \mathrm{n_2})}{\pi \mathrm{m}} \sin(\pi \mathrm{D m}) \tag{3}$$

where n_0 is the average phase index, D is the duty cycle of the surface grating, Λ is the grating pitch, m is the grating order, n_1 is the refractive index of the high index region, n_2 is the refractive index of the low index region according to rectangular grating grooves. Figure 5-2 shows the calculated average phase index n_0 of this grating-loaded structure. It is noted that the phase index of slow light is below unity thanks to a large waveguide dispersion, thus the 1st-order grating pitch is as large as 500 nm at 830 nm of wavelength, which makes the grating fabrication easier.

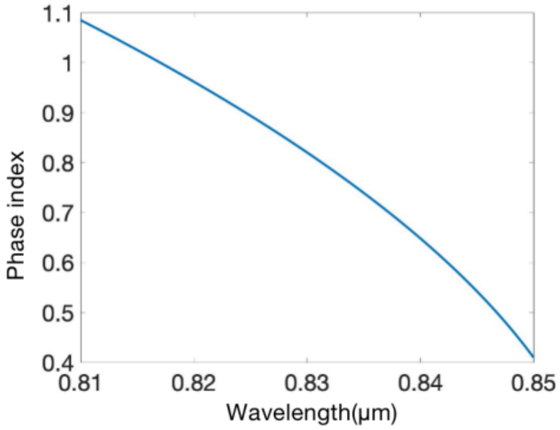

Fig. 5-2 Calculated phase index of grating loaded VCSEL.

A key parameter of the coupled-mode theory is the coupling coefficient κ which can be calculated by the following equation [24],

$$\kappa = \frac{\beta}{2}\frac{\Delta n}{n} + i\frac{\Delta\alpha}{2} \approx \frac{2(n_1 - n_2)\sin(\pi D m)}{m\lambda} \tag{4}$$

where β is the propagation constant, $\Delta\alpha$ is the gain perturbation, λ is the lasing wavelength. In the present simulation, the imaginary part is assumed much smaller than the real part which could be ignored.

By changing the grating depth from 10 to 40 nm, and the pairs of top-DBR from 19 to 5 pairs, the grating order from 1st order to 8th order, the coupling coefficient κ can be changed from 1 cm^{-1} to more than thousand cm^{-1} as shown in Fig. 5-3. Higher grating depth, fewer pairs of top DBR, and lower grating order lead to larger coupling coefficients. In brief, a wide range of coupling coefficients can be controlled in various device lengths from 10μm to cm long cavities for low threshold and high-power operations, respectively.

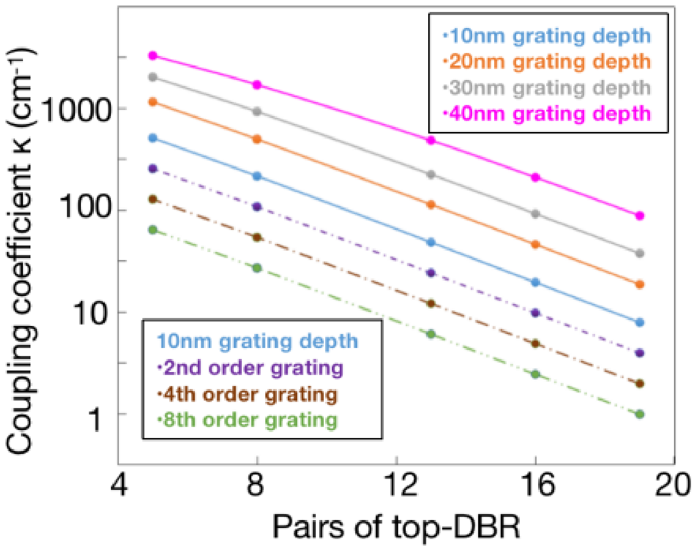

Fig. 5-3 Calculated coupling coefficient of grating loaded VCSEL.

Figure 5-4 shows the comparison of the calculated reflection spectra from gratings for the slow-wave and conventional guided-wave with a coupling coefficient κ of 20 $cm^{-1}$and center wavelength of 830 nm. The grating pitch of a slow wave is assumed as 500nm for the 1st-order grating. While both of the coupling coefficients are 20cm^{-1}, the 3dB reflection bandwidth of the slow-wave is 0.06nm which is much smaller than the guided-wave as shown in Fig. 5-4. The group index is as large as 17. A shallow surface grating provides strong optical feedback and a narrow stopband. These unique features come from slowing light.

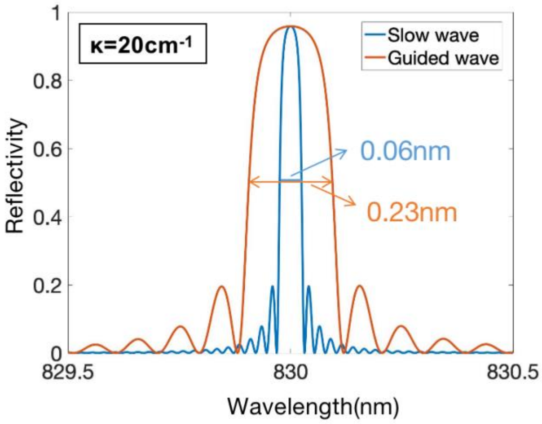

Fig. 5-4 Reflection spectra of grating for slow wave and guided wave.

5.2 Simulation of grating loaded VCSEL

With the small perturbation of the phase refractive index, the coupled mode theory could be applied for lasing condition analysis. The electric field is written as [2]:

$$E(z) = B_{+}(z)e^{i\beta_0 z} + B_{-}(z)e^{-i\beta_0 z} \tag{5}$$

where B+(z) and B-(z) are the forward and backward slow waves. Considering the boundary conditions, B-(L)=0 and B+(0)=0. The reflection coefficient is [2]

$$r = \frac{B_{-}(0)}{B_{+}(0)} = \frac{-\kappa^{*}\sinh(\gamma L)}{\Delta\beta\sinh(\gamma L)+i\gamma\cosh(\gamma L)} \tag{6}$$

$$\gamma^2 = \kappa^2 - \Delta\beta^2 \tag{7}$$

where κ is the coupling constant, Δβ is the deviation of propagation constant from the Bragg wave vector. To analysis the lasing condition, the threshold gain and radiation loss need to be considered. And γ changes to follow [2]:

$$\gamma^2 = (\alpha - i\Delta\beta)^2 + \kappa^2 \tag{8}$$

where α is the total net gain.

The threshold gain and lasing mode could be calculated by solving the following lasing condition [2]

$$\frac{\gamma}{i\kappa}\left(\frac{\gamma}{i\kappa} - e^{-i\frac{\pi}{2}}\sinh(\gamma L)\right) + \left(e^{-i\pi} - 1\right)\sinh^2\left(\frac{\gamma L}{2}\right) = 0 \qquad (8)$$

According to the coupled mode theory, κL could determine the total net gain: αL and bragg wave deviation: δL, where $\alpha = \frac{f\Gamma_s g - f\alpha_i}{2}$, g is material gain and $\Gamma_s g$ is modal gain. Then, typical simulation for mm-long grating loaded VCSEL and hundred micrometers long grating loaded half-cavity VCSEL will be discussed.

5.2.1 Grating loaded VCSEL with long-cavity length

With shallow grating depth and large grating pitch, the slow-wave structure provides a wide range of coupling coefficients which enables various cavity lengths from 10μm to 1cm. The lasing condition of a surface grating loaded VCSEL is simulated by solving the coupled-mode equations [4]. For high-power operations, the device length needs to be increased to mm long which requires a low coupling coefficient. To simulate the grating loaded VCSEL with asymmetric reflections at each end, we simplified the reflectivity of the right end of the grating loaded VCSEL as 0. To reduce the coupling coefficient, we choose the grating loaded VCSEL structure with a grating depth of 10nm and 19 pairs of a top-DBR. We show the threshold gain for each resonant mode with different reflectivities at other end in Fig. 5-5(a), its different reflection phase in Fig. 5-5(b), and different coupling coefficients in Fig. 5-5(c). Figure 5-5(a) shows the lasing condition under three different reflectivity: 1, 0.95, 0.75, and 0.5 with a fixed $\kappa L=1$. When a reflectivity is down to 0.5, the normalized threshold gain difference $\Delta\alpha L$ is as small as 0.09 which makes it difficult to get single-mode operations. Through the figure, by increasing the reflectivity, we could get lower threshold gain with higher gain difference which means more stable single-mode operations. When the reflectivity is equal to $1e^{i\pi/2}$, the normalized threshold gain difference is 0.674 and hence the threshold gain difference can be over 6 cm^{-1} for a 1 mm long device, thus the single-mode operation can be expected. Please note that the lateral propagation of slow light could be cut-off in an oxidized region. Thus, the reflectivity could be nearly 100% at an oxidized facet, which is based on the principle of the oxide confinement structure of VCSELs. Figure 5-5(b) shows the lasing condition under different reflection phases: 0, π/2, π, and 3π/2 with a fixed κL=1. The figure shows that when the phase is equal to 0, π/2, and π, the normalized threshold gain difference ΔαL is over 0.5, and hence single-mode operation with a reasonable large gain difference can be expected. Therefore, there is a phase tolerance of more than 50% which is feasible for the fabrication process.

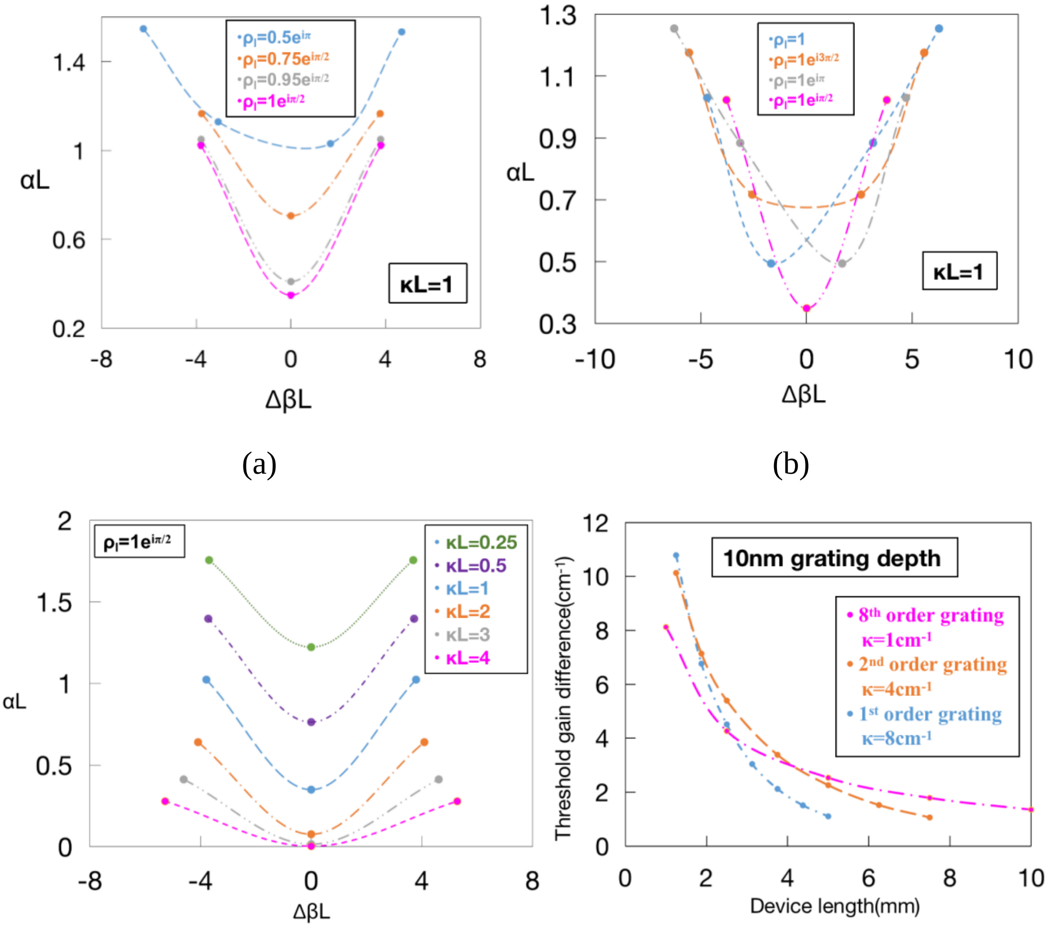

(a) (b)

(c) (d)

Figure 5-5 (a), (b) and (c) show the lasing condition with different reflectivity, reflection phase, and coupling constant, respectively; (d) shows the threshold gain difference versus device length with different κ.

Figure 5-5(c) shows the lasing condition under different coupling coefficients κL with an end reflectivity of $1e^{i\pi/2}$. When the coupling coefficient changes from 0.25 to 4, the threshold gain is reduced while the threshold gain difference decreases. The figure shows that when κL=1, the threshold gain difference gets the largest value around 0.67 which means we could get the highest threshold gain difference when κL=1. When the device length is determined, we could find an optimal coupling coefficient κ that could provide the highest threshold gain difference as shown in Fig. 5-5(d). We assumed that the reflectivity is $1e^{i\pi/2}$, the grating depth is 10nm, and 19 pairs top-DBR. By changing the grating order from 1st order, 2nd order to 8th order, corresponding to the grating pitch raging from 500nm, 1μm to 4μm, the coupling coefficient can be controlled from 8cm^{-1} to 1cm^{-1}. Even for a 10mm long device, κ=1cm^{-1} provides a higher threshold gain difference of 1.4cm^{-1}. For a 2.5mm long device, κ=4cm^{-1} could get a higher threshold gain difference of 5.4cm^{-1}. For a few mm-long grating-loaded VCSEL, we could expect single-mode operation, which is supported by experiments [26,27]. Also, we calculated the power ratio between the forward wave and backward wave, which provides two directional beams. A unidirectional output characteristic can be seen with a power ratio of over 10, which could be due to the asymmetry in the reflections as the right and left edges. Most of output power can be radiated in the direction of the non-reflective end side, which is also supported by experiments [27].

5.2.2 Grating loaded half-cavity VCSEL with short-cavity length

Short cavity devices enabling low-power consumptions could be useful for datacom applications. To realize a short-cavity grating loaded VCSEL structure, the coupling coefficient needs to be increased. As shown in Fig. 6, different from the long cavity grating loaded structure, the pairs of top-DBR need to be reduced. We chose 5 pairs of a semiconductor DBR and 6 pairs of a dielectric DBR in the modeling. As shown in Fig. 5-6, a 5-pair semiconductor top-DBR offers a large grating coupling coefficient of over 1,000 cm-1, enabling us to reduce a cavity length of below 20mm. By adding 6 pairs of dielectric DBR, the overall reflectivity could be around 99%, which is typical in low threshold VCSELs. According to the calculation of the coupling coefficient shown in Fig. 5-3, the coupling coefficient could be increased to more than 1000cm^{-1} with different grating depths. For short cavity devices, both end facets are formed by wet-selective oxidation process. We assumed that the reflectivity of the left end facet is unity, and the right side is changed from 0.5, 0.7 to 0.95 for a lasing wavelength of 830nm.

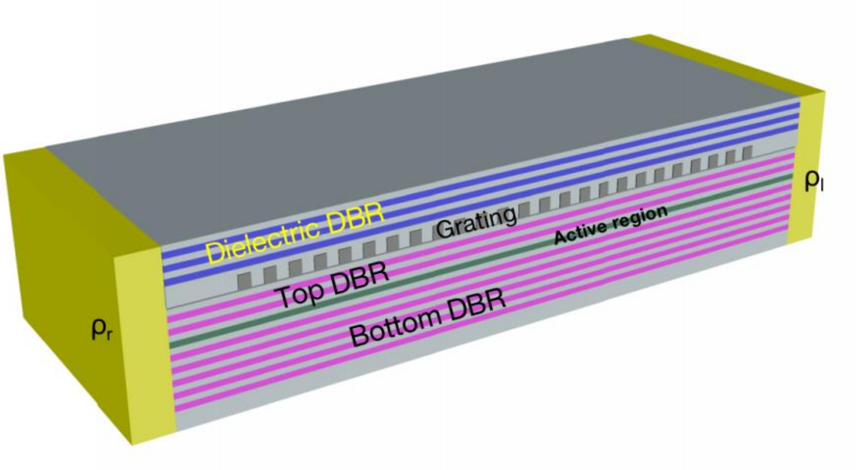

Figure 5-6 Short-cavity grating loaded VCSEL structure.

The lasing condition is calculated as a function of the reflectivity at the end as shown in Fig. 5-7(a) and on the coupling coefficient in Fig. 5-7(b). Figure 5-7(a) shows that the threshold gain αL and the gain difference are dependent on the reflectivity of the right end facet at a fixed κL of 1. With increasing the reflectivity, the threshold gain and threshold gain difference are reduced.

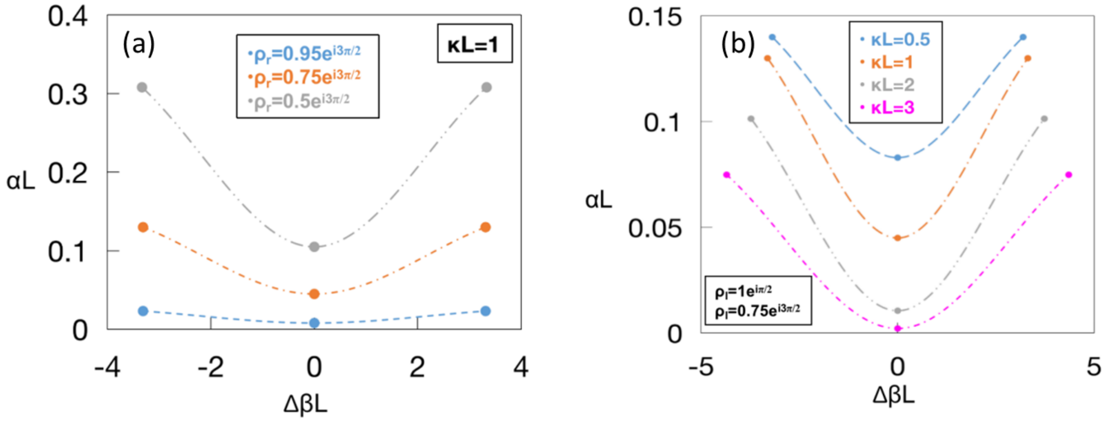

Figure 5-7 (a) and (b) show the lasing condition with different reflectivity and coupling constant, respectively.

With 5 pairs top-DBR, 6 pairs dielectric DBR, and 500nm grating pitch where the lasing wavelength is 830nm, the coupling coefficient κ of short cavity grating loaded VCSEL structure could be more than 1000cm^{-1}. Figure 5-8 shows the threshold gain as a function of a device length with different grating depths. Through the figure, larger grating depth leads to a larger coupling coefficient, enabling a short cavity length of 10μm. When the grating depth is 30nm, the coupling coefficient could reach 2035cm^{-1} for a device length of 10μm with the threshold gain of 82cm^{-1}. Correspondingly, the threshold current density could be around 1.8kA/cm^{2} for 10μm long devices.

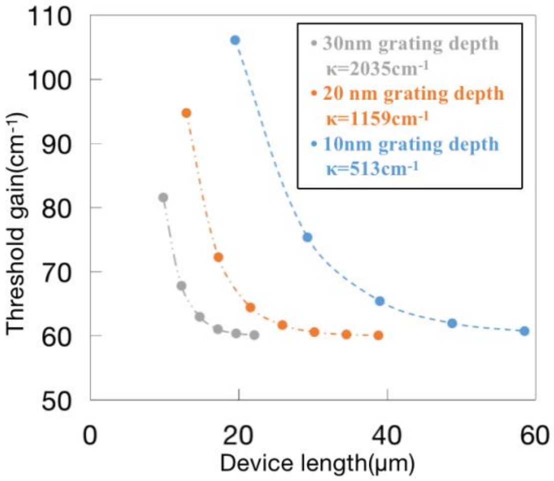

Figure 5-8 Threshold gain versus device length.

Reference in Chapter 5

1) Iga, Kenichi. "Forty years of vertical-cavity surface-emitting laser: Invention and innovation." Japanese Journal of Applied Physics 57.8S2 (2018): 08PA01.

2) Fessant, T. "Gaussian-like tapered grating quarter wave-shifted DFB semiconductor lasers for high-power single-mode operation." Applied Physics B: Lasers & Optics 67.6 (1998).

3) Fessant, Thierry. "Enhanced dynamics of QWS-DFB lasers by longitudinal variation of their coupling coefficient." IEEE Photonics Technology Letters 9.8 (1997): 1075-1077.

4) Kogelnik, H., and C. Vo Shank. "Coupled ‐ wave theory of distributed feedback lasers." Journal of applied physics 43.5 (1972): 2327-2335.

5) Yariv, Amnon, and Michiharu Nakamura. "Periodic structures for integrated optics." IEEE journal of quantum electronics 13.4 (1977): 233-253.

6) Streifer, William, D. Scifres, and R. Burnham. "Analysis of grating-coupled radiation in GaAs: GaAlAs lasers and waveguides-I." IEEE Journal of Quantum Electronics 12.7 (1976): 422-428.

7) Wang, Shyh. "Principles of distributed feedback and distributed Bragg-reflector lasers." IEEE Journal of Quantum Electronics 10.4 (1974): 413-427.

8) Handa, K., S. T. Peng, and T. Tamir. "Improved perturbation analysis of dielectric gratings." Applied physics 5.4 (1975): 325-328.

9) Brosson, P., et al. "Simple determination of coupling coefficient in DFB waveguide structures." Electronics Letters 24.16 (1988): 990-991.

10) Streifer, William, D. Scifres, and R. Burnham. "Coupling coefficients for distributed feedback single-and double-heterostructure diode lasers." IEEE Journal of quantum electronics 11.11 (1975): 867-873.

11) Jia, Xin-Hong, et al. "Detailed modulation response analyses on enhanced single-mode QWS-DFB lasers with distributed coupling coefficient." Optics communications 277.1 (2007): 166-173.

12) Wang, Shyh. "Principles of distributed feedback and distributed Bragg-reflector lasers." IEEE Journal of Quantum Electronics 10.4 (1974): 413-427..

13) Kogelnik, H., and C. Vo Shank. "Coupled ‐ wave theory of distributed feedback lasers." Journal of applied physics 43.5 (1972): 2327-2335..

14) Yariv, Amnon. "Coupled-mode theory for guided-wave optics." IEEE Journal of Quantum Electronics 9.9 (1973): 919-933..

15) Streifer, William, D. Scifres, and Robert Burnham. "Coupled wave analysis of DFB and DBR lasers." IEEE Journal of Quantum Electronics 13.4 (1977): 134-141..

16) Wang, Shyh. "Design considerations of the DBR injection laser and the waveguiding structure for integrated optics." IEEE Journal of Quantum Electronics 13.4 (1977): 176-186.

17) Fessant, Thierry, and Yann Boucher. "Additional modal selectivity induced by a localized defect in quarter-wave-shifted DFB lasers." IEEE journal of quantum electronics 34.4 (1998): 602-608..

18) Utaka, K., et al. "Analysis of quarter-wave-shifted DFB laser." Electronics Letters 8.20 (1984): 326-327..

19) Favre, Francois. "Theoretical analysis of external optical feedback on DFB semiconductor lasers." IEEE Journal of Quantum Electronics 23.1 (1987): 81-88.

20) Haus, Hermann A., and Y. Lai. "Theory of cascaded quarter wave shifted distributed feedback resonators." IEEE journal of Quantum Electronics 28.1 (1992): 205-213..

21) Zengerle, Remigius, and Ottokar Leminger. "Phase-shifted Bragg-grating filters with improved transmission characteristics." Journal of Lightwave Technology 13.12 (1995): 2354-2358.

22) Lowery, Arthur J., Adrian Keating, and Casper N. Murtonen. "Modeling the static and dynamic behavior of quarter-wave-shifted DFB lasers." IEEE journal of quantum electronics 28.9 (1992): 1874-1883.

23) Anderson, D. B., R. R. August, and J. E. Coker. "Distributed-feedback double-heterostructure GaAs injection laser with fundamental grating." Applied Optics 13.12 (1974): 2742-2744.

24) Streifer, William, D. Scifres, and R. Burnham. "Coupling coefficients for distributed feedback single-and double-heterostructure diode lasers." IEEE Journal of quantum electronics 11.11 (1975): 867-873.

25) Hassan, Ahmed MA, et al. "High power and high beam quality surface grating VCSEL." CLEO: Science and Innovations. Optica Publishing Group, 2021.

26) A. Hassan, X. Gu, et al. "High-power operations of single-mode surface grating long oxide aperture VCSELs." Appl. Phys. Lett. 119, 191103 (2021)

27) Hassan, Ahmed MA, et al. "High power surface grating slow-light VCSEL." Applied Physics Express 14.9 (2021): 092006.

28) C. Ge and F. Koyama, "Modeling of surface grating-loaded VCSEL with slowing light." MOC2021, PO-45 (2021).

29) Sudbo, A. Sv. "Film mode matching: a versatile numerical method for vector mode field calculations in dielectric waveguides." Pure and Applied Optics: Journal of the European Optical Society Part A 2.3 (1993): 211.

Chapter 6

Fabrication and characterization of surface grating VCSEL

In this chapter, the details about fabrication process and experimental characteristics of surface grating loaded coupled cavity VCSEL will be discussed. The simulation of 2nd order grating loaded VCSEL with vertical emission will also be shown.

6.1 Surface grating loaded coupled cavity VCSEL

6.1.1 Principle of surface grating loaded coupled cavity VCSEL

The schematic of surface grating loaded coupled cavity VCSEL is shown in Fig. 6-1. It was also fabricated based on the half-cavity VCSEL wafer. The half-cavity VCSEL wafer used was almost same as the metal-aperture VCSEL's epi-wafer, which includes 6 pairs of top-DBRs, 3 pairs of 7-nm/10-nm $In_{0.25}Ga_{0.75}As/GaAs$ QWs, and 33-pair of bottom DBRs. Since we only have this half-cavity VCSEL epi-wafer stocked, and this is the first time realize the surface grating coupled cavity VCSEL, this epi-wafer could be enough for present experiment. Since the half-cavity VCSEL with insufficient top reflectivity, a Ta2O5/SiO2 top dielectric DBRs will also be deposited on the surface to achieve sufficient top reflectivity which is around 99%. Since for surface grating VCSEL, the slow wave will be applied, so the lasing wavelength will be around 1040nm, and the deflection angle could be around 50 degree. Therefore, we considered change the thickness of dielectric DBR at 1040nm band to as shown in Fig. 6-2. After dry-etching for first order surface grating, a ring-shaped p-contact metal is evaporated on the surface of the half-cavity VCSEL with a different diameter and line width. Subsequently, the standard VCSEL fabrication process will be followed. The top view of the mesa is shown in Fig. 2-1(b).

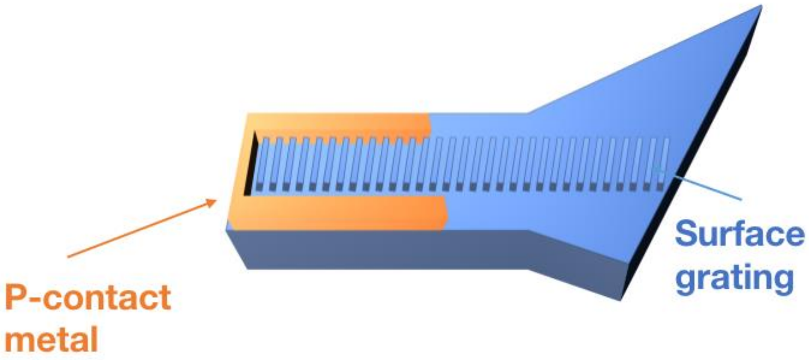

Fig. 6-1. The schematic mesa of surface grating VCSEL

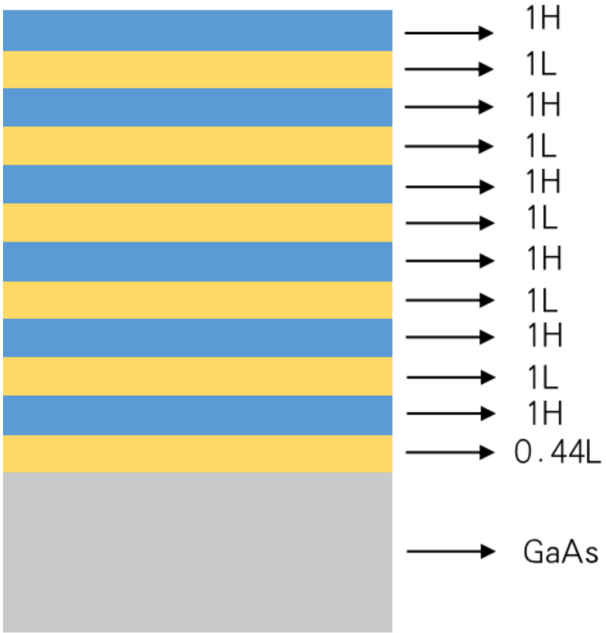

Fig. 6-2. The structure of dielectric DBR

Since the phase index of slow light is below unity as demonstrated in Chap. 5.1, the first order grating pitch is as large as 560 nm at 1040 nm. In my study, I chose 580nm, 600nm, 630nm of grating pitch. Also, we include metal-aperture for surface grating VCSEL to realize coupled cavity effect. Also to further increase the PPR effect, the 20nm longer passive coupled cavity is included. Also, to realize single mode operation, the reflection of one side should be reduced, and it realized by applying a taper-shape cavity as shown in the Fig. 6-3. Also, the length of the taper cavity changed from 30nm to 60nm. The length of oxidation aperture changed from 20µm, 40µm, 60µm, 80µm, 100µm, to 120µm. The width of oxidation aperture changed from 3µm, 4µm, to 5µm, with 6µm oxidation length. Thus, the mesa length was changed from 32µm to 132µm, and the mesa width changed from 15µm to 17µm. Besides, the CMin and CMout represent the inner and outer diameter of p-contact metal ring, respectively. The distance between the oxidation aperture and CMin is changed from 2µm to 3µm. The linewidth of contact metal will be 3µm. The parameters are shown in Table. 6-1. With the surface grating, the lasing wavelength can be selected and realize single mode emission. Also, the coupled cavity could provide PPR effect to increase the modulation bandwidth.

Table 6-1. Parameter of grating pitch, oxidation width, and cavity length

	Value		
Grating pitch	650nm	686nm	714nm
Oxidation width	3µm	4µm	5µm
Cavity length	20µm, 40µm, 60µm, 80µm, 100µm, 150µm, 200µm,		

6.1.2 Fabrication process of surface grating loaded coupled cavity VCSEL

The fabrication process of surface grating coupled cavity VCSEL is compatible with intra-cavity metal-apertrue VCSEL. Since the wafer have been prepared by FujiFilm, the other process will go through dry etching for surface grating, SiO_2 sputtering, p-contact metal evaporation, ICP for mesa, oxidation, wet etching to reveal n-contact layer, polyimide passivation, n-contact metal evaporation, p-electrode and n-electrode evaporation, and dielectric DBR deposition. These processes were completed in our laboratory, except ICP and dielectric DBR deposition. The photoresist will be finished, then the samples were send to the company to accomplish the ICP etching and dielectric DBR deposition. The critical fabrication processes will be discussed as follow:

① The 3-inch half-cavity VCSEL wafer shown in Fig. 6-3 was finished by the foundry outside the university. Since the process machine in our laboratory only permits the sample of 2mm×2mm, the sample used will be cut from the 3-inched wafer with 2mm×2mm.

② Surface grating: The surface grating is formed by outside foundry, since the grating pitch is around 500nm, which is too small to process in our laboratory. The schematic structure and photo of surface grating are shown in Fig. 6-3 and Fig. 6-4, respectivily. After the sample send back with surface grating, the SiO_2 should be sputtered to protect the grating and surface.

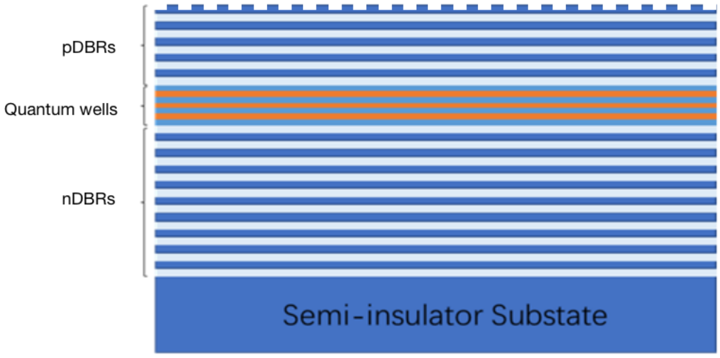

Fig. 6-3. The schematic structure of surface grating

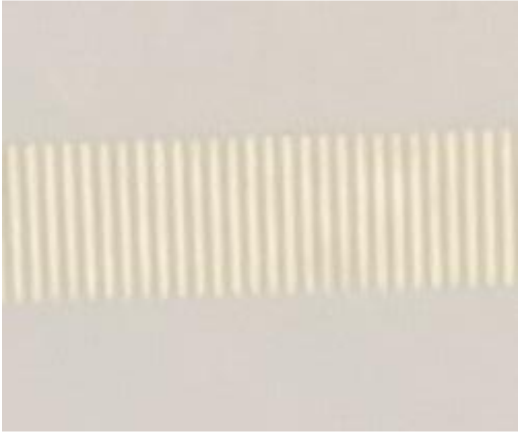

Fig. 6-4. The photo of surface grating

③ P-contact metal: The surface grating coupled cavity VCSEL also include the metal aperture process which same as the intra-cavity metal-aperture VCSEL. Since the oxidation length is 6µm, and there is 1µm left between the mesa edge and CMout, the distance between oxidation aperture and CMin could be 1µm and 2µm with 4µm and 3µm linewidth, respectively. The details about the process is demonstrated in Chap. 3.1.2. Figure 6-5 shows the photo of the surface after surface grating and contact metal process.

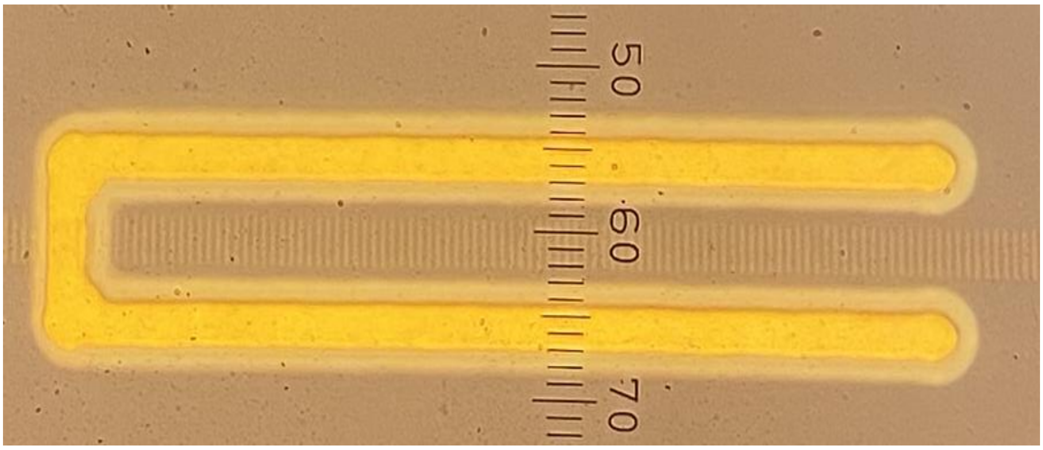

Fig. 6-5. The photo of metal aperture and surface grating

④ ICP for mesa: Then, the ICP for mesa formed. The ICP process is also finished by foundry. The photo in Fig. 6-6 shows the mesa with a taper side. According to the simulation, stable single mode operation realized when one side reflectivity is small enough. The taper side could effectively reduce the reflectivity of the right-side wall which could contribute to mode control. The following process will same as the intra-cavity metal-aperture VCSEL.

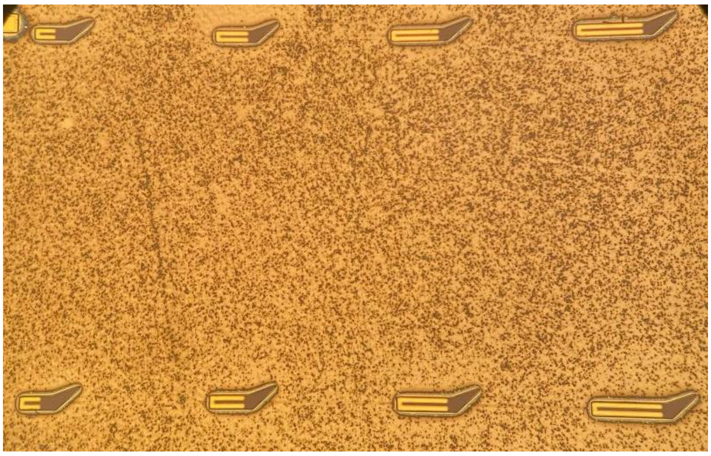

Fig. 6-6. The photo of the mesa with taper side

⑤ Oxidation: After ICP etching for mesa, oxidation process was followed. Since the oxidation layer is AlAs, the oxidation temperature is 340°C, the photo of oxidation aperture is shown in Fig. 6-7. The oxidation length can be detected by the microscope during the oxidation process. After 61min oxidation, the color of oxided region will change to white.

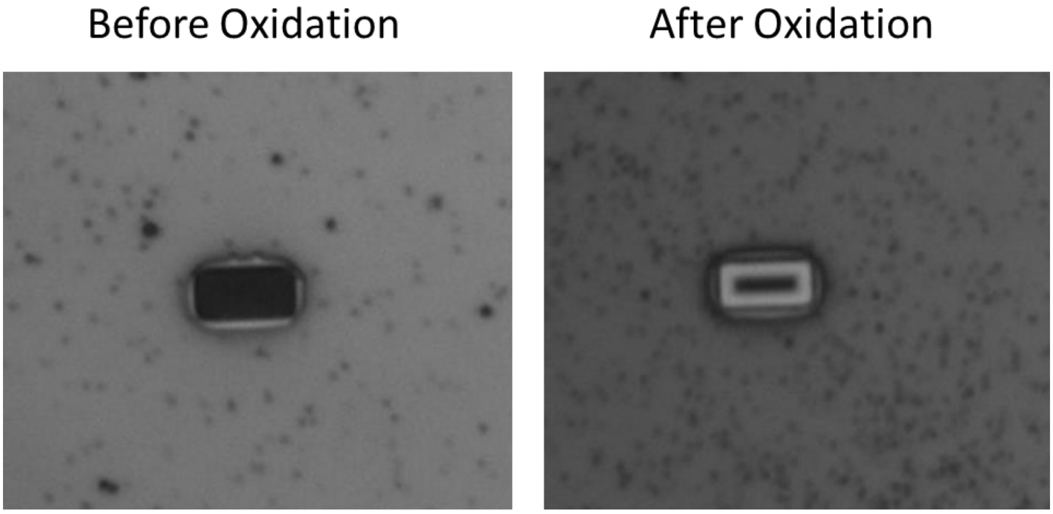

Before Oxidation

After Oxidation

Fig. 6-7. The photo of the oxidation mesa

⑥ N-contact etching and polyimide passivation: Following the oxidation process, it is necessary to expose the n-contact layer through wet etching. The etching depth should be approximately 4μm, and the bottom-DBR should be completely etched to minimize resistance. The wet etching window can be observed in Figure 6-8. Subsequently, polyimide passivation is carried out. To ensure complete removal of the polyimide in the n-contact window, the polyimide window must be larger than the contact etching window. Furthermore, the polyimide passivation process should occur after the wet etching. The passivation height, once cured, is approximately 3μm. The clear delineation of the polyimide window indicates the thorough elimination of polyimide in the n-contact window. Moreover, the side walls of both the n-contact and polyimide windows exhibit a U-shaped configuration. By applying polyimide around the outer region of the n-contact window, the side walls can be made flatter, facilitating the connection of the n-contact metal. Additionally, to ensure complete removal of the polyimide and reduce its height on the mesa, a plasma treatment of 300W for 20 minutes can be utilized to gently eliminate the polyimide on the surface. Finally, the n-contact metal, comprising a 70nm layer of AuGe, a 30nm layer of Ni, and a 100nm layer of Au, is deposited.

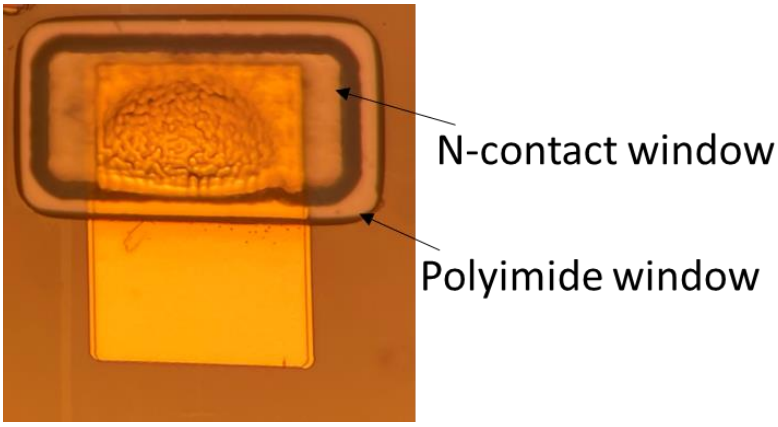

Fig. 6-8. The photo after n-contact metal process

⑦ Last, the 300nm of Au was evaporated for n-pad and p-pad. The 6 pairs of SiO_2 / Ta_2O_5 dielectric DBR were deposited. The photo after the whole process is shown in Fig. 6-9.

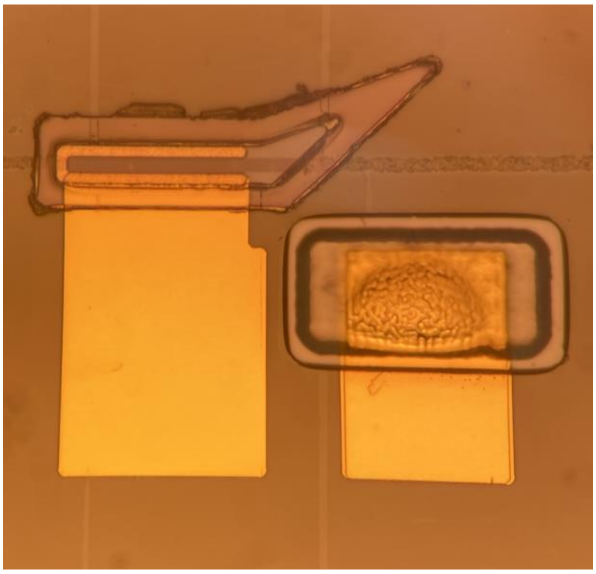

Fig. 6-9. The photo of the oxidation mesa

6.1.3 Characteristics of surface grating loaded coupled cavity VCSEL

Figure 6-10 displays the lasing spectrum of a surface grating VCSEL with a grating pitch of 650nm, an oxidation width of 4μm, and a cavity length of 200μm. The figure illustrates the achievement of single-mode slow light lasing, with the lasing wavelength centered around 1045nm. The emitted light exhibits an angle of approximately 60 degrees from the horizontal, consistent with the simulation. However, there is still evidence of vertical lasing within the 1060nm range. This occurrence can be attributed to the excessively high reflectivity of the dielectric DBR in the 1060nm range, resulting in a low threshold current. In order to realize single-mode slow light lasing, it is necessary to further decrease the reflectivity of the 1060nm range.

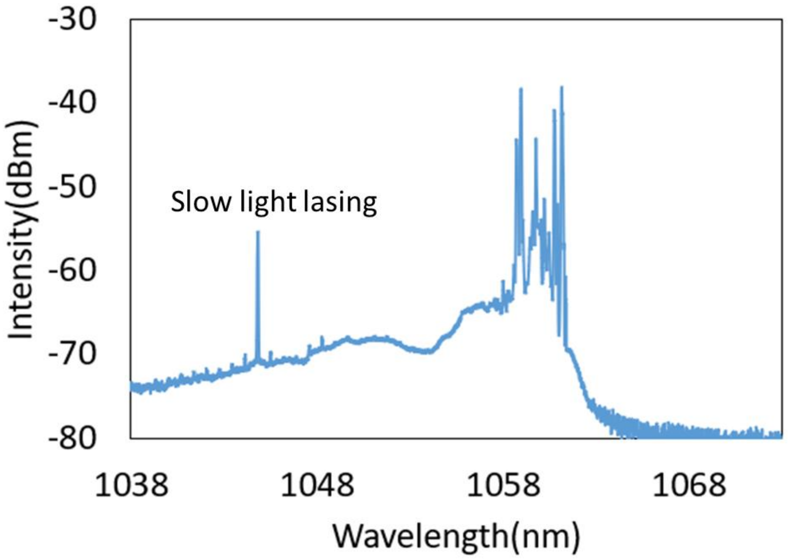

Fig. 6-10. 200μm long surface grating VCSEL.

Figure 6-11 illustrates a comparison of the lasing spectra between a surface grating VCSEL with a grating pitch of 714nm and one without a grating pitch. In both cases, the cavity length remains constant at 200μm, and the oxidation width is 4μm. When compared to the VCSEL without a surface grating, which exhibits multi-mode operation, the introduction of a surface grating enables the realization of quasi-single mode lasing at 1059nm. The implementation of the surface grating ensures transverse mode control, thereby achieving single-mode operation in VCSELs with lengths on the order of hundreds of micrometers. Additionally, this VCSEL with a 714nm grating pitch exhibits an emission angle of approximately 8 degrees, indicating fifth-order emission. This observation can be attributed to the high threshold of the slow light band induced by the dielectric DBR, whereby the 1060nm band may exhibit a lower threshold.

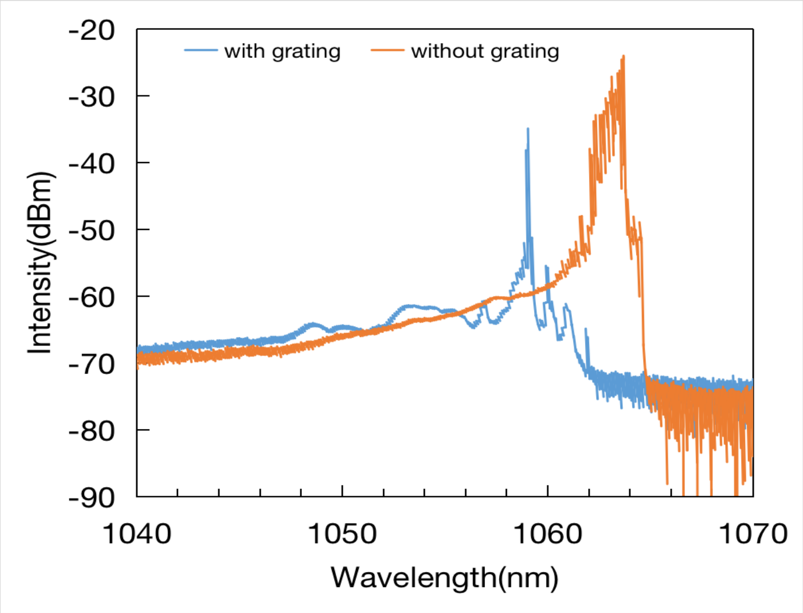

Fig. 6-11. Lasing spectra of 200μm long surface grating VCSEL.

Besides, the 2nd order grating VCSEL with 600μm of cavity length, 1.56μm of grating pitch, and 3μm of oxidation width is achieved as shown in Fig. 6-12. It fabricated on the full cavity VCSEL.

Fig. 6-12. The photo of the 2nd order grating VCSEL

Fig. 6-13 shows the LIV characteristics of 2nd order surface grating VCSEL. Larger than 160mW output power can be realized at 350mA with low voltage around 2.8V. The spectrum is shown in Fig. 6-14. Stable quasi-single mode operation from 60mA to 300mA can be obtained thanks to the surface grating.

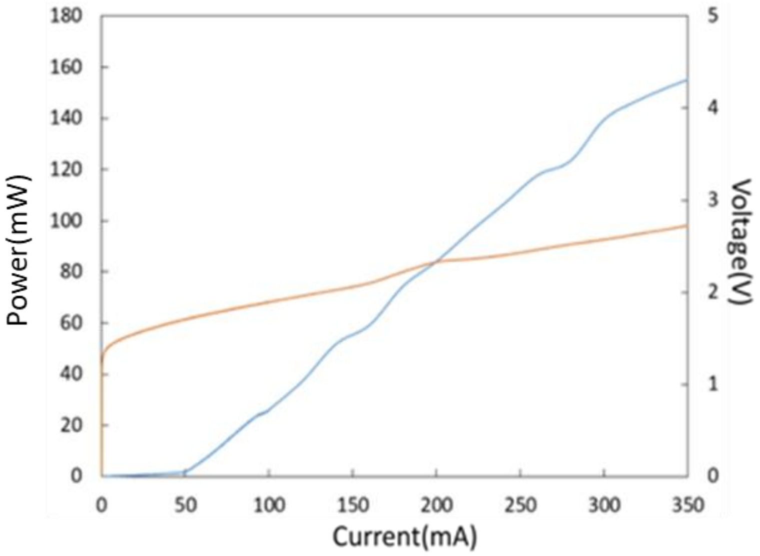

Fig. 6-13. LIV characteristics of the 2nd order grating VCSEL

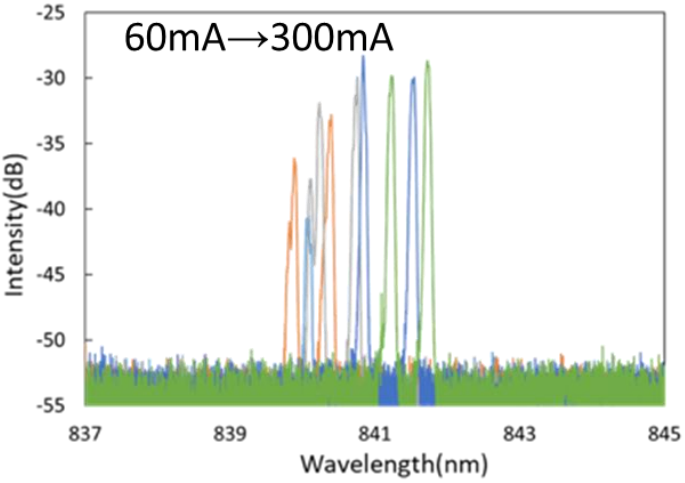

Fig. 6-14. The spectrum of the 2nd order grating VCSEL

Figure 6-15 presents the FFP and intensity distribution of each mode in a 2nd order surface grating VCSEL. The application of the 2nd order grating enables vertical emission. However, two additional modes also emerge, deviating by approximately 30 degrees from the vertical. The intensity of the vertical emission accounts for only one third of the total intensity. In order to achieve pure vertical emission, it is crucial to eliminate the T0 and T-2 modes.

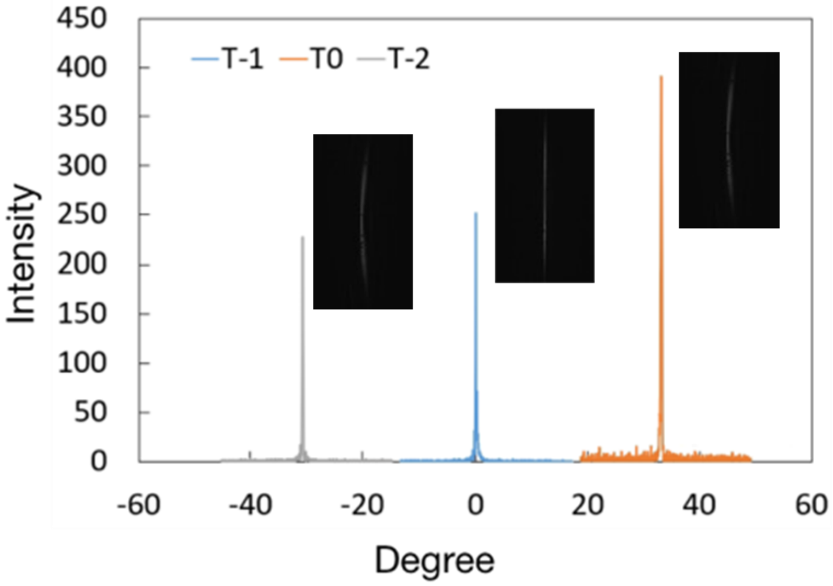

Fig. 6-15. The FFP of the 2nd order grating VCSEL

6.2 Simulation of 2nd order surface grating VCSEL for vertical emission

The study of surface emission DFB lasers and DBR lasers with second-order gratings has been ongoing since 1970 [1-5]. In the case of surface grating-loaded VCSELs, the emitted beam deviates from the vertical direction by an angle of approximately 50 degrees, which may pose challenges for fiber alignment. In this chapter, we introduce a vertical emission structure for surface grating-loaded VCSELs using a second-order grating. The angle and intensity of each deflection mode are determined using the Rigorous Coupled Wave method (GSolver).

The schematic of the second-order grating-loaded VCSEL is depicted in Figure 6-5. Here, the second-order grating is formed on the surface of a half-cavity VCSEL with six pairs of top DBR and thirty pairs of bottom DBR. As light propagates in the VCSEL in a "Zig-Zag" pattern, modifying the wavelength of the slow light mode allows for adjustment of the propagation angle, denoted as θ. This, in turn, enables control over the transmission mode and angle of the emitted light.

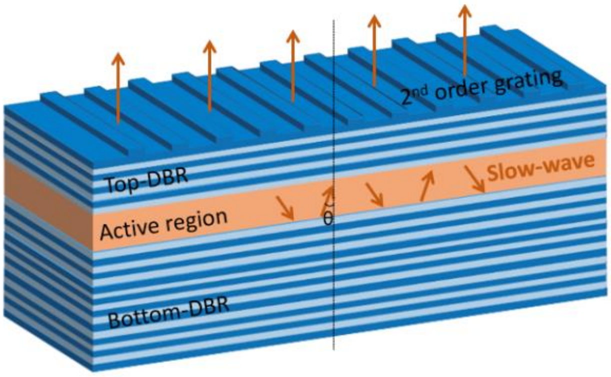

Fig. 6-5. Schematic structure of 2^{nd} order surface grating VCSEL

In the context of slow light propagation, the grating pitch of the second order, denoted as Λ, reaches a magnitude of approximately 1μm. The relationship between the grating pitch and the lasing wavelength is depicted in Figure 6-6. By maintaining a fixed grating pitch, the lasing wavelength can be effectively controlled. Subsequently, the propagation angle of the lasing wavelength can be determined, as illustrated in Figure 6-7. The cutoff wavelength, located around 1070nm, corresponds to vertical lasing. As the lasing wavelength decreases to approximately 1032nm, it experiences total reflection within the cavity.

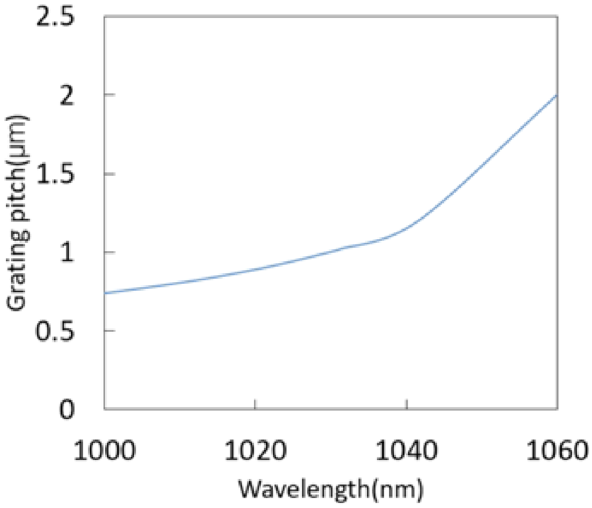

Fig. 6-6. Relation of grating pitch and lasing wavelength

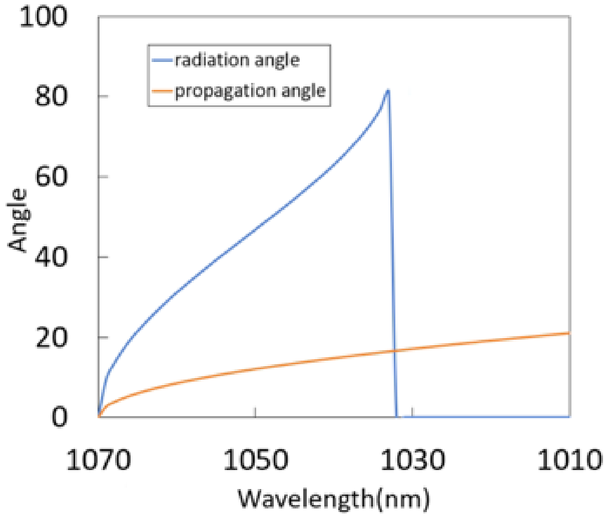

Fig. 6-7. Relation of radiation angle and propagation angle with lasing wavelength

Through the utilization of GSolver, we can effectively simulate the deflection modes within this structure. For the sake of simplicity in our simulation, we assume that the input light corresponds to the slow light mode propagating in the active region at an angle denoted as θ. This allows us to calculate the transmission and reflection modes, as depicted in Figure 6-8. Figure 6-9 illustrates the various deflection modes obtained by altering the input angle θ.

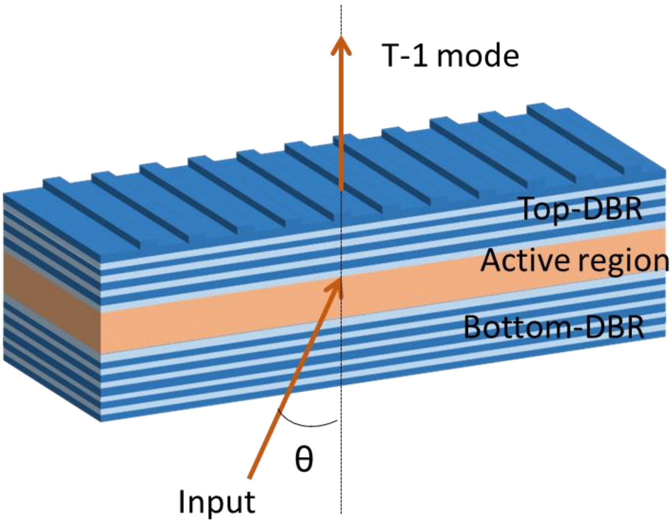

Fig. 6-8. Schematic structure of simulation model

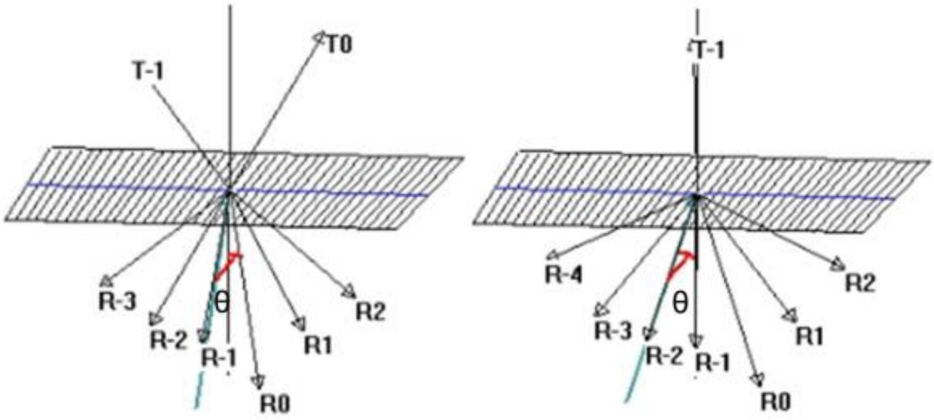

Fig. 6-9. Deflection modes at input angle (a) θ=8°, (b) θ=17°.

At an angle θ of 8 degrees, two transmittance modes, namely the T0 mode and the T-1 mode, are observed. As the angle increases to 17 degrees (θ = 17°), only the T-1 mode with vertical emission is achieved. Hence, by adjusting the angle (which corresponds to a change in the lasing wavelength), it is possible to attain single-mode operation with vertical emission. Referring to the relationship between the propagation angle and the lasing wavelength depicted in Figure 6-7, a wavelength of approximately 1030nm corresponds to a propagation angle of 17 degrees. Considering that the grating pitch remains fixed at approximately 1μm, we select a lasing wavelength of 1030nm with a 1μm grating pitch on the surface.

Figure 6-10 showcases the simulation structure, featuring a 1μm grating pitch, a grating duty cycle of 40%, a grating depth of 120nm, and a lasing wavelength of 1030nm, resulting in a propagation angle of 17 degrees. The simulation model solely encompasses the surface grating, six pairs of AlGaAs/GaAs top DBR, and the active region. The input is set at 1030nm with an angle of 17 degrees.

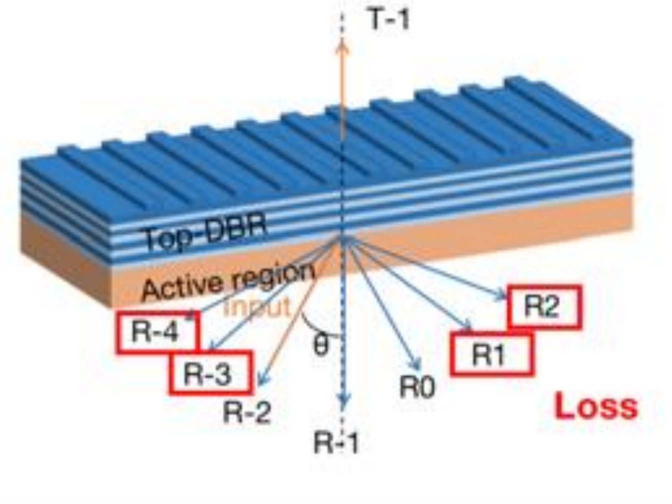

Fig. 6-10. Fabrication process flow of surface grating coupled cavity VCSEL

The simulated intensity of each deflection mode in the 1060nm half-cavity VCSEL structure with 6 pairs of [Missing information] can be observed. Figure 4 indicates a radiation dip at 1030nm, suggesting that lasing at this wavelength is feasible for the structure. Additionally, the intensity of the T-1 mode reaches approximately 50%, which is twice as high as the other higher-order reflection modes. Consequently, it is plausible to achieve vertical emission single-mode VCSELs with extended cavity lengths, enabling high-speed operations.

Fig. 6-4. Fabrication process flow of surface grating coupled cavity VCSEL

R2	R1	R0	R-1	R-2	R-3	R-4	T-1
0.5%	0.96%	95.38%	1.22%	1.7%	0.2%	0.03%	0.01%

Reference in Chapter 6

1) Iga, Kenichi. "Forty years of vertical-cavity surface-emitting laser: Invention and innovation." Japanese Journal of Applied Physics 57.8S2 (2018): 08PA01.

2) Fessant, T. "Gaussian-like tapered grating quarter wave-shifted DFB semiconductor

lasers for high-power single-mode operation." Applied Physics B: Lasers & Optics 67.6 (1998).

3) Li, Shuang, et al. "Analysis of surface-emitting second-order distributed feedback lasers with central grating phaseshift." IEEE Journal of selected topics in quantum electronics 9.5 (2003): 1153-1165.

4) Shams-Zadeh-Amiri, Ali M., Xun Li, and Wei-Ping Huan. "Above-threshold analysis of second-order circular-grating DFB lasers." IEEE journal of quantum electronics 36.3 (2000): 259-267.

5) Witjaksono, Gunawan, and Dan Botez. "Surface-emitting, single-lobe operation from second-order distributed-reflector lasers with central grating phaseshift." Applied Physics Letters 78.26 (2001): 4088-4090.

Chapter 7

Conclusion and prospective

In this chapter, the thesis will be concluded, and the prospective will be discussed.

7.1 Conclusion

In this thesis, the principle of mode control and bandwidth enhancement was demonstrated. Specifically, the achievement of single-mode operation and enhanced bandwidth is demonstrated through the utilization of intra-cavity surface relief metal-aperture VCSELs and surface grating loaded VCSELs. The thesis encompasses the simulation, fabrication process, and measurements of these devices, providing a comprehensive overview of their performance.

- The concept of mode control and bandwidth enhancement is successfully demonstrated in this study. Previous research has established that the oxidation process, as well as the implementation of metal-aperture and surface relief techniques, effectively facilitate mode control and selectivity. Through simulation, it has been observed that the metal-aperture half-cavity VCSEL allows for further expansion of the small signal modulation bandwidth due to photon-photon resonance occurring within a short distance (<2μm) between the oxidation aperture and the p-contact metal boundary. The transverse coupling strength plays a crucial role in achieving bandwidth enhancement, as it provides mode selectivity and enables stable single-mode operation. For short cavity VCSELs, the incorporation of a metal aperture proves to be an effective method for mode control. However, for longer cavity lengths, on the order of hundreds of micrometers, the implementation of surface grating loaded VCSELs is a more effective approach for achieving single-mode operation. To this end, a surface grating loaded coupled cavity VCSEL is introduced, wherein the surface grating controls the transverse modes, while the coupled cavity structure provides optical feedback, enabling the realization of the photon-photon resonance effect and thus enhancing the bandwidth.

- The fabrication process of intra-cavity surface relief metal-aperture VCSELs is successfully demonstrated. By implementing a surface relief technique with a depth of 30nm, stable single-mode operation is achieved across the entire current range, utilizing oxidation apertures of 5µm, 6µm, and even 7µm. The output power of the device with a 5µm oxidation aperture can reach 2.5mW, which can be further increased to over 3mW by reducing the reflectivity of the dielectric DBR. Additionally, the small signal bandwidth is significantly enhanced, reaching 23GHz. To further extend the small signal modulation bandwidth, an optimized configuration is considered for the intra-cavity surface relief metal-aperture VCSELs. This involves the insertion of a polyimide layer beneath the p-electrode pad, which helps reduce parasitic capacitance and increases the small signal bandwidth. Remarkably, a record-breaking small signal bandwidth of 31GHz is achieved, making it the highest bandwidth ever recorded for a 1060nm single-mode VCSEL. Moreover, the VCSELs exhibit excellent temperature robustness, enabling uncooled operation. This can be attributed to the highly strained InGaAs quantum wells employed in the design. Stable single-mode operation is maintained across the entire current range, even at elevated temperatures up to 85°C. At 55°C, the realized small signal modulation bandwidth reaches an impressive 27GHz.
- Our device exhibits promising potential for high-speed data transmission in

kilometer-long 100Gbaud applications. This is attributed to the pulse compression effect resulting from fiber negative dispersion and frequency chirp. As a result, the small signal modulation bandwidth extends to 35GHz, 32GHz, and 25GHz over transmission distances of 2km, 5km, and 10km, respectively, through SMF. Additionally, we have successfully demonstrated high-speed large signal modulations, achieving 70Gbps (NRZ) and 110Gbps (PAM4) transmissions over a 2km distance using 1300nm-SMF. Notably, we extended the link length to 10km at a 45Gbps (NRZ) rate, which is a hundredfold improvement compared to 850nm MMF links. The achieved bandwidth-distance product amounts to 450Gbps•km. Furthermore, with the assistance of digital signal processing (DSP) in offline mode, a data rate of up to 128Gbaud has been accomplished. By reducing the reflectivity of the top mirror, it is anticipated that higher-speed transmission over a 10km distance can be achieved through increased output power. Furthermore, we expect that further advancements in link lengths and bit rates can be achieved by reducing chirp and enhancing the bandwidth in transverse coupled cavity VCSELs. Additionally, we have demonstrated the feasibility of uncooled operation for large signal measurements. Thanks to its excellent temperature tolerance, the small signal modulation bandwidth reaches 27GHz, enabling 70Gbps (NRZ) and 100Gbps (PAM4) data transmissions over 2km of single-mode fiber.

- In the pursuit of achieving single-mode operation in long cavity VCSELs, we conducted modeling of surface grating-loaded VCSELs based on the coupled-mode theory, incorporating the slow-wave effect. This approach predicts a narrower stopband in surface grating-loaded VCSELs, facilitated by the slow-wave propagation resulting from significant waveguide dispersion. The use of a large surface grating pitch, owing to the low phase index, simplifies the fabrication process compared to conventional distributed feedback (DFB) structures. Our simulations indicate that a wide range of control over coupling coefficients allows for long-cavity VCSELs up to 10mm in length, as well as short-cavity devices as small as 10μm, in surface grating-loaded VCSELs. For a 10mm-long device, employing a structure with a 10nm grating depth, 19 pairs of top-DBR, and an 8th order grating enables single-mode operation with a low threshold. Through our modeling efforts, we anticipate the realization of high-power and single-mode operations in surface grating-loaded VCSELs. These devices offer distinct advantages, including the absence of facet damages, well-established VCSEL manufacturing techniques, and straightforward grating fabrication processes, making them suitable for high-power and single-mode VCSEL applications. In the case of short-cavity devices spanning around a hundred micrometers, reducing the top-DBR to 5 pairs allows for the formation of a 10μm-long grating-loaded VCSEL with a 30nm grating depth. This design facilitates single-mode operation with a low threshold. The newly introduced design flexibility in this study also enables the creation of single-mode VCSELs with larger active areas. Consequently, our proposed VCSEL platform, employing surface grating structures, offers a wide range of device lengths, from 10μm to 10mm, catering to diverse applications in VCSEL photonics.

- The fabrication process of grating-loaded VCSELs with coupled cavities is conducted. The difference is the first order surface grating formed on the wafer at the first step. Additionally, taper sides are incorporated to reduce one-sided reflectivity. The grating pitch varies at 650nm, 686nm, and 714nm. With a device length of 200μm, slow light lasing is achieved at 1045nm, exhibiting an emission angle of 60 degrees. However, the high reflectivity of the dielectric DBR in the 1060nm band results in vertical emission. By implementing a 714nm grating pitch, single-mode operation is realized at 1059nm with 5th-order emission. Furthermore, a coupled cavity VCSEL with a 600μm-long cavity demonstrates stable quasi-single mode operation. Vertical emission is achieved through the utilization of a second-order grating; however, two additional modes also emerge with approximately two-thirds of the total intensity. To achieve single-mode vertical emission, it is crucial to eliminate these two additional modes. The simulation of a second-order grating half-cavity VCSEL is illustrated, showcasing the potential of vertical emission surface grating VCSEL arrays for achieving data transmission rates of 1.6Tbps, 3.2Tbps, 6.4Tbps, and beyond..

7.2 Prospective

7.2.1 Towards intra-cavity surface relief metal-aperture VCSEL

Thanks to the implementation of the shallow surface relief and metal-aperture processes, stable single-mode operation with excellent uniformity is achieved in the 5μm oxidation diameter VCSELs, as demonstrated in Chapter 3. Importantly, the fabrication process closely resembles that of the standard conventional VCSEL process flow, allowing for successful realization of fully processed intra-cavity surface relief metal-aperture VCSELs on a 3-inch substrate. Moreover, the achieved modulation bandwidth of up to 31GHz enables high-speed data transmission, such as 70Gbps (NRZ) and 100Gbps (NRZ) over a 2km distance, highlighting the potential for applications in 100G and 400G Ethernet data center transmissions [1-3].

To address the growing demand for hyperscale data centers requiring data transmission rates exceeding 800G and beyond [4], it is imperative to consider the utilization of intra-cavity surface relief metal-aperture VCSEL 2D arrays.

7.2.2 Towards surface grating loaded VCSEL

At present, the development of surface grating VCSELs for achieving single-mode operation has been completed. However, due to factors such as the low coupling coefficient and large grating pitch, obtaining single-mode slow light lasing with cavity lengths shorter than 100μm remains a challenge. In order to address this issue and cater to high-speed applications, the development of single-mode coupled cavity surface grating VCSELs with shorter cavity lengths is of utmost importance.

To address the unintended vertical emission and low reflectivity of slow light emission, modifications need to be made to the dielectric DBR. By increasing the deposition depth of the first layer of SiO2, the reflectivity for vertical emission in the 1060nm band can be enhanced to approximately 97.9%, while the reflectivity for slow light emission in the 1040nm band can be improved to around 99.2%. By optimizing the dielectric DBR, it should be possible to achieve single-mode slow light emission.

As the current single-mode operation has only been achieved with a 200μm cavity length, primarily due to insufficient coupling coefficients, one potential approach to increasing the coupling coefficient is by increasing the surface grating depth to 40nm. With an enhanced coupling coefficient, it is anticipated that single-mode operation can be achieved in VCSELs with cavity lengths ranging from 20μm to 100μm.

In the context of coupled cavity surface grating VCSELs, further investigation is required to determine the resonant cavity length for the PPR effect. By harnessing the PPR effect, data transmission rates of up to 100Gbaud can be anticipated.

Moreover, the vertical emission capability of surface grating coupled cavity VCSELs holds great potential for the realization of 2D array surface grating VCSELs, as depicted in Figure 7-1, enabling data transmission rates in the Tbps range, aligning with the requirements of future 6G and hyperscale data center transmissions.

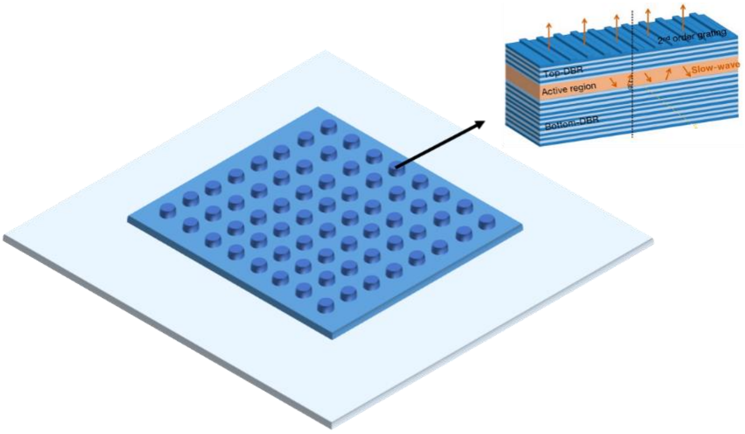

Fig. 7-1. 2D array surface grating VCSEL

Reference in Chapter 7

1) Kant, Krishna. "Data center evolution: A tutorial on state of the art, issues, and challenges." Computer Networks 53.17 (2009): 2939-2965.

2) Groumas, Panos, et al. "Multi-100 GbE and 400 GbE interfaces for intra-data center networks based on arrayed transceivers with serial 100 Gb/s operation." Journal of Lightwave Technology 33.4 (2014): 943-954.

3) Carusone, Tony Chan, et al. "F6: Optical and Electrical Transceivers for 400GbE and beyond." 2021 IEEE International Solid-State Circuits Conference (ISSCC). Vol. 64. IEEE, 2021.

4) Routray, Sudhir K., et al. "The new frontiers of 800g high speed optical communications." 2020 4th International Conference on Electronics, Communication and Aerospace Technology (ICECA). IEEE, 2020.

Publication list

(a) Journal Papers (as first author)

[J-1] Chang Ge, M. A. Hassan, Shanting Hu, Fumio Koyama, "*Modeling of surface grating-loaded VCSEL with slowing light*," *Japanese Journal of Applied Physics* 61.SK (2022): SK1010

[J-2] Chang Ge, Liang Dong, Xiaodong Gu and Fumio Koyama, "Uncooled Operations of 1060nm Single-mode Metal-aperture VCSEL for High-speed Single-mode Fiber Data Transmission", Chinese Optics Letters, 2024

[J-3] Chang Ge, Liang Dong, Xiaodong Gu, and Fumio Koyama, "*1060nm single-mode intra-cavity metal-aperture VCSEL for over 2km standard 1300nm SMF transmission*," APEX, submitted

(b) International Conferences (as presenter)

[I-1] Chang Ge, and Fumio Koyama, "*Modeling of Surface Grating-loaded VCSEL with Slowing Light,*" Micro Optics Conference 2021, PO-45, 2021

[I-2] Chang Ge, Boxuan Zhang, Xiaodong Gu, Susumu Kinoshita, and Fumio Koyama, "*Full 3-inch wafer processed 1060nm single-mode transverse coupled-cavity VCSEL for data transmission in standard 1300nm single-mode fiber,*" Optical Fiber Communication Conference (OFC) 2023, Th2A.9, 2023

[I-3] Chang Ge, Liang Dong, Xiaodong Gu, and Fumio Koyama, "*1060nm single-mode intra-cavity metal-aperture VCSEL for over 2km standard 1300nm SMF transmission,*" Conference on Lasers and Electro Optics (CLEO) 2023, STh4Q.2 2023

[I-4] Chang Ge, Liang Dong, Xiaodong Gu, and Fumio Koyama, "*Uncooled operations of 100Gbps 1060nm Single-mode Metal-aperture VCSEL for Standard SMF transmission,*" European Conference on Optical Communication (ECOC) 2023

(c) Domestic Conferences

[D-1] Chang Ge, and Fumio Koyama, "*Modeling of surface grating-loaded VCSEL with slowing light,*" The 82th JSAP Autumn Meeting, 10a-N405-5, 2021.

[D-2] Chang Ge, Xiaodong Gu, and Fumio Koyama, "*Modeling of surface grating-loaded VCSEL for vertical emission*," The 83th JSAP Autumn Meeting, 2022, 22a-C101-11, 2022.

[D-3] Chang Ge, Xiaodong Gu, and Fumio Koyama, “*1060nm single-mode intra-cavity metal-aperture VCSEL for over 2km standard 1300nm SMF transmission*,” The 70th JSAP Spring Meeting, 2023, 17p-A303-4, 2023.

謝辞 Acknowledgement

Firstly, I would like to express my sincere gratitude to Prof. Fumio Koyama for providing me with the invaluable opportunity to pursue my studies in Japan and for his kind supervision throughout my three-year research journey. His dedication, guidance, and suggestions regarding my research topic have greatly enriched my knowledge and experiences. I am truly grateful for his invaluable support in this study.

I would also like to extend my gratitude to the other professors in our laboratory: Prof. Iga Kenichi, Prof. Hiroyuki Uenohara, Prof. Tomoyuki Miyamoto, Prof. Nobuhiko Nishiyama at Tokyo Institute of Technology, and Prof. Toshihiko Baba at National Yokohama University. Their advice and insights shared during various meetings and conferences have been instrumental to the progress of my research.

I also hope to thank Prof. Susumu Kinoshita, Dr. Takahiro Sakaguchi, and Mr. Hisao Sudo for their invaluable assistance with my experiments and clean room management.

I am grateful to Prof. Xiaodong Gu for his academic advice and support in my daily life.

I would also like to express my gratitude to the secretaries of the Koyama Lab: Ms. Hiromi Yoshida, Ms. Satsuki Ogawa, Ms. Tomie Chiba, and Ms. Etsuko Koiwa for their assistance and support during my time in the lab.

I extend my appreciation to Dr. Shanting Hu, Dr. Hameeda Ibrahim, Dr. Ahmeda Hassan, Dr. Ruixiao Li, Mr. Liang Dong, Mr. Boxuan Zhang, Ms. Di Wu, and Ms. Ling Yan for their invaluable help with my simulations, experiments, study advice and support in various aspects of my life.

Finally, I want to express my heartfelt appreciation to my parents for their unwavering support in every aspect of my life.